Title
Cosmic Cartography: Mapping the Universe for Next-Generation Dark Energy Voyages

Author
Kitanidis, Elpida Ellie

Publication Date
2020

Peer reviewed|Thesis/dissertation

Cosmic Cartography: Mapping the Universe for Next-Generation Dark Energy Voyages

by

Elpida Ellie Kitanidis

A dissertation submitted in partial satisfaction of the

requirements for the degree of

Doctor of Philosophy

in

Physics

in the

Graduate Division

of the

University of California, Berkeley

Committee in charge:

Professor Martin White, Chair
Professor Adrian Lee
Professor Daniel Kasen

Spring 2020

Cosmic Cartography: Mapping the Universe for Next-Generation Dark Energy Voyages

Abstract

Cosmic Cartography: Mapping the Universe for Next-Generation Dark Energy Voyages

by

Elpida Ellie Kitanidis

Doctor of Philosophy in Physics

University of California, Berkeley

Professor Martin White, Chair

Mapping the distribution of matter and light in the Universe is key to unlocking some of its most fundamental secrets. What drives the acceleration of cosmic expansion? Does Einstein's Theory of General Relativity fail on very large scales, requiring a new model of gravity to account for an accelerating expansion? Or is there some exotic and invisible form of "dark energy" that dominates the composition of our Universe? Beginning with the Dark Energy Spectroscopic Instrument (DESI), a series of next-generation galaxy surveys will revolutionize our understanding of dark energy, providing an unprecedented wealth of data to solve these and other cosmic mysteries. Several major challenges directly determine the ultimate success of ambitious missions such as DESI: how tightly systematic sources of error and contamination can be controlled, how well the biases and properties of the galaxy samples can be understood, and how accurately their positions can be mapped. This thesis presents contributions I have made towards addressing these challenges and doing early science with DESI, for which I received "Builder Status" by the DESI Collaboration. Approximately two-thirds of this thesis are devoted to performing the first major analysis of the systematics and clustering of DESI samples selected from deep imaging. In the final part of this thesis, I present a cross-correlation between DESI galaxies and the lensing of the cosmic microwave background, one of the most significant detections of this type of signal to date, from which I further characterize the DESI samples and also study how the accuracy of their positions impacts science goals. In addition to enabling future cosmology with DESI, the methodologies and frameworks developed in this thesis have broader applications in future dark energy experiments and, more generally, cosmological studies using deep imaging data.

For my parents, Ranna and Peter
And for Nate

Contents

List of Figures

List of Tables

Acknowledgments

I am deeply grateful to my advisor, Professor Martin White, for his guidance, generosity, and support, as well as the other members of my doctoral committee, Professor Adrian Lee and Professor Daniel Kasen, for their thoughtful feedback on this dissertation. I feel incredibly lucky to have been surrounded by such distinguished scholars during my time at UC Berkeley. To the fantastic community of staff scientists and postdoctoral researchers here and at the Lawrence Berkeley National Lab, as well as my esteemed DESI collaborators, it has been a pleasure working with you all and I have learned a great deal from our discussions. I would like to especially thank Dr. David Schlegel, who served on my qualifying exam committee and has been another wonderful mentor to me, and Dr. Yu Feng, whose high-performance computing expertise saved the day too many times to count.

To my fellow physics and astronomy students at Berkeley, my awesome housemates, my study buddies, my "cosmograds" cohort, the ladies of the Society of Women in the Physical Sciences, and the past and present organizers of the Career Development Initiative in the Physical Sciences, thank you for sharing the ups and downs of graduate life with me.

Last but not least, I am profoundly thankful for the love, encouragement, and support of my family and friends throughout this marathon of grad school. Nate, Mom, and Dad - I wouldn't have made it to the finish line without you cheering me on. Dean, Phoebe, Janet, Phil, Emily, Lincoln - thank you for making every milestone special by celebrating with me.

Chapter 1

Introduction

1.1 Overview

Over the last few decades, supported by a growing body of publicly available data, scientific consensus has converged upon a new phenomenological model of the Universe: the ΛCDM model. ΛCDM is often referred to as a "concordance model" because of its ability to explain a multitude of seemingly disparate or conflicting observations, from the clustering of galaxies, to the anisotropies in the cosmic microwave background, to the discovery that our Universe is currently undergoing a period of accelerated expansion. ΛCDM can interpret all these phenomena and more from within a single self-consistent framework. Even more remarkably, it has made additional predictions that were later verified: the statistics of weak gravitational lensing, the existence of baryonic acoustic oscillations, and the polarization of the cosmic microwave background are a few of its notable recent successes.

While the ΛCDM model is appealingly predictive and well supported by experimental evidence, it is also incomplete and slightly mystical. The key ingredients of ΛCDM are dark energy, an exotic component of the Universe that acts as a sort of "anti gravity," and cold dark matter, an invisible particle that does not interact with light. Though we can detect them only indirectly, dark energy and dark matter together make up over 95% of the energy content of the Universe. Dark energy alone accounts for nearly 70% of this, yet it has not been measured with adequate precision to narrow the field of possible theories or even definitively confirm its existence. Fortunately, we are entering a new era of precision cosmology. As galaxy surveys, as well as experiments mapping the cosmic microwave background, become wider and deeper, span more frequencies, and enable more accurate measurements than ever before, the answers to these fundamental questions may finally be within reach.

However, this new era of precision cosmology presents many new challenges. First, ultra-precise measurements demand meticulous control over any and all sources of systematic uncertainty, which are increasingly dominating the stingy error "budgets" of modern cosmology experiments. Secondly, precise cosmological constraints require a mature understanding of how the phenomena we are able to observe connect to the phenomena we wish to un-

derstand; these relationships are profoundly complex and subtle, necessitating sophisticated physical models and detailed characterizations of the data samples. Thirdly, with the rising volume and multiplicity of astronomical data, and the corresponding surge in computationally expensive, labor intensive, and time-consuming work, new tools must be innovated. For example, it is no longer feasible to obtain spectroscopic redshifts for every galaxy detected, and as photometric redshifts alone do not meet the required accuracy, we must seek out new techniques such as inferring redshifts through cross-clustering measurements.

This thesis presents contributions I have made towards addressing each of the aforementioned challenges, mainly within the context of the Dark Energy Spectroscopic Instrument (DESI) experiment, which is advancing the boundary of human understanding by creating the largest 3D map of the Universe to date and providing unrivaled constraints on dark energy. While these contributions are crucial stepping stones towards doing cosmology with DESI, the methodologies and findings presented herein are also broadly applicable to next-generation dark energy experiments and thus have significant implications beyond DESI.

1.2 Layout

Chapter 2 contextualizes this body of work, giving an overview of the state of the field, from its foundations in Einstein's Theory of General Relativity to the bleeding edge of modern experiments. Throughout, we motivate the unique challenges facing cosmology in the next decade, and explain how this thesis aims to address various aspects of those challenges.

Chapters 3 and 4 are papers (one accepted for publication, one to be submitted after the conclusion of internal collaboration review) of which I was the first author. In each of these multi-author works, I performed all of the analysis and writing. Co-authors contributed advice and helpful discussions, or were instrumental to the creation of data reduction pipelines upstream of mine. For the sake of organizational clarity, I have made no significant alterations to the content of these papers, choosing instead to include them in their original versions with minor aesthetic changes and transitions. The introductory chapter serves to unite these papers within a shared scientific context and give an integrated perspective.

Chapter 2

Scientific Background & Motivations

2.1 Review of Relevant Cosmology

In this section, we give a brief review of the basic ideas of cosmology needed to motivate and understand dark energy, which is the focus of the DESI experiment and this thesis. The following is by no means intended to be a comprehensive treatment of these topics.

The Cosmological Principle and Hubble's Discovery

Modern physical cosmology is built around a fundamental observation about the Universe: on sufficiently large scales, it is homogeneous and isotropic. Phrased another way, this so-called "Cosmological Principle" states that laws of physics are the same everywhere and that our corner of the Universe is a statistically representative sample of the whole. We emphasize that the Cosmological Principle applies on scales much larger than the typical size of a galaxy cluster (a few Mpc); zoomed in on any particular region of space, there is plenty of texture, structure, and asymmetry to be seen. However, averaged over scales > 100 Mpc, the cosmos appears smooth and uniform, with no special locations or preferred directions.

Another very important observation about the Universe was made by Edwin Hubble[1] (Hubble 1929) nearly a century ago: it is expanding. By estimating the distances and velocities of stars in galaxies outside the Milky Way, Hubble determined that far away galaxies are receding from one another, and moreover that the rate of recession is proportional to their separation, with a slope given by the Hubble constant H_0. Though not immediately interpreted so by Hubble himself, this observation became a cornerstone for the subsequent tower of experimental evidence that the Universe is expanding, a result that had already been predicted from theory independently by Friedmann (1922) and Lemaître (1927).

Hubble estimated the velocities of objects from their redshifts. When the source of an electromagnetic wave is moving away from the observer, its wavelength is increased, making it appear "redder." Meanwhile, elements such as hydrogen and helium absorb and emit pho-

[1] Though there is some controversy regarding the credit of this discovery! See e.g. Block 2012.

tons at specific wavelengths, leading to characteristic patterns in the spectra of light from astronomical objects. By seeing how these patterns have redshifted, astronomers can calculate the velocities of objects relative to us - and, through Hubble's law, their distances. By far the most dominant contribution to this velocity is from the expansion of the Universe (see Section 2.4 for a discussion of peculiar velocities in the context of redshift-space distortions), and thus we can directly relate the redshift z to the scale factor a,

$$1 + z = \frac{a_0}{a} \tag{2.1}$$

where $a(t)$ quantifies the size of the expanding Universe at time t relative to today, $a_0 \equiv a(t_{\text{today}}) = 1$, and is defined to be zero at the beginning of time.

General Relativity and Einstein's Biggest Blunder

A few years prior to Hubble's discovery, Einstein completed his Theory of General Relativity, leading to some of the most revolutionary paradigm shifts in the history of science. In the classical Newtonian view, gravity is a force that acts upon massive bodies and accelerates them. In the relativistic Einsteinian view, gravity is an inherent feature of four-dimensional spacetime, which is curved by the presence of massive bodies. The key principles of General Relativity are often summarized as "mass tells spacetime how to curve, spacetime tells mass how to move." These ideas are encoded in Einstein's Field Equations (EFE), 10 equations that can be elegantly represented in a single line using Einstein tensor notation:

$$R_{\mu\nu} - \frac{1}{2}Rg_{\mu\nu} + \Lambda g_{\mu\nu} = \frac{8\pi G}{c^4}T_{\mu\nu} \tag{2.2}$$

Without delving into details, the left side of the equations may be thought of as representing curvature while the right side represents matter. These equations can be solved for the metric tensor $g_{\mu\nu}$, which describes the geometry of the Universe. Arguably the most important exact solution to EFE is the Friedmann-Lemaître-Robertson-Walker (FLRW) metric, which describes a homogeneous, isotropic, and expanding spacetime. From the FLRW metric and EFE, we obtain the Friedmann equations governing cosmic dynamics at large scales:

$$\left(\frac{\dot{a}}{a}\right)^2 = \frac{8\pi G}{3}\rho + \frac{\Lambda c^2}{3} - \frac{kc^2}{a^2} \tag{2.3}$$

$$\frac{\ddot{a}}{a} = -\frac{4\pi G}{3}\left(\rho + \frac{3p}{c^2}\right) + \frac{\Lambda c^2}{3} \tag{2.4}$$

The term $\dot{a}/a$ in Equation 2.3 is called the Hubble parameter, $H(z)$. Its present-day value is the Hubble constant, H_0. k is curvature ($k = +1$ for a positively curved Universe, $k = 0$ for a flat Universe, and $k = -1$ for a negatively curved Universe), G is Newton's gravitational constant, c is the speed of light, and ρ and p are, respectively, the density and isotropic pressure of the contents of the Universe. But what of Λ? What does this term represent?

Einstein originally added the Λ term, called the "cosmological constant," to his equations in order to counterbalance the effects of gravitational attraction and allow for a static Universe. When the expansion of the Universe was confirmed, he abandoned this term, calling it his "biggest blunder." However, the cosmological constant was re-introduced after the 1998 discovery that the Universe's expansion is accelerating (Perlmutter et al. 1998, Riess et al. 1998). In order to mathematically account for this acceleration, a new term must be added to the Friedmann equations. It represents an exotic and pervasive type of energy, dubbed "dark energy," that accounts for nearly 70% of the energy content of the Universe and has strange properties such as exerting negative pressure and not diluting in density as the volume of the Universe grows. The cosmological constant has thus been revived as the primary dark energy candidate, due to its simple origins in EFE as well as its interpretability as a "vacuum energy" of the sort that arises naturally in quantum field theories[2].

The Composition and Dynamics of the Universe

The evolution of the Universe is complicated by the fact that it contains many different types of energy, each of which evolves differently. In addition to the radiation and ordinary baryonic matter we encounter in our daily lives, decades of observational evidence indicate the existence of yet another type of matter, one that interacts gravitationally but not electromagnetically. This invisible matter, called "dark matter" (not to be confused with the distinct concept of dark energy) is thought to make up 85% of the matter in the Universe. Revisiting the first Friedmann equation, the density can now be written out in terms of the different components of the Universe: $\rho = \rho_{\rm m} + \rho_{\rm r} = (\rho_{\rm b} + \rho_{\rm DM}) + \rho_{\rm r}$. To include the cosmological constant as a dark energy term, the substitution is usually made

$$\rho \to \rho - \frac{\Lambda c^2}{8\pi G} \tag{2.5}$$

which is conceptually equivalent to defining a new type of density $\rho_\Lambda = \frac{\Lambda c^2}{8\pi G}$. Next, switching to the second Friedmann equation, we make the substitution

$$p \to p + \frac{\Lambda c^4}{8\pi G} \tag{2.6}$$

which is equivalent to the substitution we made for the density but with the added assumption that dark energy is a perfect fluid ($p = w\rho c^2$) with negative pressure given by $w_\Lambda = -1$.

The Friedmann equations can be solved for a perfect fluid, giving density evolution

$$\rho(z) \propto \exp\left(3\int_0^z \frac{1 + w(z')}{1 + z'} dz'\right) \tag{2.7}$$

[2]As of yet, however, the two theories have not been made consistent with one another; the discrepancy between predicted values for Λ is so astonishingly large that it has been named "the vacuum catastrophe."

For matter ($w = 0$), $\rho_m \propto a^{-3}$. For radiation and other relativistic matter such as neutrinos ($w = 1/3$), $\rho_r \propto a^{-4}$. For a cosmological constant ($w = -1$), $\rho_\Lambda \propto a^0$.

We can rewrite everything in terms of the dimensionless density parameter Ω, which is the ratio of the actual density to the critical density of the Universe. The critical density is the density corresponding to a flat Universe, $\rho_{\rm crit} = \frac{3H^2}{8\pi G}$. Furthermore, we can write the density parameter Ω at any time in terms of its value today Ω_0 times its evolution. Putting this all together and simplifying, we obtain a definition for the dimensionless Hubble parameter,

$$E(z) \equiv \frac{H(z)}{H_0} = \sqrt{\Omega_{\rm m,0}(1+z)^3 + \Omega_{\rm r,0}(1+z)^4 + \Omega_{\Lambda,0} + \Omega_{k,0}(1+z)^2} \tag{2.8}$$

where we have also absorbed the curvature term, $\Omega_{k,0} = -\frac{kc^2}{H_0^2} = 1 - \Omega_{\rm m,0} - \Omega_{\rm r,0} - \Omega_{\Lambda,0}$.

The cosmological constant is a key ingredient of the ΛCDM standard model of cosmology, which has been one of the most successful predictive theories of all time. However, it is important to emphasize that the cosmological constant is not the only dark energy candidate. To obtain an accelerating Universe from the Friedmann equations, it is only necessary that $w_{\rm DE} < -1/3$, not that $w_{\rm DE} \equiv w_\Lambda = -1$. Furthermore, though the density of dark energy has been measured at different redshifts and appears constant within errors, there has been insufficient precision thus far to definitively rule out dynamic dark energy, $w_{\rm DE} \to w_{\rm DE}(z)$. Several parametric models of dynamic dark energy have been proposed, the most common being the Chevallier-Polarski-Linder (CPL) model (Chevallier & Polarski 2001, Linder 2003). Furthermore, dark energy itself is not the only possible solution to cosmic acceleration; if, instead, General Relativity were modified in some way, an accelerating Universe might be explainable without dark energy at all. Next-generation dark energy experiments such as DESI (described in the next section) will be critical to distinguishing between these different theories and answering the most fundamental questions about the nature of the cosmos.

2.2 The Dark Energy Spectroscopic Instrument

Introduction

The Dark Energy Spectroscopic Instrument (DESI) is a state-of-the-art dark energy experiment that is designed to create the largest three-dimensional map of the Universe to date. DESI is a wide-area survey covering a $\sim$ 14,000 square degree footprint. The titular spectroscopic instrument boasts a unique robotic fiber positioning system that will allow it to measure over 5,000 spectra simultaneously. Thus DESI inherits the legacy of the highly successful and groundbreaking Baryon Oscillation Spectroscopic Survey (BOSS; Dawson et al. 2013b), and extends it in both redshift and sky area, leading to a remarkable order of magnitude improvement in the number of galaxies observed and the volume of the Universe mapped. DESI is a trailblazer, representing the first "Stage IV" dark energy experiment on the sky, as defined by the Dark Energy Task Force (a committee convened to advise the Department of Energy, the National Aeronautics and Space Administration, and the National

Science Foundation on the future of dark energy research) in their detailed community planning report (Albrecht et al. 2006). Installed on the Mayall telescope at Kitt Peak, DESI is currently in its survey validation phase, during which time the various data collection, processing, and analysis pipelines are tested over small regions of the sky. Following survey validation, DESI is expected to begin its five-year mission sometime in 2020.

DESI's main science goals are to chart the expansion history of the Universe through baryon acoustic oscillations (BAO; see Section 2.3) and constrain the growth of large-scale structure through redshift-space distortions (RSD; see Section 2.4) with unprecedented precision. As we will discuss, both BAO and RSD are powerful probes of dark energy, and together they will provide some of the best constraints to date. In addition to dark energy, DESI will enable other cosmological studies, for example of the sum of neutrino masses and theories of inflation; as these are not the focus of this thesis, we will not provide details here.

Main targets

DESI will measure spectra for approximately 6 million luminous red galaxies (LRG) up to z = 1.0, 17 million [OII] emission-line galaxies (ELG) up to z = 1.6, and 2.5 million quasars (QSO) up to z = 3.5. These three main target classes, briefly described below, are selected from deep optical photometry provided by the Legacy Surveys (Dey et al. 2018), complemented by near-infrared imaging from the Wide-field Infrared Survey Explorer (WISE; Wright et al. 2010). Each target type requires its own unique set of techniques for selecting a sample from photometry that will optimize spectroscopic completeness and efficiency when it is time to acquire spectra. In addition, bad imaging or target selection may even lead to types of contamination that cannot be deprojected with spectroscopy.

LRGs are massive, bright, early-type galaxies that are inherently red due to their old stellar populations. Their strong clustering make them excellent probes of large-scale structure at low redshift. A homogeneous sample of LRGs can be selected from photometry by exploiting the 1.6μm (rest frame) peak in their spectral energy distributions and similarly the 4000Å break continuum feature makes it easy to reliably measure their redshifts across the desired redshift range $0.4 < z < 1.0$.

ELGs are late-type galaxies that are inherently blue due to their high rates of active star formation, exhibiting strong emission lines from the ionized gas around their massive, luminous stars, most notably the [OII] doublet. This distinctive feature enables highly accurate redshift measurements. The majority of the galaxies targeted for spectroscopy by DESI will be ELGs, spanning the wide redshift range $0.6 < z < 1.6$.

QSOs are exceptionally bright due to the energy released as gas falls in towards the supermassive black holes at their centers. Though relatively rare, their extreme luminosity ensures that QSOs can be measured to very high redshift, making them invaluable tools for studying the Universe. QSOs in the redshift range $0.9 < z < 2.1$ will be used for their clustering as direct tracers of dark matter, similar to LRGs and ELGs. Furthermore, QSOs can be used to probe even higher redshifts due their Lyman-α features. The Lyman-α forest is a series of absorption lines in the spectra of distant quasars as the light travels through neutral hydrogen

in the inter-galactic medium (IGM) prior to the formation of galaxy clusters. Thus, with high enough density, these features can be interpolated to create maps of the distribution of hydrogen at $z > 2.1$.

Synergies with CMB

In combination with other experiments, DESI will also enable powerful statistical constraints that would be impossible otherwise. For example, DESI overlaps with the Dark Energy Survey (DES) and the Large Synoptic Spectroscopic Telescope (LSST; LSST Science Collaboration et al. 2009), two deep photometric surveys that probe dark energy in complementary ways to DESI. In particular, we would like to draw attention to synergies with cosmic microwave background experiments (CMB). For example, cross-correlations between DESI galaxies and the lensing of matter by the CMB, as measured by modern high-resolution experiments such as Planck, will greatly improve the signal-to-noise ratio of the lensing signal (and thus constraints on cosmological parameters such as the density of matter). Furthermore, by breaking degeneracies between galaxy bias and dark matter clustering, such studies allow us to cleanly extract information about the tracer samples. We perform this measurement and analysis using an LRG sample selected from imaging in Chapter 4.

2.3 Baryon Acoustic Oscillations

In this section, we provide background on the topic of baryon acoustic oscillations (BAO), the primary deliverable of many next-generation dark energy experiments including DESI. In the first sub-section, we motivate the idea of using "statistical standard rulers" to probe dark energy, after which we briefly review the physics of BAO and why it makes for an ideal statistical standard ruler. In the final sub-section, we summarize the status of BAO measurements, tease the new ultra-precise constraints that DESI is capable of achieving, and highlight the role of this thesis towards helping the collaboration reach its goals.

Standard clocks, candles, and rulers

Dark energy is studied through its effect on the expansion history of the Universe. Recall that the dimensionless Hubble parameter can be written,

$$E(z) = \frac{H(z)}{H_0} = \sqrt{\Omega_{\mathrm{m},0}(1+z)^3 + \Omega_{\mathrm{r},0}(1+z)^4 + \Omega_{\mathrm{DE},0} f(z) + \Omega_{k,0}(1+z)^2} \tag{2.9}$$

where we have replaced the cosmological constant model $w_\Lambda = -1$ with a more general dark energy model having equation of state $w_{\mathrm{DE}}(z)$ and corresponding density evolution $f(z)$. Thus, one way to constrain dark energy is to directly measure the Hubble parameter - for example, through the "differential age" method, also known as "cosmic chronometers" (Jimenez & Loeb, 2002), where passively evolving galaxies are age-dated based on their

stellar populations and the redshift-time relation $\frac{\Delta z}{\Delta t} \approx \frac{dz}{dt}$ gives a direct estimate of $H(z)$. This is a "standard clock" method, taking advantage of features of known duration or age. However, such measurements are presently still highly dominated by the systematics involved in determining galaxy ages (see e.g. discussion in Moresco et al. 2016).

Another way to probe the expansion history of the Universe is to use distance measurements from "standard rulers" or "standard candles," meaning features of known size or luminosity, respectively. We recall that the line-of-sight co-moving distance is given by

$$d_C(z) = c \int_0^z \frac{dz'}{H(z')} \tag{2.10}$$

while the transverse comoving distance is given by

$$d_M(z) = \begin{cases} \frac{c}{H_0} \frac{1}{\sqrt{\Omega_k}} \sinh(\sqrt{\Omega_k} d_C(z) H_0/c) & \Omega_k > 0 \\ d_C(z) & \Omega_k = 0 \\ \frac{c}{H_0} \frac{1}{\sqrt{|\Omega_k|}} \sin(\sqrt{|\Omega_k|} d_C(z) H_0/c) & \Omega_k < 0 \end{cases} \tag{2.11}$$

We now define the angular diameter distance,

$$d_A(z) \equiv \frac{x(t_e)}{\theta} = \frac{x(t_o)}{\theta(1+z)} \tag{2.12}$$

where x is the physical size and θ is the observed angular size, and we also define the luminosity distance,

$$d_L \equiv \sqrt{\frac{L}{4\pi S}} \tag{2.13}$$

where L is the intrinsic luminosity and S is the observed (bolometric) flux. These distance measurements are related to d_M by

$$d_A(z) = \frac{1}{1+z} d_M(z) \tag{2.14}$$

$$d_L(z) = (1+z) d_M(z) \tag{2.15}$$

Thus, if we measure $d_A(z)$ by observing the angle that an object of known transverse size extends in the sky, or $d_L(z)$ by observing the flux of an object with known intrinsic luminosity, we obtain a measurement of $d_M(z)$. This gives a constraint on $d_C(z)$ that is inherently degenerate with curvature Ω_k. Furthermore, since $d_C(z)$ is an integral over $H(z)^{-1}$ which is itself an integral over $w(z)$, any rapidly oscillating features in the parameter of interest will be washed out. However, while standard candles can only measure $d_M(z)$, standard rulers fortunately can also estimate $H(z)$, assuming the characteristic physical scale is present along

the line-of-size dimension as well as the transverse dimension. The line-of-sight co-moving distance between two nearby events (that are close in redshift) is given by

$$d_C(z+dz) - d_C(z) = \int_z^{z+dz} \frac{c\ dz'}{H(z')} \approx \frac{c\ dz}{H(z)} \tag{2.16}$$

Using standard rulers, we can simultaneously measure $H(z)$ and $d_A(z)$, capturing both the instantaneous and integrated expansion history of the Universe, which allows us to distinguish between different cosmological models and achieve much tighter constraints on dark energy.

Historically, possible standard rulers have included certain types of radio sources (e.g. Kellermann 1993, Buchalter et al. 1998), as well as galaxy clusters (e.g. Allen et al. 2002). However, a class of astrophysical objects usually can't be observed at many different redshifts or with high enough densities to overcome shot noise. Furthermore, such objects are generally neither uniform enough nor well enough constrained in their properties to give precise results. Thus, cosmologists' attentions turned to "statistical standard rulers," meaning rulers based on statistical properties of the Universe, such as the Hubble scale at matter-radiation equality. However, by far the most powerful and successful statistical standard ruler thus far has been the BAO scale, for the following reasons: it is based on well-understood physics (described in the next section), it can be calibrated over most of the age of the Universe, and it has a value that is squarely in the linear regime, thus permitting perturbative treatment.

The physics of BAO

The formation of structure relies on the notion of gravitational instability - that is, the notion that overdense regions will become more overdense with time as their self-gravity overcomes the opposing influence of cosmic expansion, while the inverse is true for underdense regions. However, during the early history of our Universe, density perturbations behaved instead as acoustic waves, giving rise to features seen in the anisotropies of the cosmic microwave background as well as patterns in the clustering of matter. Thus, in order to explain the physics of BAO, we must give a brief history of the first million years of the Universe.

Fractions of a moment after the birth of the Universe, small perturbations in its smooth background, generated by quantum fluctuations, were expanded to cosmic scales through a period of rapid exponential growth known as inflation. Inflation imprinted these initial perturbations in all species and on all scales simultaneously. Since the expansion of the Universe was faster than the speed of light during the inflationary epoch, some perturbations were planted on super-horizon (i.e. not causally connected) scales. The establishment of these gravitational potential wells seeded the large-scale structures seen today.

Three minutes after the Big Bang, the young Universe was comprised of a hot, dense particle soup of photons, electrons, protons, and neutrons. Due to the high temperature and photon-to-baryon density ratio, neutral hydrogen and helium could not form without getting broken apart immediately by photons, so the plasma was ionized. This primordial world was also opaque, as photons experienced extremely short mean free paths before Compton

scattering off the free electrons[3], which in turn interacted with the protons via the Coulomb force. Through these interactions, the system remained in thermal equilibrium, behaving as a tightly coupled photon-baryon fluid. The fluid oscillated due to the competing forces of the background gravitational potential (due initially to the relativistic species i.e. photons and neutrinos, and later to dark matter after matter-radiation equality at $z \sim 3570$) acting on the electrons and nucleons to compress the fluid, and radiation pressure from the photons resisting the compression. The resulting acoustic waves propagated outwards from every initial perturbation with a relativistic sound speed $c_s \approx c/\sqrt{3}$. Dark matter, in the meantime, was not affected by radiation pressure and did not oscillate; instead, it grew in place over the initial perturbations, although its growth was retarded prior to matter-domination.

Over the next $\sim$ 380,000 years, the Universe expanded and cooled to $\sim$ 4,000 K. At this temperature, even the high tail-end of the blackbody spectrum did not possess enough photons with the ionizing energy (13.6 eV) required to prevent electrons and nucleons from combining, and thus neutral hydrogen began to form. This phase-transition event, referred to (rather confusingly) as "recombination," took place over $\sim 70,000$ years, with the midpoint typically defined as occurring at $z \sim 1370$ when the number density of neutral atoms became equal to the number density of ions. As the ionization fraction decreased and photons gained the freedom to travel farther and farther without scattering off electrons, they began to decouple from the baryon gas, and the photon-baryon wave slowed. The epoch of photon decoupling is usually defined as occurring when the interaction rate of photons became equal to the rate of the expansion of the Universe, though decoupling was not an instantaneous process; the gradual diffusion of the photons can be seen in the Silk damping of the acoustic oscillations. When the last photons decoupled from the plasma (known as the "surface of last scattering," $z \sim 1100$), the pressure waves stalled, leaving spherical shells of baryons at the sound horizon radius 150 h^{-1}Mpc. The photons that streamed away are the cosmic microwave background we observe today. Over time, the dark matter perturbations and baryonic matter perturbations converged, both growing under their combined gravitational attractions and eventually developing the sites of the first stars and galaxies.

Thus, baryonic acoustic oscillations are detectable not only in the CMB anisotropies, which measure the photon perturbations directly, but also as a subtle bump in the distribution of matter in configuration space (or a series of wiggles in Fourier space), which is dominated by the initial dark matter perturbations but also contains the BAO signature as a density excess at the characteristic scale of 150 h^{-1}Mpc.

BAO as a standard ruler

Proposals for using BAO as a statistical standard ruler to constrain cosmology were first developed in Eisenstein et al. 1998, Eisenstein 2003, and Blake & Glazebrook 2003. Letting

[3]Scattering between photons and protons was negligible compared to the scattering between photons and electrons because the Thomson cross section is proportional to the inverse of the mass squared and protons are over a thousand times more massive than electrons.

the characteristic BAO scale defined by the sound horizon be s, with s very well calibrated by the structure of the peaks in the CMB, we have

$$d_A(z) = \frac{s_\perp(t_{\rm then})}{\theta} = \frac{s_\perp(t_{\rm now})}{\theta(1+z)} \tag{2.17}$$

where $s_\perp(t_{\rm now}) = s_\parallel(t_{\rm now}) \approx 150\ h^{-1}$Mpc. Therefore,

$$s_\perp(t_{\rm now}) = (1+z)d_A(z)\theta = d_M(z)\theta \tag{2.18}$$

Meanwhile, the line-of-sight co-moving distance is given by

$$s_\parallel(t_{\rm now}) \approx \frac{c\ dz}{H(z)} \tag{2.19}$$

Thus, by observing the BAO peak in the two-point correlation function and measuring both its transverse and line-of-sight modes, we have a means to measure $d_A(z)$ and $H(z)$ simultaneously, giving unique constraints on dark energy. As previously discussed, BAO can generally be described with linear theory; however, at low redshifts, the nonlinear growth of structure can cause systematic errors in the measurement of the position and shape of the acoustic peak. Peculiar velocity flows from gravitational forces and small-scale clustering affect the separations between matter by as much as $\sim 10\ h^{-1}$Mpc. Eisenstein et al. 2007 and Padmanabhan et al. 2012 lay out a straightforward framework for reversing these displacements and reconstructing the initial positions. Reconstruction is able to dramatically undo the degradation of the BAO signal, and is now a standard part of BAO analysis pipelines.

Current status and future of BAO measurements

The first clear detection of the BAO peak in the galaxy two-point correlation function was obtained over a decade ago using a catalog of 46,748 luminous red galaxies at $z \sim 0.35$ from the Sloan Digital Sky Survey (Eisenstein 2005). Concurrently, BAO features were found in the power spectrum of galaxies at $z \sim 0.2$ from the Two-degree-Field Galaxy Redshift Survey (Cole et al. 2005). Since then, several measurements of the BAO scale at a range of redshifts $z < 1$ have been made (and subsequently refined) with precision at the level of a few percent using newer galaxy surveys such as the Six-degree-Field Galaxy Survey (Beutler et al. 2011), the WiggleZ Dark Energy Survey (Blake et al. 2011, Kazin et al. 2013), the Baryon Oscillation Spectroscopic Survey (BOSS) (Anderson et al. 2012, Anderson et al. 2014, Tojeiro et al. 2014, Alam et al. 2017), and the extended Baryon Oscillation Spectroscopic Survey (eBOSS) (Bautista et al. 2018). In addition, quasars have enabled measurement at higher redshift, not only as biased tracers of dark matter at intermediate redshifts $1 < z < 2$ (Ata et al. 2018, Zhu et al. 2018) but also as probes of the distribution of neutral hydrogen through their Lyman-α features, enabling measurements out to $z \approx 2$ (Busca et al. 2013, Slosar et al. 2013, Kirkby et al. 2013, Font-Ribera et al. 2014b, Delubac et al. 2015, Bautista

et al. 2017, du Mas des Bourboux et al. 2017), something that only recently became possible when BOSS dramatically increased the number density of observed quasars.

The next generation of dark energy experiments will measure BAO at even higher precision and significance. In this work, we focus on DESI, which will provide an order of magnitude improvement over BOSS in both the volume and the target density of the three-dimensional map it creates, enabling sub-percent precision distance measurements from BAO at more than thirty redshifts. Figure 2.1 shows the expansion history of the Universe as determined from past BAO measurements as well as measurements from Type Ia supernovae (the premier standard candle method). Expected constraints from the DESI BAO measurements are included, showing how DESI will be able to, for the first time, distinguish between dark energy models with very subtle effects on the cosmic expansion.

To obtain the unprecedented precision that DESI hopes for in its BAO measurements, all possible sources of observational error must be controlled and corrected for, ideally with a minimum loss of the survey volume and target density that gives DESI its competitive edge. Furthermore, the galaxy bias of each target class must be well understood in order to relate its observed correlation function to the clustering of dark matter. Targets for which reliable spectroscopic redshifts are not obtained will have additional uncertainty in the radial direction, with the BAO analysis requiring $\sigma_z/(1+z) \sim 0.0005$. In this thesis, we present our contributions towards reducing systematic errors, characterizing galaxy samples, and quantifying and reducing redshift uncertainty in galaxies without spectroscopy.

2.4 Redshift-Space Distortions

In addition to BAO, DESI will also measure redshift-space distortions (RSD) from the anisotropic clustering of galaxies. RSD helps constrain the growth of structure, which probes dark energy in a very complementary way to the distance measurements discussed in the previous section; while distance measurements predict the growth of structure under the assumption of unmodified general relativity (GR), measurements of the growth of structure for a given cosmic expansion history are sensitive to deviations from GR. In the following section, we briefly review the theory behind RSD and then summarize the current status and DESI projections of its measurement.

Measuring the growth of structure

Another way of probing dark energy is through its effects on the growth of structure. In particular, the function that charts the evolution of the amplitude of growth is dictated by the delicate interplay between gravity and expansion, and thus is an excellent probe of modified gravity models of dark energy. Under the assumption of standard GR, small matter density fluctuations $\delta = (\rho - \bar{\rho})/\bar{\rho}$ grow according to the equation

$$\ddot{\delta} + 2H\dot{\delta} - 4\pi G\rho\delta = 0 \tag{2.20}$$

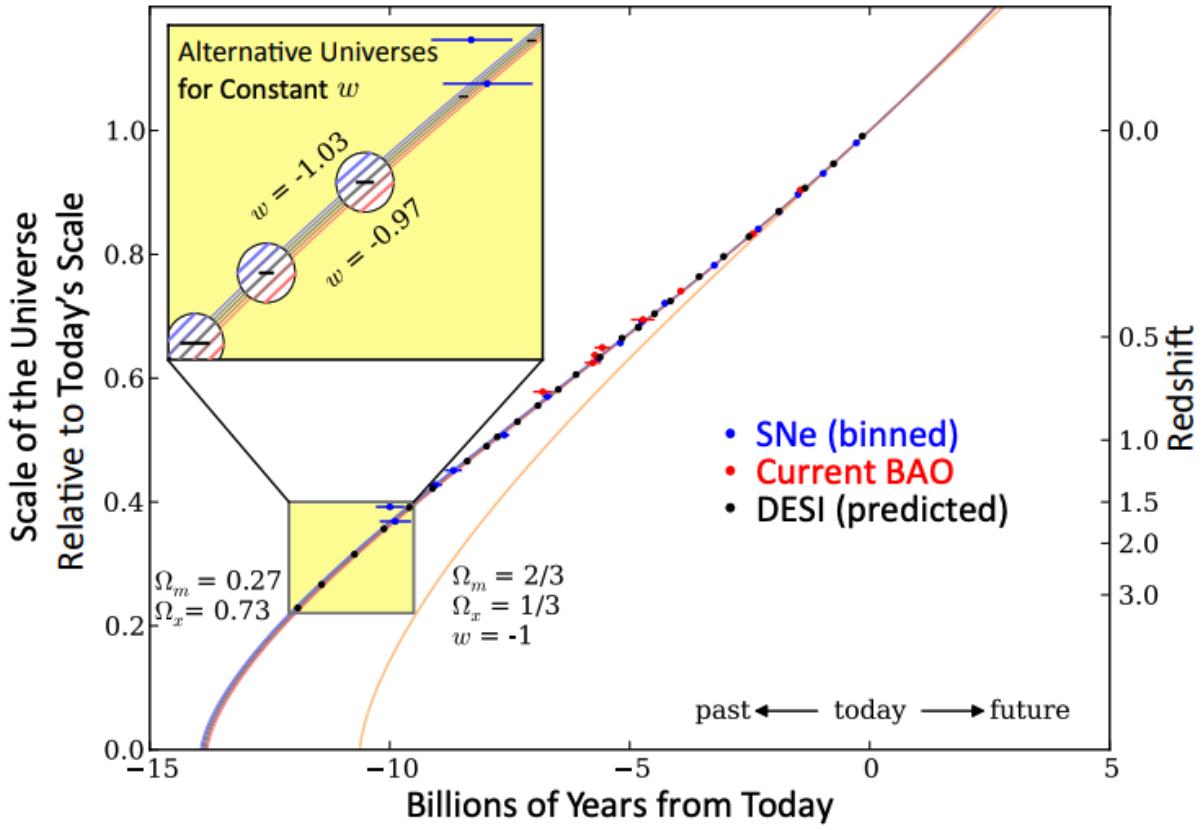

Figure 2.1: The expansion history of the Universe for different models of dark energy, with the inset showing the very fine spacing between cosmological models with slightly different values of w_Λ. Current measurements from supernovae (SNe) and BAO are overlaid in blue and red, respectively, while the DESI BAO projections are shown in black. *Source*: DESI Collaboration et al. 2016.

in the linear regime $|\delta| \ll 1$ (early times and large scales). Thus the linear growth in this framework can be modelled simply as

$$\delta(z) = D(z)\delta(z=0) \tag{2.21}$$

where $D(z)$ increases with decreasing redshift and is called, appropriately, the linear growth rate. Furthermore, under GR, $D(z)$ is entirely specified by the expansion history of the Universe, and is given approximately by

$$f \equiv \frac{d\ln D(a)}{d\ln a} \approx \Omega_m(z)^{\gamma\sim 0.55} \tag{2.22}$$

However, explanations for cosmic acceleration based on modifying GR on large scales will necessarily change these equations. A common parameterization of the modified growth rate under alternative theories of GR is to simple change the growth index γ. More generally, modified gravity could potentially introduce scale-dependence in $D(z)$. By constraining the growth of structure as a function of redshift, we can test these theories of modified gravity.

The origins and effects of RSD

Galaxy surveys measure redshifts, which are converted to distances assuming Hubble flow,

$$cz = H_0 d \tag{2.23}$$

Yet in addition to capturing the bulk recession due to cosmic expansion, redshifts also reflect small components of a galaxy's "peculiar velocity" sourced by local gravitational effects. More formally, we might say that the observation of the density field in redshift-space is a combination of the true real-space density and momentum fields. These peculiar velocities alter the apparent correlations between galaxies along the line-of-sight, leading to anisotropy in the observed clustering, as shown in Figure 2.2 and described below:

At larger scales, the coherent velocity of an infalling shell is small compared to its radius, so the shell appears squashed along the line-of-sight direction. This is called the Kaiser effect (Kaiser 1987). The squashing increases to smaller scales until "turnaround," when the peculiar infall velocity exactly cancels the Hubble expansion, making the structure appear pancake-flat. At small scales, when the peculiar velocity is great compared to its radius, the galaxy's coordinates seem to turn inside-out in redshift space. And at even smaller scales, galaxies inside virialized dark matter halos seem stretched out along the line of sight due to their random velocities in an effect known as Fingers of God (Jackson 1972).

Under the Kaiser approximation, to leading order, the density fluctuation in redshift-space is related to the real-space perturbation as

$$\delta_s(\vec{k}) = \delta(\vec{k})(1+\beta\mu^2) \tag{2.24}$$

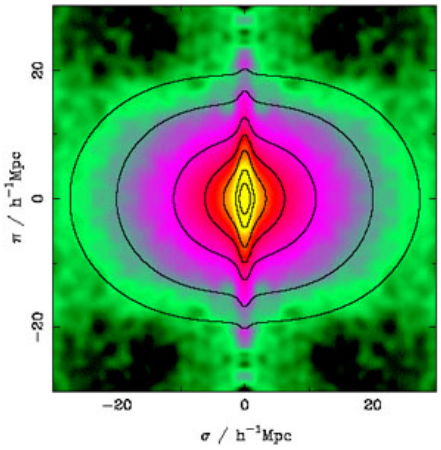

Figure 2.2: The two-dimensional correlation function in redshift-space of galaxies from 2dF-GRS, showing a range of RSD effects including the large-scale Kaiser effect as well as the small-scale Fingers of God effect. *Source*: Peacock et al. 2001.

where $\beta = f/b$ (with b being the galaxy bias) and μ is the directional cosine between the wave-number $\vec{k}$ and the line-of-sight direction. Written in terms of the power spectrum,

$$P_s(\vec{k}) = (b + f\mu^2)^2 P_m(k) \tag{2.25}$$

Thus for an assumed expansion history, measuring RSD in the galaxy correlation function can provide a unique prediction for the growth f, which must be measured across a wide range of scales and redshifts to robustly test GR. In practice, we see from Equation 2.25 that the measurement of f is degenerate with the overall normalization of the present-day linear matter power spectrum P_m, which is conventionally set at σ_8^2, with σ_8 defined as the amount of matter clustering averaged over a sphere of radius 8 h^{-1}Mpc. RSD provides constraints on the combined quantity $f\sigma_8$ as a function of redshift.

Current status and future of RSD measurements

Over the last decade, RSD studies have been performed by several recent surveys. For an assumed expansion history and flat ΛCDM cosmology, the resulting constraints on $f\sigma_8$ at a range of low redshifts are summarized in Table 2.1. DESI is expected to improve the precision of these constraints by a factor of 4-10 (Font-Ribera et al. 2014b). Due to its superior number density, DESI will be able to measure RSD in fine redshift bins, with predicted aggregate precision from the combined target classes $\sim 0.0035\%$ (Huterer et al. 2015). As most observational systematics are on large-scales and thus do not impact the RSD measurements significantly, the breakdown of the Kaiser approximation due to nonlinear effects is the central source of uncertainty. A large body of methods to correct for nonlinear complications using both theory and simulation exists in the literature, but accurate calibration of

Survey (Sample)	**z**	**fσ_8**	**Reference**
2dFGRS	0.17	0.51 ± 0.06	Percival et al. 2004
VVDS	0.77	0.49 ± 0.18	Guzzo et al. 2008
WiggleZ	0.22	0.42 ± 0.07	Blake et al. 2011
	0.41	0.45 ± 0.04	
	0.6	0.43 ± 0.04	
	0.78	0.38 ± 0.04	
6dFGRS	0.067	0.42 ± 0.06	Beutler et al. 2012
SDSS (LRG)	0.25	0.35 ± 0.06	Samushia et al. 2012
	0.37	0.46 ± 0.04	
VIPERS	0.80	0.47 ± 0.08	de la Torre et al. 2013
BOSS (CMASS)	0.57	0.45 ± 0.03	Samushia et al. 2014
FastSound	1.4	0.48 ± 0.12	Okumura et al. 2016

Table 2.1: Summary of $f\sigma_8$ constraints from RSD in past galaxy surveys

the mapping between galaxy clustering and dark matter clustering is crucial to all of them. Thus, characterizing the clustering of DESI targets is an important first step to obtaining accurate RSD measurements, and one that this thesis contributes towards.

Chapter 3

Imaging Systematics and Clustering of DESI Main Targets

In this chapter, we evaluate the impact of imaging systematics on the clustering of luminous red galaxies (LRG), emission-line galaxies (ELG) and quasars (QSO) targeted for the upcoming Dark Energy Spectroscopic Instrument (DESI) survey. Using Data Release 7 of the DECam Legacy Survey, we study the effects of astrophysical foregrounds, stellar contamination, differences between north galactic cap and south galactic cap measurements, and variations in imaging depth, stellar density, galactic extinction, seeing, airmass, sky brightness, and exposure time before presenting survey masks and weights to mitigate these effects. With our sanitized samples in hand, we conduct a preliminary analysis of the clustering amplitude and evolution of the DESI main targets. From measurements of the angular correlation functions, we determine power law fits $r_0 = 7.78 \pm 0.26\ h^{-1}$Mpc, $\gamma = 1.98 \pm 0.02$ for LRGs and $r_0 = 5.45 \pm 0.1\ h^{-1}$Mpc, $\gamma = 1.54 \pm 0.01$ for ELGs. Additionally, from the angular power spectra, we measure the linear biases and model the scale dependent biases in the weakly nonlinear regime. Both sets of clustering measurements show good agreement with survey requirements for LRGs and ELGs, attesting that these samples will enable DESI to achieve precise cosmological constraints. We also present clustering as a function of magnitude, use cross-correlations with external spectroscopy to infer dN/dz and measure clustering as a function of luminosity, and probe higher order clustering statistics through counts-in-cells moments.

3.1 Introduction

The Dark Energy Spectroscopic Instrument (DESI; DESI Collaboration et al. 2016) is a ground-based dark energy experiment whose mission is to produce the largest three-dimensional map of the Universe to date. This map will enable unprecedented constraints on dark energy (for a comprehensive review, refer to Weinberg et al. 2013 or Amendola et al. 2013) by charting the expansion history of the Universe through studies of baryon acoustic

oscillations (BAO; see Eisenstein 2005 or Bassett & Hlozek 2010 reviews) and constraining the growth of structure through redshift-space distortion measurements (RSD; see e.g. Ruggeri et al. 2019 for a recent study). In addition, it will provide a means to precisely measure the sum of neutrino masses (Font-Ribera et al. 2014a), and to investigate theories of inflation (Gariazzo et al. 2015, Tellarini et al. 2016) and modified gravity (Jain & Khoury 2010, Joyce et al. 2015, Casas et al. 2017, Amendola et al. 2019). Installed on the Mayall 4-meter telescope at Kitt Peak, DESI is a Stage IV dark energy project[1] consisting of a highly multiplexed fiber-fed spectrograph that can measure as many as 5000 spectra in parallel using robot fiber positioners. DESI will obtain spectra for four main target classes selected from imaging, including approximately 6 million luminous red galaxies (LRG) up to $z = 1.0$, 17 million [OII] emission-line galaxies (ELG) up to $z = 1.6$, and 2.5 million quasars (QSO). QSOs with $z < 2.1$ will serve as tracers of the underlying dark matter distribution, while a high redshift sample of QSOs ($2.1 < z < 3.5$) will be used for their Lyman-α absorption features to probe the distribution of neutral hydrogen in the intergalactic medium. During "bright time," when the position of the moon above the horizon impacts the observation of faint, high redshift targets, DESI will conduct the Bright Galaxy Survey (BGS), observing over 10 million galaxies up to $z \sim 0.4$, and also the Milky Way Survey (MWS) of local stars.

DESI is currently in its commissioning phase, with survey validation scheduled for the spring of 2020. At this stage of the project, it is vital to ensure that the targets selected from imaging will satisfy the science requirements of the collaboration, which demand meticulous control over all possible systematics. Since it is not obvious how systematics in the distribution of targets selected from imaging will translate to systematics in the 3D clustering of the spectroscopic samples, it is prudent to identify and mitigate them to the greatest extent possible. Furthermore, while acquiring spectra will allow us to remove any low redshift contaminants and deproject any purely angular systematics, the targeting efficiency of the survey will be adversely affected. In this chapter, we analyze the impact of potential systematics from imaging and target selection on the observed clustering of the main DESI samples and develop methods to ameliorate those effects. Using the resulting value-added large-scale structure catalogs, we begin to characterize the properties of these tracer samples, both as a first step for analysis in cosmological studies and to aid in generating accurate mock catalogs.

The chapter is organized as follows: Section 3.2 outlines our techniques for measuring and modeling clustering. Section 3.3 describes the imaging data and explains how we build our large-scale structure catalogs. In Section 3.4, we implement and test some preliminary survey masks; Section 3.4 deals with imaging completeness and its sensitivity to depth variations and color cuts, while Section 3.4 covers masking around bright foregrounds. In Section 3.5, we explore spatial variations in the clustering of the targets and identify additional problematic or anomalous regions. In Section 3.6, we investigate the effects of varying survey properties and instrument characteristics on the densities of targets, obtaining photometric weights for the most dominant systematics, with Section 3.6 focusing on the impact of stellar contamination in the QSO sample. Section 3.7 presents our preliminary characterization of

[1] As defined in the Dark Energy Task Force report (Albrecht et al., 2006).

the angular distribution of of the tracer samples, including mean surface densities, angular correlation functions, angular power spectra, linear biases, counts-in-cells moments, and clustering as a function of magnitude. In Section 3.8, we use external spectroscopic catalogs to measure real-space projected cross-correlations, clustering dN/dz, and clustering as a function of luminosity. Section 3.9 summarizes our results and conclusions.

Throughout, we will work in co-moving coordinates and assume a flat ΛCDM cosmology with $h = 0.676$, $\Omega_m h^2 = 0.142$, $\Omega_b h^2 = 0.022$, $n_s = 0.962$, and $\sigma_8 = 0.848$ (the default parameters in `CLASS`, see e.g. Blas et al. 2011). Additionally, all magnitudes are quoted as AB magnitudes, unless otherwise specified.

3.2 Clustering Measurement and Theory

To characterize the properties of DESI main samples and understand how systematics impact their observed distributions, we must be able to accurately quantify clustering as well as compare our results to theoretical predictions and survey expectations. To convert between angular clustering measurements and 3D clustering theory in Section 3.7, we assume the fiducial redshift distributions in the DESI Science Final Design Report (DESI Collaboration et al. 2016, henceforth FDR), calculated from cross-matching and photometric methods (private communications: Rongpu Zhou, Anand Raichoor, and Nathalie Palanque-Delabrouille for the DR7 LRG, ELG, and QSO dN/dz, respectively). These redshift distributions are plotted in Figure 3.25. In Section 3.8, we use cross-correlations with external spectroscopy to obtain clustering dN/dz.

Angular correlation functions

One of the simplest and most powerful measurements of clustering is the two-point correlation function $\xi(r)$, which measures the excess probability, compared to a random Poisson distribution, that a pair of objects lie at a given separation (see e.g. Peebles 1980, Peacock 1999). The two-point correlation function and its Fourier transform, the power spectrum, fully characterize a Gaussian random field. For samples that lack redshifts, the 2D angular correlation function $w(\theta)$, representing the probability in excess of random of finding two objects separated by a given angle, may be used instead.

Pair-count estimators

We measure $w(\theta)$ of the targets with direct pair-count estimators, namely the Landy-Szalay estimator (Landy & Szalay, 1993)[2],

$$\hat{w}_{LS}(\theta) = \frac{D_1 D_2 - D_1 R_2 - D_2 R_1 + R_1 R_2}{R_1 R_2} \tag{3.1}$$

[2]Normalization factors are not included here.

where DD, DR, and RR respectively refer to counts of data-data, data-random, and random-random pairs at average separation θ (within annular bins $\theta \pm \delta\theta$). For auto-correlations, this simplifies to $\hat{w}_{LS}(\theta) = (DD - 2DR + RR)/RR$. When cross-correlating with external data sets that don't have a corresponding random catalog readily available, we instead use the Davis-Peebles estimator (Davis & Peebles, 1983),

$$\hat{w}_{DP}(\theta) = \frac{D_1 D_2 - D_2 R_1}{D_2 R_1} \tag{3.2}$$

which has a slightly larger variance (see Landy & Szalay 1993 for a comparison of pair-count estimators) but only requires one set of randoms. We count pairs within 16 logarithmically spaced angular bins between $\theta = 0.001°$ and $\theta = 1°$.

Limber approximation

We wish to generate a prediction for the observed angular clustering of objects in the sky, $w(\theta)$, given an assumed model for the full three-dimensional clustering, $\xi(r)$, and redshift distribution, dN/dz. An approximation first introduced by Limber (1953) and Rubin (1954) is frequently employed for this purpose. Briefly, the Limber approximation assumes redshift distributions that do not vary appreciably over the coherence length of the structures defined by $\xi(r)$. Though not a requirement, it is often further assumed that the sky may be treated as flat. In this section, we state the general result, as well as the simplified expression for the case of a power-law $\xi(r)$. A more detailed derivation can be found in e.g. Simon (2007) or Loverde & Afshordi (2008).

Written in center-of-mass and relative coordinates, $\bar{r} = (r_1 + r_2)/2$ and $\Delta r = r_2 - r_1$, the Limber approximation straightforwardly relates the angular and spatial correlations between two samples,

$$w_{1,2}(\theta) = \int_0^\infty d\bar{r}\ f_1(\bar{r})\ f_2(\bar{r}) \int_{-\infty}^\infty d\Delta r\ \xi_{1,2}(R, \bar{r}) \tag{3.3}$$

where f_1 and f_2 are the normalized radial distributions, and $R = \sqrt{\bar{r}^2\theta^2 + \Delta r^2}$. If we further presume a power-law for the correlation function, with correlation length r_0,

$$\xi(r) = \left(\frac{r}{r_0}\right)^{-\gamma} \tag{3.4}$$

then we can evaluate the Δr integral directly, and Limber's approximation gives a particularly simple result,

$$\begin{aligned} w_{1,2}(\theta) &= \theta^{1-\gamma}\ r_0^\gamma \sqrt{\pi}\ \frac{\Gamma(\gamma/2 - 1/2)}{\Gamma(\gamma/2)} \int_0^\infty d\bar{r}\ f_1(\bar{r})\ f_2(\bar{r})\ \bar{r}^{1-\gamma} \\ &\equiv A_w \theta^{1-\gamma} \end{aligned} \tag{3.5}$$

Using this equation with tabulated dN/dz's, we can compare observation to theory by determining the clustering length r_0 and slope γ that best fit the observed $w(\theta)$.

Projected real-space cross-correlations

We can extract additional clustering information by cross-correlating the samples with other samples of known redshift. We begin by deriving a relation between the angular correlation function $w(\theta)$ and the projected real-space correlation function $w_p(r_p)$, the latter being defined as the integral of the 2D spatial correlation function $\xi(r_\pi, r_p)$ over the line of sight r_π (Davis & Peebles, 1983).

Starting with the simple case in which the spectroscopic sample lies at $\chi = \chi_0$, the flat-sky approximation yields

$$w(\theta) = \int d\chi f(\chi) \xi\left(\sqrt{\chi_0^2\theta^2 + (\chi - \chi_0)^2}\right) \tag{3.6}$$

where $f(\chi)$ is the normalized radial distribution of the photometric sample, and the second integral over the radial distribution of the spectroscopic sample, a delta function, has been performed. Applying the Limber approximation (Section 3.2), this simplifies to

$$\begin{aligned} w(\theta) &\simeq f(\chi_0) \int dr_\pi \xi(r_p, r_\pi) \\ &= f(\chi_0) w_p(r_p) \end{aligned} \tag{3.7}$$

where $w_p(r_p)$ is a real-space measurement, since redshift space distortions only affect r_π.

Generalizing to a narrow spectroscopic redshift slice, such that the clustering can still be treated as constant over the slice, we adopt the approach of Padmanabhan et al. (2009): for each pair in a given bin, we assume the photometric object lies at the same redshift as the spectroscopic object it is being correlated with, allowing us to re-bin the pair counts in transverse separation, $w_\theta(r_p)$, such that Equation 3.7 becomes

$$w_\theta(r_p) = \big\langle f(\chi) \big\rangle w_p(r_p) \tag{3.8}$$

where $\big\langle f(\chi) \big\rangle$ is averaged over the spectroscopic redshift bin in question and $w_\theta(r_p)$ is the angular correlation function but binned in physical distance instead of angle using the redshifts of the spectroscopic objects for conversion.

To compare with theory, we note also the form $w_p(r_p)$ takes for a power-law correlation function model $\xi(r) = (\frac{r}{r_0})^{-\gamma}$:

$$w_p(r_p) = r_p^{1-\gamma} r_0^\gamma \sqrt{\pi} \frac{\Gamma(\gamma/2 - 1/2)}{\Gamma(\gamma/2)} \tag{3.9}$$

Bootstrap errors

As an internal error estimate, we use the bootstrap technique of Efron (1979), splitting the sample into multiple subsamples and then randomly selecting with replacement to obtain many different realizations of the underlying distribution. Since resampling on individual

objects has been shown to lead to unreliable errors (Mo et al. 1992, Fisher et al. 1994), with variance underestimated in underdense regions and overestimated in overdense regions, we instead partition the sky into equal area pixels and resample these.

The choice of the bootstrap over similar methods such as the jackknife is motivated by comparative studies (e.g. Norberg et al. 2009) suggesting that, though the bootstrap tends to overestimate variance on all scales, it recovers the principal eigenvectors of the true covariance matrix in an unbiased fashion. As such, we caution that our bootstrap error bars are likely overestimated in some cases.

In detail, we use the `HEALPix` package[3] (Górski et al., 2005) with $N_{\rm SIDE} = 4$ to divide the surface of a sphere into 192 equal area pixels of approximate size ∼215 sq deg, then throw away any pixels that do not overlap with the footprint, leaving 83 pixels. We then randomly select pixels with replacement until the number of randoms in each bootstrap realization is similar to the number of randoms in the footprint. We use 500 bootstrap realizations to obtain an estimate of the variance. Our results are robust to variations in the $N_{\rm SIDE}$ resolution and the number of bootstrap realizations.

Angular power spectra

The angular power spectrum, C_ℓ, is another powerful tool for quantifying clustering, allowing us to study the Fourier modes of the angular distribution of galaxies. It complements the statistical information derived from the angular correlation function, to which it is related via a Legendre transform:

$$w(\theta) = \sum_\ell \frac{2\ell+1}{4\pi} P_\ell(\cos\theta) C_\ell \tag{3.10}$$

Large-scale systematics are more clearly visible in the power spectrum than in the correlation function, which potentially has long-wavelength modes affecting all angular scales. On the other hand, the correlation function is more sensitive to small scales, where nonlinear evolution dominates and introduces correlations between different C_ℓ's at large ℓ. Additionally, it is faster to compute small-scale clustering in configuration space and large-scale clustering in Fourier space. Thus, we focus our analysis of the angular power spectrum on large scales $\ell \leq 500$, corresponding to angular scales greater than $\theta \sim 180°/\ell \approx 0.4°$, or spatial scales greater than a few h^{-1} Mpc at the characteristic survey depth of 1 h^{-1} Gpc.

Measurement

We use `HEALPix` with $N_{\rm SIDE} = 512$ and estimate the angular power spectrum from harmonic analysis of the pixelised map of density contrast $\delta_g = n/\bar{n} - 1$, where n is the number of galaxies in a given pixel and $\bar{n}$ is the average density over the entire masked sample multiplied by the given pixel's effective area. We mask out pixels whose effective area is less than 25% of its full area, such that only pixels which are fully (or mostly) inside the survey geometry

[3] http://healpix.sf.net

are considered[4]. Using `anafast`, we obtain the estimated angular power spectrum C_ℓ, which is the sum of the signal and the shot noise. To first-order correct the effects of partial sky, we divide by a factor of $f_{\rm sky}$, the fraction of sky covered by the masked footprint; full deconvolution of the mask is deferred to a future work. We find that the angular power spectrum of the mask has its power concentrated in the large-scale modes, with the mask dropping to half power at $\ell \sim 10$ and falling below 10% power beyond $\ell \sim 20$. We also divide out the pixel window function. The variance of the estimator can be modelled analytically as

$$\sigma_\ell^2 = \frac{1}{f_{\rm sky}} \frac{2C_\ell^2}{2\ell+1} \tag{3.11}$$

On a small section of sky ϕ, multipole resolution is limited by $\Delta\ell \approx 180^\circ/\phi$, with the $\ell_{\rm min}$ mode constrained to be the wavelength that fits into the angular patch (Peebles, 1980). We bin C_ℓ using 10 linearly spaced bins from $\ell_{\rm min} = 30$ to $\ell_{\rm max} = 500$ and take the weighted arithmetic mean and variance for each bin.

$$\begin{aligned} \bar{C}_{\rm bin} &= \frac{\sum_{\ell \text{ in bin}} \frac{C_\ell}{\sigma_\ell^2}}{\sum_{\ell \text{ in bin}} \frac{1}{\sigma_\ell^2}} \\ \frac{1}{\sigma_{\rm bin}^2} &= \sum_{\ell \text{ in bin}} \frac{1}{\sigma_\ell^2} \end{aligned} \tag{3.12}$$

Theory

In the first-order correction to the Limber approximation (Loverde & Afshordi, 2008), the multipole expansion of the galaxy angular power spectrum is given by

$$\begin{aligned} C_\ell &= \int d\chi \; f(\chi)^2 \frac{1}{\chi^2} P_g(k = (\ell+1/2)/\chi, z) \\ &= \int d\chi \; f(\chi)^2 \frac{b(z)^2}{\chi^2} P_m(k = (\ell+1/2)/\chi, z) \end{aligned} \tag{3.13}$$

where $f(\chi) \equiv dN/d\chi = dN/dz \frac{H(z)}{c}$ is the normalized radial distribution, P_m is the linear dark matter power spectrum, and $b(z)$ is the large-scale bias, which we assume takes the form[5] $b(z) = b_0/D(z)$ as per the DESI FDR. In Section 3.7, we fit the linear bias b_0 and also explore the scale-dependence of the bias in the weakly nonlinear regime.

[4]Since effective area is calculated using a set of uniformly distributed random points, there is some natural Poisson variance, hence why we do not use a more restrictive threshold.

[5]$D(z)$ is the linear growth function with normalization $D(z=0) = 1$. Thus the approximation $b \propto D^{-1}(z)$ assumes that the clustering is constant, since the evolution of $P(k,z)$ is cancelled by the evolution of $b^2(z)$.

Clustering dN/dz

Overview

The idea of using cross-correlations to infer redshift information about objects in the night sky has been circulating for decades (e.g. Seldner & Peebles 1979, Phillipps & Shanks 1987, Landy et al. 1996, Ho et al. 2008), but has received renewed attention in the context of modern astronomical surveys, which are probing deeper than ever and imaging far more objects than can feasibly be targeted for spectroscopic observation. In recent years, a number of dN/dz cross-correlation estimators have been proposed and studied (Newman 2008, Matthews & Newman 2010, Schulz 2010, Matthews & Newman 2012, McQuinn & White 2013, Ménard et al. 2013) and applied to real or simulated data (Schmidt et al. 2013, Scottez et al. 2016, Hildebrandt et al. 2017, Scottez et al. 2018, Davis et al. 2018, Gatti et al. 2018, Chiang et al. 2018, Krolewski et al. 2019). Following Ménard et al. (2013), which presents a simple and practical method for estimating the clustering dN/dz of a sample, we probe the redshift distributions of objects targeted for DESI in Section 3.8. Unlike other methods, the Ménard method takes advantage of small-scale clustering information and reduces the impact of systematics by sidestepping autocorrelation functions. We briefly describe the formalism of Ménard method and the details of our implementation below.

Method

Consider two populations. Let the reference (spectroscopic) sample have a redshift distribution dN_r/dz, a mean surface density $\bar{n}_r$, and a total number of objects N_r. The corresponding properties for the unknown (photometric) sample will be labeled dN_u/dz, $\bar{n}_u$, and N_u, respectively. The angular cross-correlation between the reference sample and the unknown sample is estimated by

$$w_{ur}(\theta, z) = \frac{\langle n_u(\theta, z) \rangle}{\bar{n}_u} - 1 \tag{3.14}$$

where $\langle n_u(\theta, z) \rangle$ is the mean surface density of objects from the unknown sample lying within an angular distance θ of objects in the reference sample at redshift z. To calculate this, we bin the reference sample into narrow redshift bins δz_i. Then, for each δz_i, we estimate $w_{ur}(\theta, z_i)$ by pair counting with the Davis-Peebles estimator Equation 3.2.

In practice, we actually integrate over an annulus around each reference object, from $\theta_{\rm min}$ to $\theta_{\rm max}$, because the sensitivity of the estimator is improved by encoding information from many clustering scales (Ménard et al., 2013). In order to maximize the SNR, we weight each point by θ^{-1}, which gives equal amounts of clustering information per logarithmic scale ($d\theta/\theta = d\log\theta$).

$$\bar{w}_{ur}(z) = \int_{\theta_{\rm min}}^{\theta_{\rm max}} d\theta \, \frac{w_{ur}(\theta, z)}{\theta} \tag{3.15}$$

To avoid excess signal from cross-correlations between duplicate objects that appear in both catalogs, it is necessary to impose a minimum radius, $\theta_{\rm min}$ which is at least as large as the

astrometric uncertainties in the survey. Furthermore, as we go to smaller scales < 1 Mpc, clustering becomes increasingly nonlinear and bias becomes increasingly scale-dependent, so the assumptions underpinning the estimator break down, potentially affecting the accuracy of the result. Finally, we note that as the scale falls below the mean separation of spectroscopic objects, cross-correlations between redshift bins become more significant. Meanwhile, at larger scales, the advantage of a linear bias[6] must be balanced against the cost of degraded signal-to-noise since the clustering signal decreases with radius and the noise due to systematics increases as more background sources are included in the counts. Thus, for samples which have little to no bias evolution, small scales are ideal for recovering dN/dz; for samples with some bias evolution, intermediate scales are recommended; and for samples with extensive bias evolution, restricting to large scales may be the best strategy.

Counts-in-cells

To aid in simulations, we wish to also provide some measurement of the higher order clustering statistics of the DESI samples. In particular, for regions of high density, spectroscopic incompleteness due to the physical limitation of fiber allocation is expected to introduce systematic effects on the observed clustering (Cahn et al. 2017, Burden et al. 2017, Pinol et al. 2017) which must be included in any realistic mock catalog. Thus, rich clustering information down to the scale of the DESI fiber patrol radius of $1.4'$ is invaluable for the purpose of mock calibration and validation.

Since a discrete map of galaxies or quasars samples the continuous density field of matter, the number of galaxies within a randomly placed cell (counts-in-cells: Hubble 1934; White 1979; Peebles 1980) provides a window into the higher-order correlations. Let $P(N)$ be the probability that a cell with area Ω contains exactly N galaxies. The factorial moments of this distribution, $F_p = \langle N(N-1)...(N-p+1)\rangle$, are related to the corresponding moments of the spatially smoothed underlying density field, $\overline{\mu}_p = \langle(1+\delta)^p\rangle$, via the simple relation $\overline{\mu}_p = \frac{F_p}{\langle N\rangle^p}$, which tidily includes shot noise corrections arising from the fact that we are dealing with a discrete, locally Poissonian representation of the continuous field (Szapudi & Szalay 1993a, Szapudi et al. 1996). From these moments, we can extract the correlation functions of corresponding order (also smoothed over the characteristic cell size), $\overline{w}_p(\Omega) = \frac{1}{\Omega^p}\int_\Omega d\Omega_1...d\Omega_p w_p(\theta_1,...,\theta_p)$. The first few are listed below (e.g. Fry 1985, Fry et al. 2011):

$$\begin{aligned}\overline{\mu}_2 &= 1+\overline{w}_2\\ \overline{\mu}_3 &= 1+3\overline{w}_2+\overline{w}_3\\ \overline{\mu}_4 &= 1+6\overline{w}_2+3\overline{w}_2^2+4\overline{w}_3+\overline{w}_4\end{aligned} \tag{3.16}$$

Szapudi & Colombi (1996) classifies theoretical errors on counts-in-cells statistics as either cosmic errors (due primarily to shot noise, edge effects, and finite volume) or measurement

[6]The bias measured by these angular cross-correlations is dominated by scales of hundreds of kpc to a few Mpc, and thus should be distinguished from the large-scale (>10 Mpc) bias, which may evolve differently.

errors (due to the finite number of sampling cells), the latter scaling as the inverse of the number of sampling cells used. The counts-in-cells distribution and its moments are usually determined by throwing random cells over the region of interest, with massive oversampling required to control the measurement errors. However, Szapudi (1998) describes a method of implementing counts-in-cells that is essentially equivalent to using an infinite number of random cells, thereby eliminating the measurement error entirely. We implement this method using our publicly available code `infcic`[7]. Therefore, we present only the uncertainty associated with cosmic errors, which we approximate by calculating counts-in-cells over two large fields, one in each galactic hemisphere, and measuring the mean and dispersion, weighted by effective area.

3.3 Imaging Catalogs

Imaging data

The DECam Legacy Survey (DECaLS) is a wide-field photometric survey amassing deep multicolor imaging within the footprints of ongoing and future spectroscopic surveys. Using the DECam instrument (Flaugher et al., 2015) at the Blanco 4m telescope, DECaLS observed in three optical/near-infrared bands (g, r, z), complemented by four mid-infrared bands from the Wide-field Infrared Survey Explorer (WISE; Wright et al. 2010). DECaLS aims to obtain images up to 5σ point-source depths $g = 24.7$, $r = 23.9$, and $z = 23.0$ AB mag, and is designed to boost the science power of spectroscopic observations by providing publicly available imaging with superior depth (1-2 magnitudes fainter) and enhanced image quality compared to existing photometry from SDSS, ATLAS, and Pan-STARRS. DECaLS covers a large equatorial region (bounded by $\delta < 32°$ in galactic coordinates), corresponding to roughly two-thirds of the optical imaging used for DESI targeting, and is a key piece of the Legacy Survey project, which has imaged the full 14000 square degrees of extragalactic sky making up the DESI survey (Dey et al., 2018).

Raw DECam images are processed through the NOAO Community Pipelines, with astrometric calibration and photometric characterization based on Pan-STARRS-1 measurements. The calibrated images are then run through *The Tractor*[8] (Lang et al., 2016), which produces an inference-based catalog by optimizing the likelihood for source properties, given the data and a noise model. We use Data Release 7 (DR7), the seventh public data release of the Legacy Survey, which is the last DECaLS-only data release, including observations from August 2013 through March 2018 (NOAO survey program 0404). It also uses non-DECaLS observations from DECam conducted between August 2013 and March 2018, including some data from the Dark Energy Survey (DES; DES Collaboration et al. 2005). Together, these cover approximately 9766 square degrees in the g-band, 9853 square degrees in the r-band,

[7] https://github.com/ekitanidis/infcic
[8] https://github.com/dstndstn/tractor

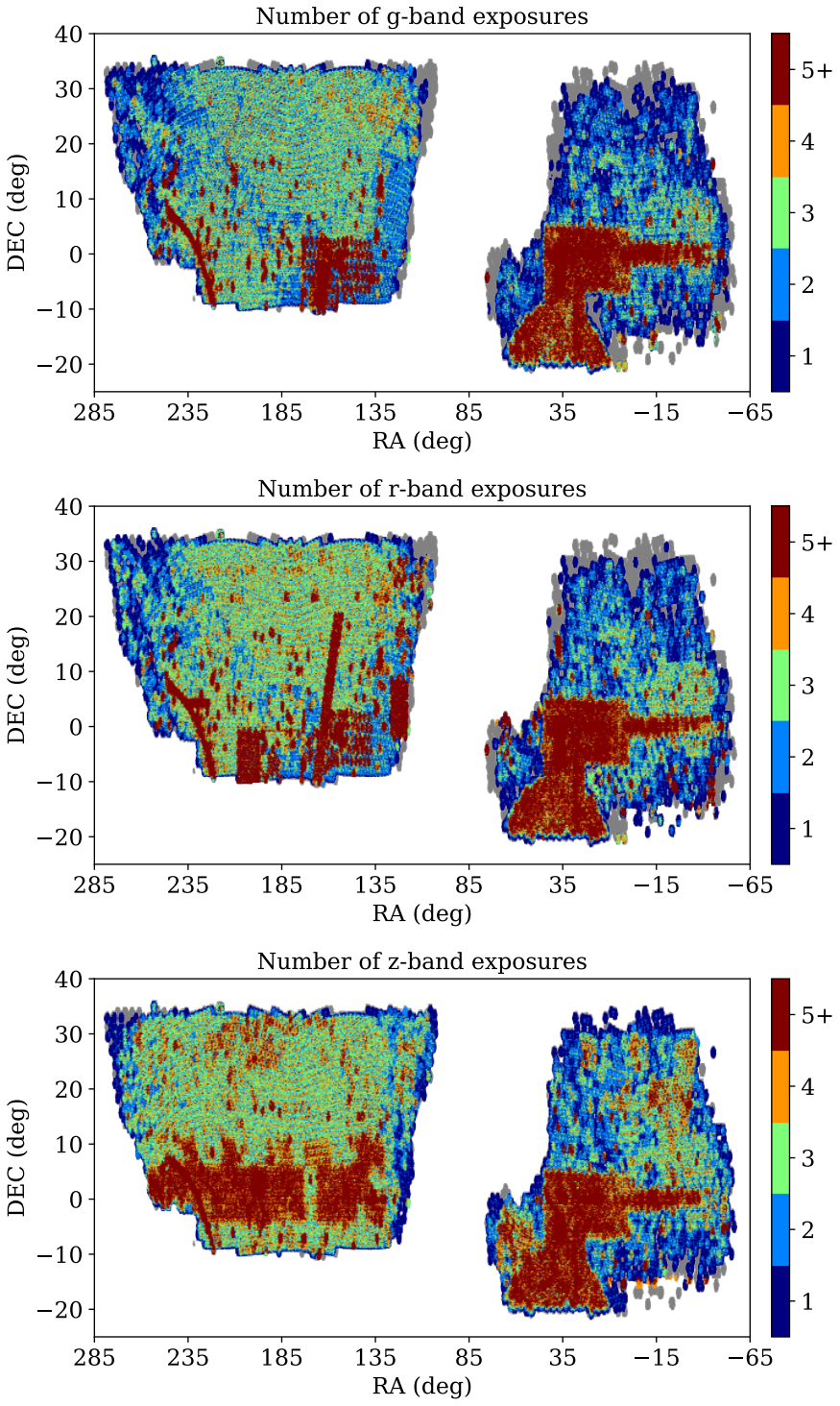

Figure 3.1: Number of exposures in each DECaLS band in DR7, estimated by sampling the footprint with randoms. No map projection is applied here.

N_{EXP}	f_{sky}				Area (deg^2)			
	g	r	z	all	g	r	z	all
0	0.14	0.11	0.05	1.0	1572.5	1263.8	541.6	11243.6
1	0.17	0.14	0.11	0.82	1865.1	1529.1	1292.5	9273.5
2	0.23	0.21	0.18	0.63	2620.5	2329.9	2035.4	7114.6
3	0.2	0.22	0.24	0.39	2279.5	2430.0	2665.8	4380.5
4	0.09	0.11	0.16	0.19	1032.8	1274.3	1846.3	2185.9
5+	0.17	0.21	0.25	0.11	1873.2	2416.5	2861.9	1220.6

Table 3.1: Area and sky fraction covered by *exactly* 0,1,2,3,4,5+ exposures in each optical band in DECaLS DR7. The "all" columns are cumulative, such that the $N_{EXP} = 1$ row refers to area and sky fraction covered by *at least* one exposure in all bands. Areas are estimated by sampling the footprint with randoms. In this context, the sky fraction is defined relative to the total DECaLS footprint, whereas elsewhere in the chapter, it is defined relative to the area where imaging exists ($N_{EXP} > 0$) in all three optical bands.

Target	Redshift range	Selection bands	
		Primary	Other
LRG	0.4 - 1.0	z	g, r, $W1$
ELG	0.6 - 1.6	g	r, z
QSO (tracers)	< 2.1	r	g, z, $W1$, $W2$
QSO (Ly-α)	2.1 - 3.5	r	g, z, $W1$, $W2$

Table 3.2: Summary of selection properties for each of the dark time DESI target classes. $W1$ and $W2$ denote WISE bands. "Primary" refers to the band used to define the limiting magnitude, which is relevant for the completeness mask (see Section 3.4).

and 10610 square degrees in the z-band, with 9298 square degrees observed in all three optical bands (see also Table 3.1, Figure 3.1).

Target selection

Table 3.2 summarizes the primary target types evaluated in this chapter. These targets are defined in great detail in the FDR and their selection algorithms are briefly outlined below.

LRG

LRG targets are selected from the g, r, z, and $W1$ bands by applying a series of color cuts using extinction-corrected magnitudes. No morphology cut is applied.

$$\begin{gathered} 18.01 < z < 20.41 \\ 0.75 < r - z < 2.45 \\ -0.6 < (z - W1) - 0.8\,(r - z) \\ (z - 17.18)\ /\ 2 < r - z < (z - 15.11)\ /\ 2 \\ (r - z > 1.15)\ \ ||\ \ (g - r > 1.65) \end{gathered} \tag{3.17}$$

ELG

ELG targets are selected from the g, r, and z bands by applying a series of color cuts using extinction-corrected magnitudes. No morphology cut is applied.

$$\begin{gathered} 21.00 < g < 23.45 \\ 0.3 < (r\ -\ z) < 1.6 \\ (g\ -\ r) < 1.15\,(r\ -\ z) - 0.15 \\ (g\ -\ r) < 1.6 - 1.2\,(r\ -\ z) \end{gathered} \tag{3.18}$$

QSO

QSO targets are selected by applying a machine learning method based on Random Forests (RF) which relies only on extinction-corrected object colors in the g, r, z, W_1, W_2 bands (Christophe Yèche, private communication). The algorithm is trained using all known QSOs in the footprint with an initial cut of $r < 23$ against a sample of unresolved objects from Stripe 82 without known QSOs and objects exhibiting QSO-like variations in their light curves. In the target selection itself, a tighter initial cut of $r < 22.7$ is applied.

Catalogs and randoms

DESI target catalogs and uniform random catalogs are created with our public code `ImagingLSS`[9]. `ImagingLSS` processes the outputs of the DECaLS pipeline and selects DESI targets from it, as well providing the option for auxiliary, user-defined targets. Uniform unclustered randoms are sampled from the imaging survey footprint. Geometric survey masks (for example, vetoing by proximity to bright objects) can be applied to both catalogs and randoms in a consistent manner. In addition to DECaLS data, `ImagingLSS` uses the SFD98 dust map (Schlegel, Finkbeiner & Davis, 1998) to correct for extinction, as well as the Tycho-2 star catalog (Høg et al., 2000) and the AllWISE catalog (Cutri et al., 2015) to mask out bright stars.

[9] https://github.com/desihub/imaginglss

Target	Mask	Number	Area (deg^2)	$f_{\rm sky}$
LRG	no mask	4882206	9298.91	1.0
	complete only	4872537	9281.0	1.0
	bright star only	4304375	8584.68	0.92
	all masks	4296486	8568.65	0.92
ELG	no mask	23224353	9298.91	1.0
	complete only	23032874	9227.78	0.99
	bright star only	20329143	8638.84	0.93
	all masks	20166887	8575.15	0.92
QSO	no mask	3125148	9298.91	1.0
	complete only	3116976	9288.35	1.0
	bright star only	1814359	6655.11	0.72
	all masks	1810801	6648.68	0.71

Table 3.3: Summary of masks and how each affects the number of targets and the effective area and sky fraction. Here, sky fractions are quoted relative to the "no mask" case, which is simply the joint regions of the footprint where imaging is available in all three optical bands.

3.4 Imaging Masks

We develop two types of initial masks, completeness and bright star, to reject possibly problematic regions of the imaging data. The effects of these masks on the survey efficiency and effective area are summarized in Table 3.3. Our baseline sample is selected from regions where imaging exists in all three optical bands used for targeting ("no mask"), and all sky fractions are quoted relative to this sample. In subsequent sections, we will review the purpose and implementation of each mask, with Section 3.4 focused on imaging completeness, and Section 3.4 describing our bright star mask. We also investigate whether there is need for a mask around extended sources such as large galaxies.

Survey depth and completeness

Tractor catalogs contain an estimation of the imaging depth at each observed pixel in the footprint. This depth is affected by the number of exposures, exposure times, observational

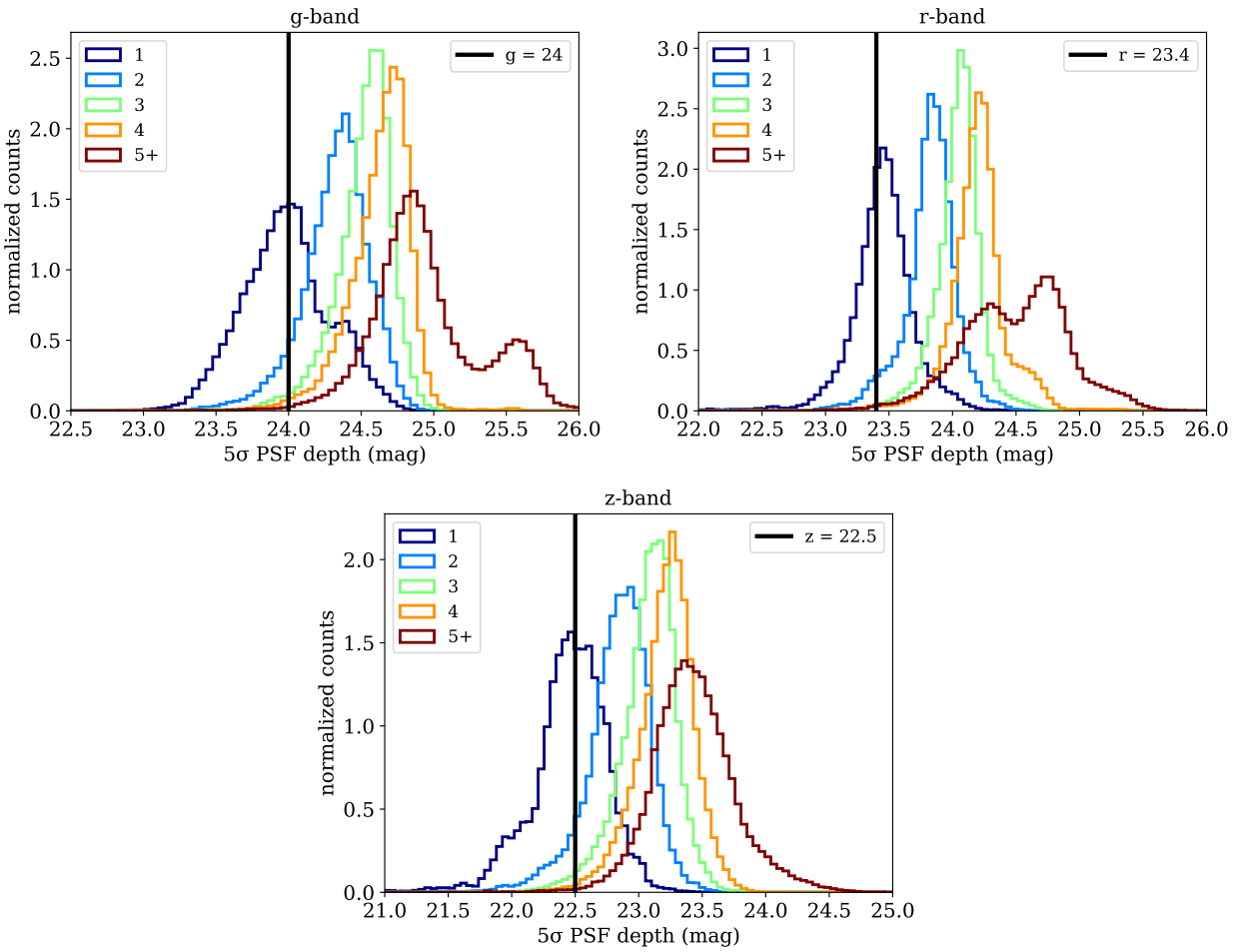

Figure 3.2: Histograms of 5σ point-source depths of randoms in each band, normalized as probability densities, with the colored curves corresponding to different numbers of exposures. The solid vertical lines are the DESI nominal 5σ depth requirements $g = 24.0$, $r = 23.4$, $z = 22.5$ for an ELG galaxy with half-light radius of 0.45 arcsec.

conditions, and instrument effects[10]. Due to the multi-pass nature of the imaging survey and the fact that it is ongoing, variations in depth across the footprint are substantial. In DR7, some of the sky has been covered just once, while the deepest regions have received five or more passes (see Table 3.1 and Figure 3.1).

To select a uniform and complete sample, we implement a "completeness" mask. Since two exposures, at minimum, are needed to meet the nominal depth requirements of DESI

[10]Note that we do not explicitly apply the `ALLMASK` flag, which uses the NOAO Community Pipeline's data quality map to mask out bad pixels on the CCD and pixels affected by bleed trail, transients such as cosmic rays, and saturation. These effects are accounted for in the estimation of the depths (Dey et al., 2018) and thus are perforce included in our completeness mask.

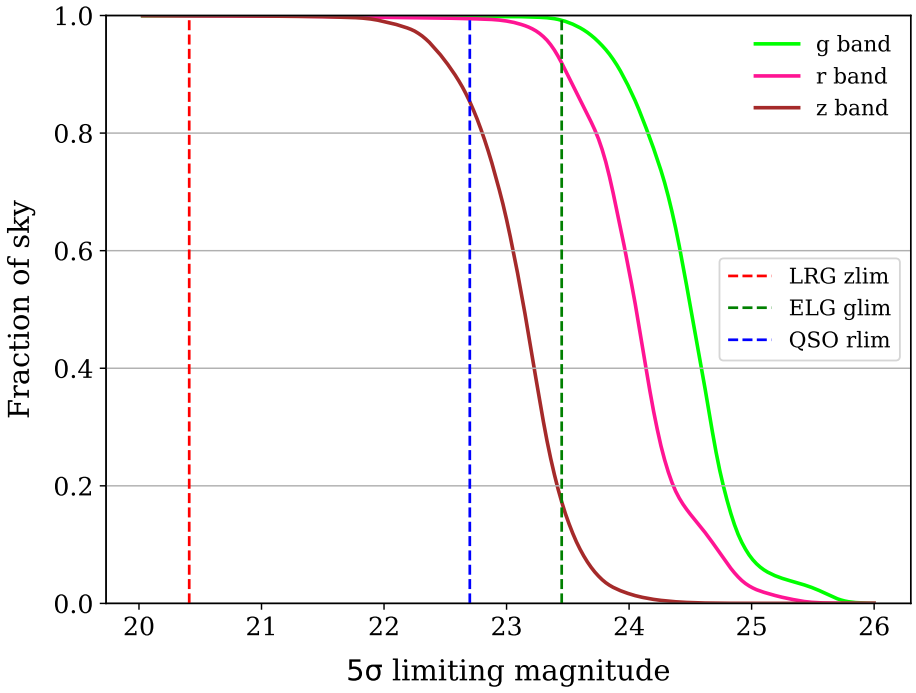

Figure 3.3: Cumulative sky fraction vs. 5σ limiting magnitudes, with target selection cuts shown as vertical lines to demonstrate the effect that shifting a magnitude limit up or down would have on the completeness of the corresponding target.

over most of the footprint (Dey et al., 2018), a reasonable approach might be to mask out areas with fewer than two exposures in each band. However, not every pixel will exceed target depth for a given number of overlapping exposures (see Figure 3.2), and thus the result will still be biased towards regions with more passes. Even with perfectly uniform coverage, variations in observing conditions affect depths and therefore the homogeneity of the resulting catalog.

Instead, using the 5σ point-source depths as limiting magnitudes, combined with DESI target definitions, we construct a "binary completeness mask," in which a particular observed pixel is in the "complete" area for a target type if and only if it meets the following conditions:

1. the limiting magnitudes in the bands used for magnitude cuts are sufficient to observe even the faintest targets with 5σ confidence;

2. imaging exists for all bands used in the target definitions.

This ensures that only the "deep enough" regions of the sky are used to generate DESI catalogs and randoms for analysis. Figure 3.3 shows the sky fraction as a function of depth for each band, with the magnitude cuts for the three targets plotted as vertical lines, to

visualize how shifting a magnitude cut up or down would affect usable sky area. As Figure 3.3 shows, all depths are sufficient to detect the full target samples.

By only requiring the existence of imaging in the bands used for color cuts, we are implicitly assuming that uncertainties in the colors do not affect the reliability of the target selection. Alternatively, we could require a 5σ detection in all bands, not just the primary bands used to apply magnitude cuts. However, it is not clear how to define a detection limit in a band that is only used for color cuts, as the targets are not necessarily bounded in these bands. The other advantage of defining the completeness mask on only the bands used for magnitude cuts is that it makes it easier to apply the definition to target selections of finer granularity in the color space, for example, represented by a forest of decision trees.

Bright foregrounds

As discussed in Section 3.3, we correct for galactic extinction by adjusting the color of objects using the SFD98 dust map. In addition to extinction, bright objects in the foreground (point sources such as stars, and extended sources such as nearby galaxies) can also affect the detection of targets in their angular vicinity, due to CCD saturation and diffraction spikes that contaminate the surrounding pixels. The systematics due to these bright objects in the target catalogs are spatially localized and uncorrelated with the underlying true density of the targets. Thus, we can quantify these systematic effects by measuring the densities of targets as a function of their proximity to the bright foreground objects, and mitigate them via masks.

Bright stars

We use two bright star catalogs, Tycho-2 and WISE. Tycho-2 is a reference catalog of the 2.5 million brightest stars in the sky, with photometry in two optical bands, $\lambda_{BT} = 435$ nm and $\lambda_{VT} = 505$ nm. It has highly accurate astrometric positions and is 99% complete out to $VT \sim 11$ magnitude, making it well suited to our analysis. However, some stars not included in the Tycho-2 catalog may still be bright enough in the near-infrared bands to affect the detection of LRGs and QSOs, both of which use the WISE band $W1$ in their target selection (QSOs also use $W2$). To be safe, we create separate veto masks for each star catalog and apply both to our data. Table 3.4 compares the effective areas and sky fractions of the two star masks.

For both catalogs, we follow a similar procedure to construct and test a radial mask for each target class. We begin by splitting the sample of stars into magnitude bins, since the masking radius will be magnitude-dependent. The bin widths are chosen such that each bin contains a similar number of stars and therefore has comparable Poisson errors. For a given magnitude bin, we use the pair-enumeration algorithm in `KDcount`[11] to efficiently locate all star-galaxy pairs within a distance of $\theta = 0.05$ rad $\approx 10^4$ arcsec of one another. We calculate

[11] https://github.com/rainwoodman/kdcount

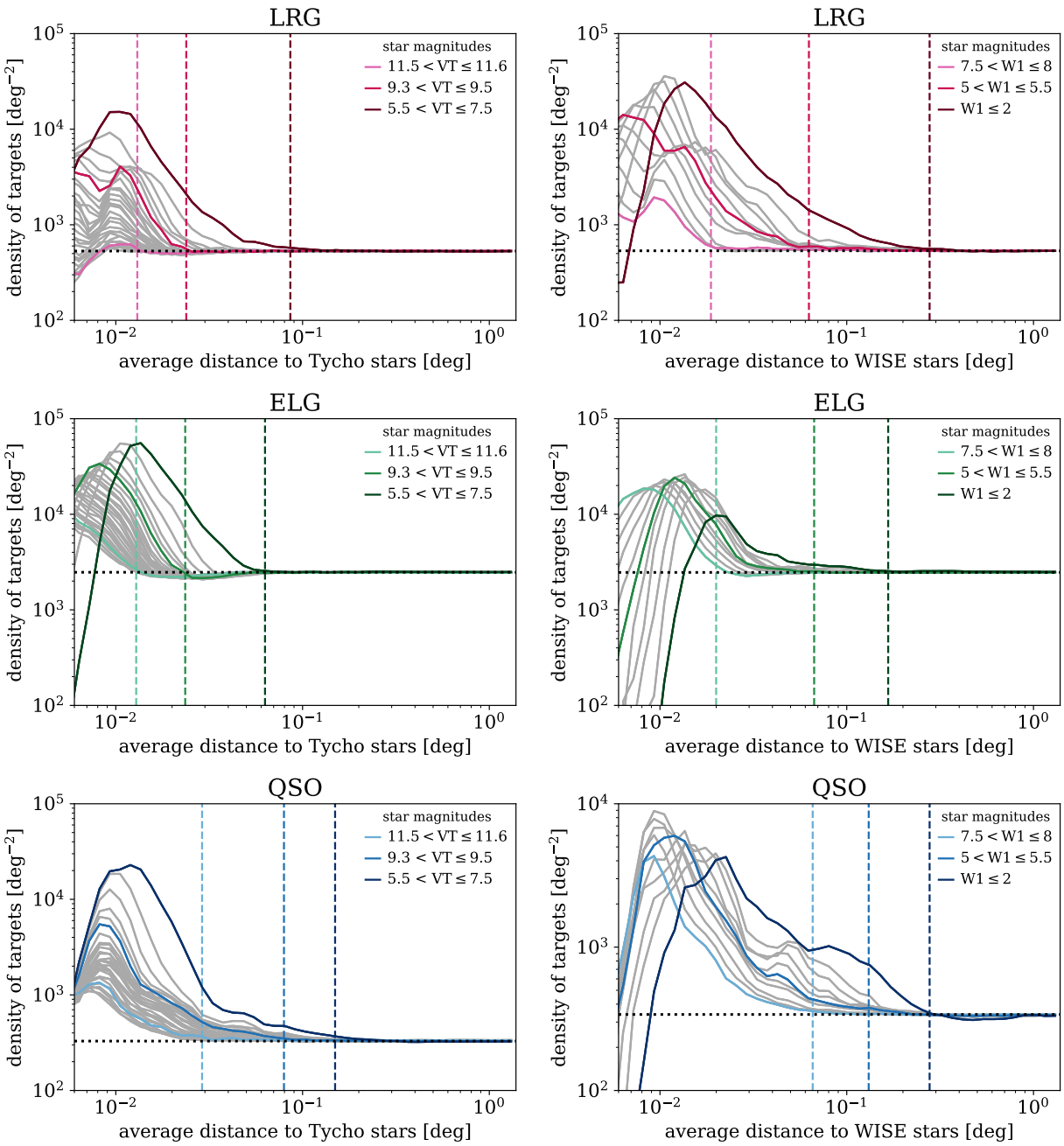

Figure 3.4: Average density of DESI targets as a function of distance to bright stars from Tycho-2 (left) and WISE (right). Both star catalogs are divided into magnitude bins, which are spaced such that each contains a roughly comparable number of stars. In each plot, three bins are highlighted for illustration, with the dashed vertical lines representing the corresponding masking radius (Equations 3.19 and 3.20) calculated using the average magnitude of that bin.

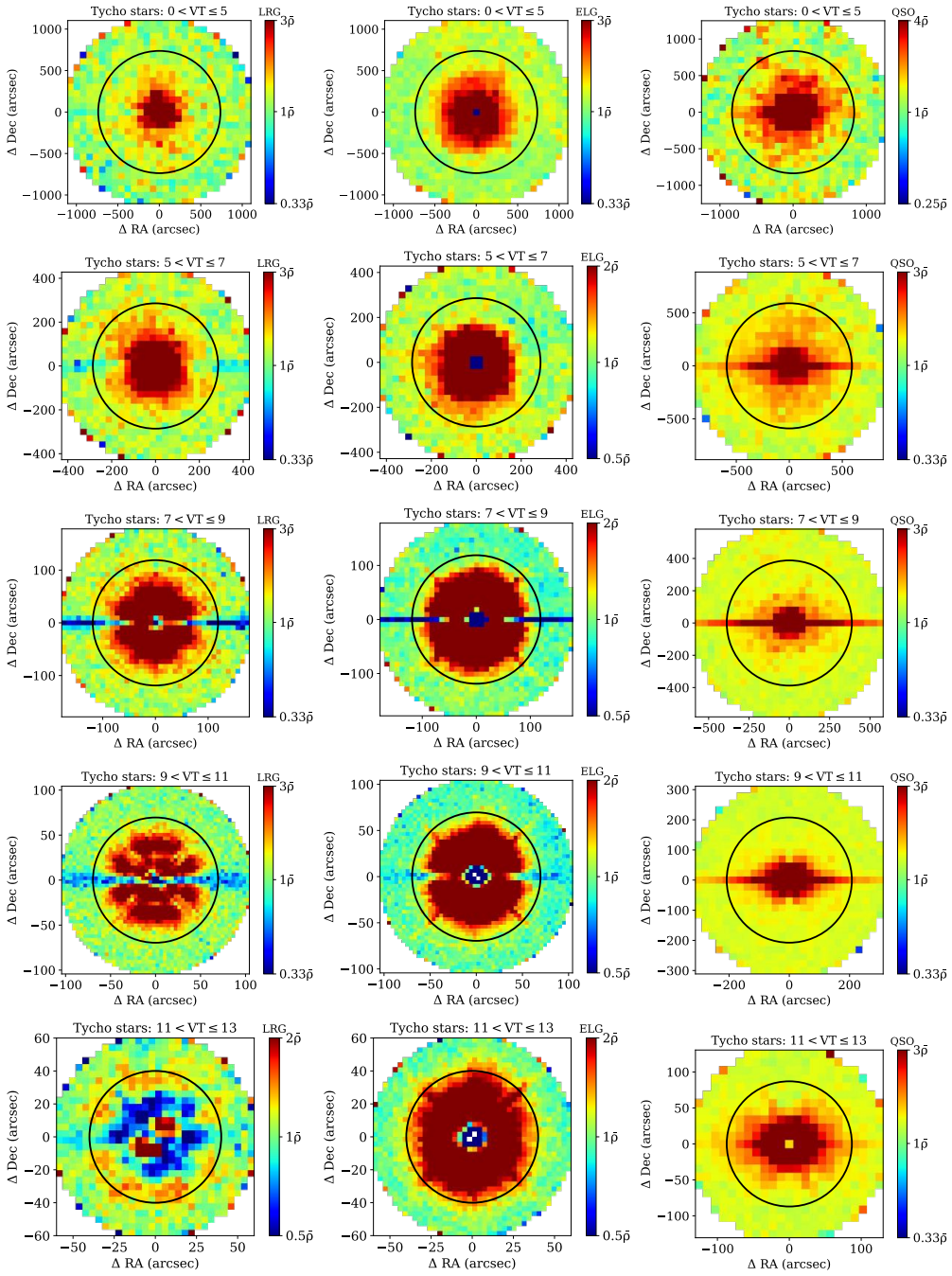

Figure 3.5: 2D histograms of the density of DESI targets around stacks of bright stars from Tycho-2. The solid black circles represent our star masks (Equation 3.19). The horizontal features appearing in some maps, which are due to insufficient masking of charge bleed trails in the CCDs, are only a few arcsec in width, and we find that removing them with a separate rectangular mask has no perceptible impact on the densities around stars.

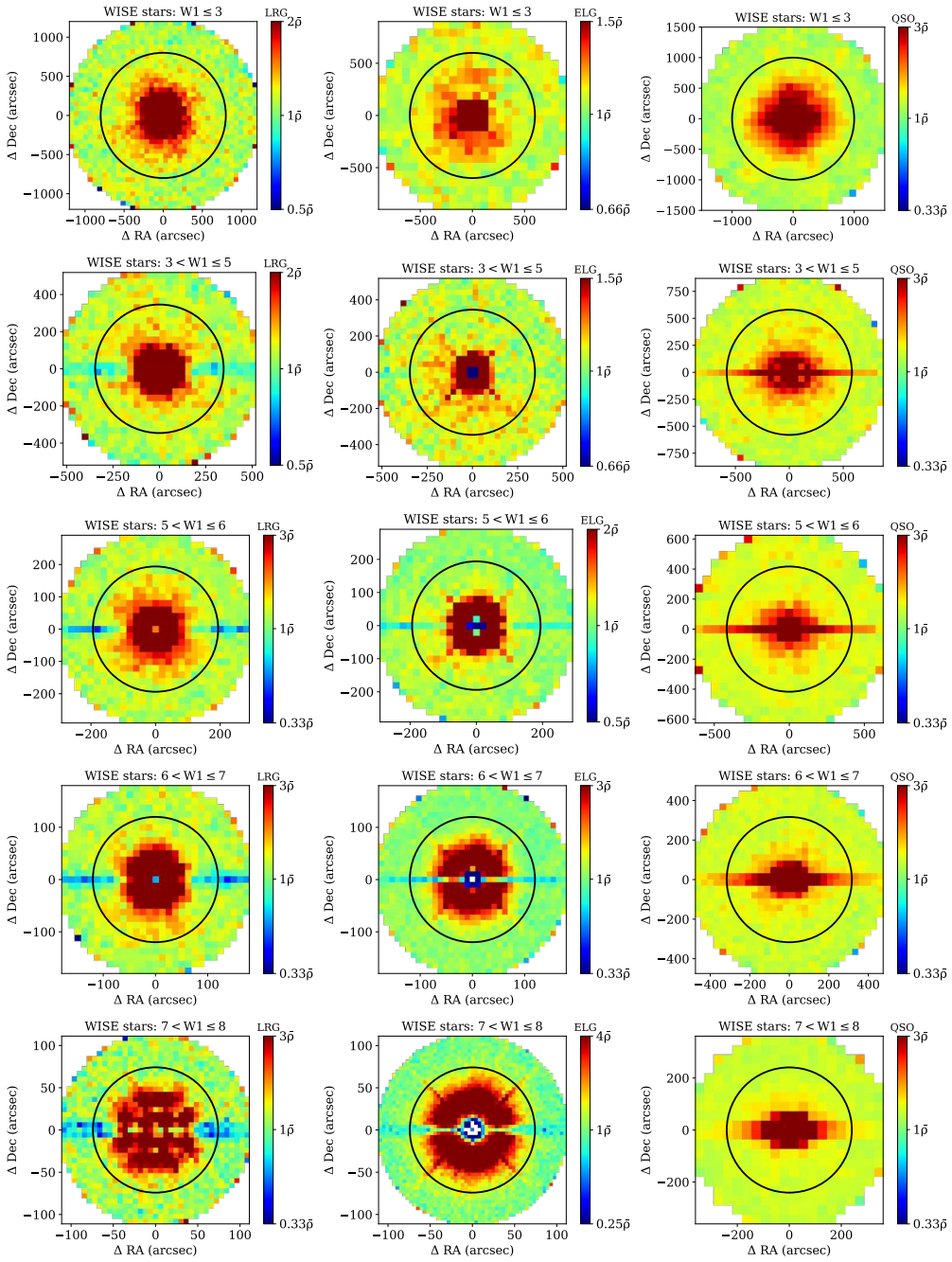

Figure 3.6: 2D histograms of the density of DESI targets around stacks of bright stars from WISE. The solid black circles represent our star masks (Equation 3.20). The horizontal features appearing in some maps, which are due to insufficient masking of charge bleed trails in the CCDs, are only a few arcsec in width, and we find that removing them with a separate rectangular mask has no perceptible impact on the densities around stars.

Target	Mask	Number	Area (deg^2)	$f_{\rm sky}$
LRG	no mask	4882206	9298.91	1.0
	Tycho mask only	4385463	8752.25	0.94
	WISE mask only	4529935	8970.73	0.96
	both star masks	4304375	8584.68	0.92
ELG	no mask	23224353	9298.91	1.0
	Tycho mask only	21378695	8811.44	0.95
	WISE mask only	21065984	8970.73	0.96
	both star masks	20329143	8638.84	0.93
QSO	no mask	3125148	9298.91	1.0
	Tycho mask only	2192932	7541.98	0.81
	WISE mask only	2030414	7269.13	0.78
	both star masks	1814359	6655.11	0.72

Table 3.4: Summary of star masks and how each affects the number of targets and the effective area and sky fraction. Here, sky fractions are quoted relative to the "no mask" case, which is simply the joint regions of the footprint where imaging is available in all three optical bands.

the density of targets around each star in logarithmically-spaced annular bins up to this maximum separation, then average across all stars to determine the mean density of targets in each annular bin. By assigning a conservative cutoff radius to each magnitude bin by eye and fitting the results, we obtain the following magnitude-radius relations:

For Tycho-2:

$$R = \begin{cases} -2.5 \times VT^3 + 77.4 \times VT^2 \\ \quad -813.6 \times VT + 2969 \text{ arcsec}, & \text{LRG, ELG} \\ 2.8VT^2 - 143.4VT + 1387.1 \text{ arcsec}, & \text{QSO} \end{cases} \tag{3.19}$$

For WISE:

$$R = \begin{cases} 10^{\,3.29\,-\,0.18\,\times\,W1} \text{ arcsec}, & \text{LRG, ELG} \\ 10^{\,3.29\,-\,0.12\,\times\,W1} \text{ arcsec}, & \text{QSO} \end{cases} \tag{3.20}$$

For both types of star mask, the LRGs and ELGs can be fit to the same magnitude-radius relation, while the QSOs require their own, more conservative mask. We found that relaxing

the QSO stellar masks (by, for instance, applying the LRG/ELG masks instead) led to a measurable increase in stellar contamination, evidenced by inflated QSO autocorrelation and QSO-star cross-correlation measurements.

In our analysis, we implement Equations 3.19 and 3.20 instead of using the `MASKBITS` column provided by DECaLS to mask out stars. We have found that our geometric masks are more aggressive than the combination of available stellar bitmasks; in particular, they are necessary for removing contaminated areas at larger radii.

Figure 3.4 shows the resulting target densities vs. distance to bright stars, sectioned by target type and star catalog, with each magnitude bin plotted separately. Three bins are highlighted for illustration, with the corresponding dashed vertical lines representing the relevant masking radii calculated with the average magnitude of that bin. These plots show how the masks eliminate spurious clustering due to bright stars. In Figures 3.5 and 3.6, we also present 2D histograms of target densities around stacks of bright stars, plotted in equatorial coordinates[12] with star masks drawn on as circles, again showing well-fiting mask radii.

Bright extended sources

Similarly to bright stars, we examine the density of targets near bright extended sources such as nearby galaxies. We use the 2MASS Extended Source Catalog (Jarrett et al., 2000), a catalog of near-IR extended sources complete for angular sizes greater than ∼10 arcsec. Restricting to $10 < J < 15$ total J-band magnitude, we find no appreciable impact on the density of our DESI dark time targets (Figure 3.7), and thus we do not apply a mask.

3.5 Spatial Variations

NGC vs. SGC

We calculate the angular correlation functions in the north galactic cap (NGC) and the south galactic cap (SGC) individually, as the two hemispheres may suffer from different systematics, and earlier analyses have found NGC/SGC variations in BOSS data (see Ross et al. 2012 Section 4.1 for an explanation of the origin of this difference in number density between the NGC and SGC in BOSS). The results are shown in Figure 3.8. For LRGs, the autocorrelations are virtually identical. For ELGs, there is a slight divergence, most noticeably in the $0.02° < \theta < 0.09°$ range. For QSOs, the difference between NGC and SGC is significantly more pronounced. The NGC results appear more impacted by systematics, as indicated by a bulge in the correlation function with extremely large bootstrap errors. This is likely due to the fact that parts of the SGC, where there is DES imaging, are very

[12] We also performed this analysis in ecliptic coordinates, to see if additional structure could be identified. In some of the fainter magnitude bins, resolution and contrast could be manipulated to resolve an x-shaped feature in the 2D stacked plots, but this feature was very fine, and we found that removing it beforehand had no perceptible impact on the 1D density plots.

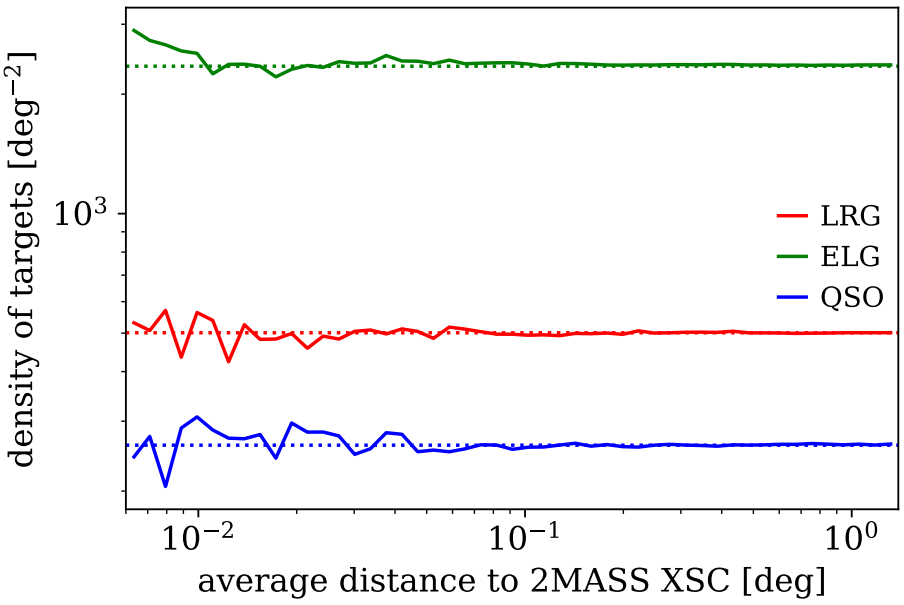

Figure 3.7: Average density of DESI dark time targets as a function of distance to extended sources from 2MASS-XSC.

deep (see also Figure 3.9 in the following section to visually observe how the NGC appears more impacted by systematics for QSO).

Visual inspection

As an initial sanity check, we create maps of the density contrast $\delta = n/\bar{n} - 1$ averaged over `HEALPix` pixels of $N_{\rm SIDE} = 256$. The results are shown in Figure 3.9, with the unmasked catalogs mapped on the left and their masked counterparts on the right. The masked catalogs are visually cleaner, with the star masks reducing stellar contamination and the completeness masks cancelling the imprint of imaging depth on target density. Several features remaining in the masked maps are highlighted and discussed below.

While LRG clustering appears relatively uniform, ELG clustering shows some troubling large-scale trends. For example, the shape of the DES region in the south is detectable, appearing under-dense despite its superior depth. This suggests contamination in non-DES regions, likely due to the effect of low redshift ($z < 0.8$) objects preferentially scattering into the ELG target selection across the low-z color cut $(g - r) < 1.15\,(r - z) - 0.15$ in regions of worse depth. This was tested (Ashley Ross, private communication) by injecting artificial noise into regions of very deep imaging and examining the photometric redshifts of the resulting scattered objects. Additionally, a few suspicious "hot spots" appear in the ELG density. When examined closely, most of these occur around a small set of very bright

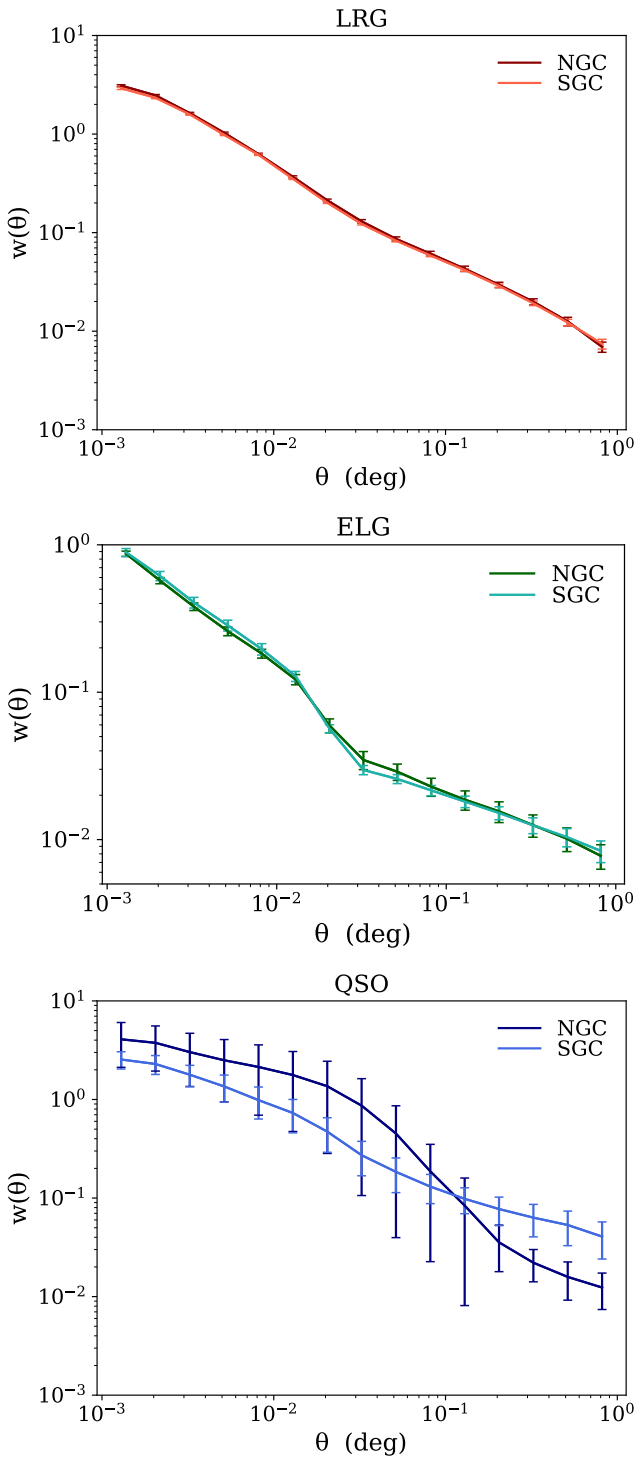

Figure 3.8: $w(\theta)$ for LRGs, ELGs, and QSOs calculated in NGC and SGC separately. Error bars are from bootstrapping.

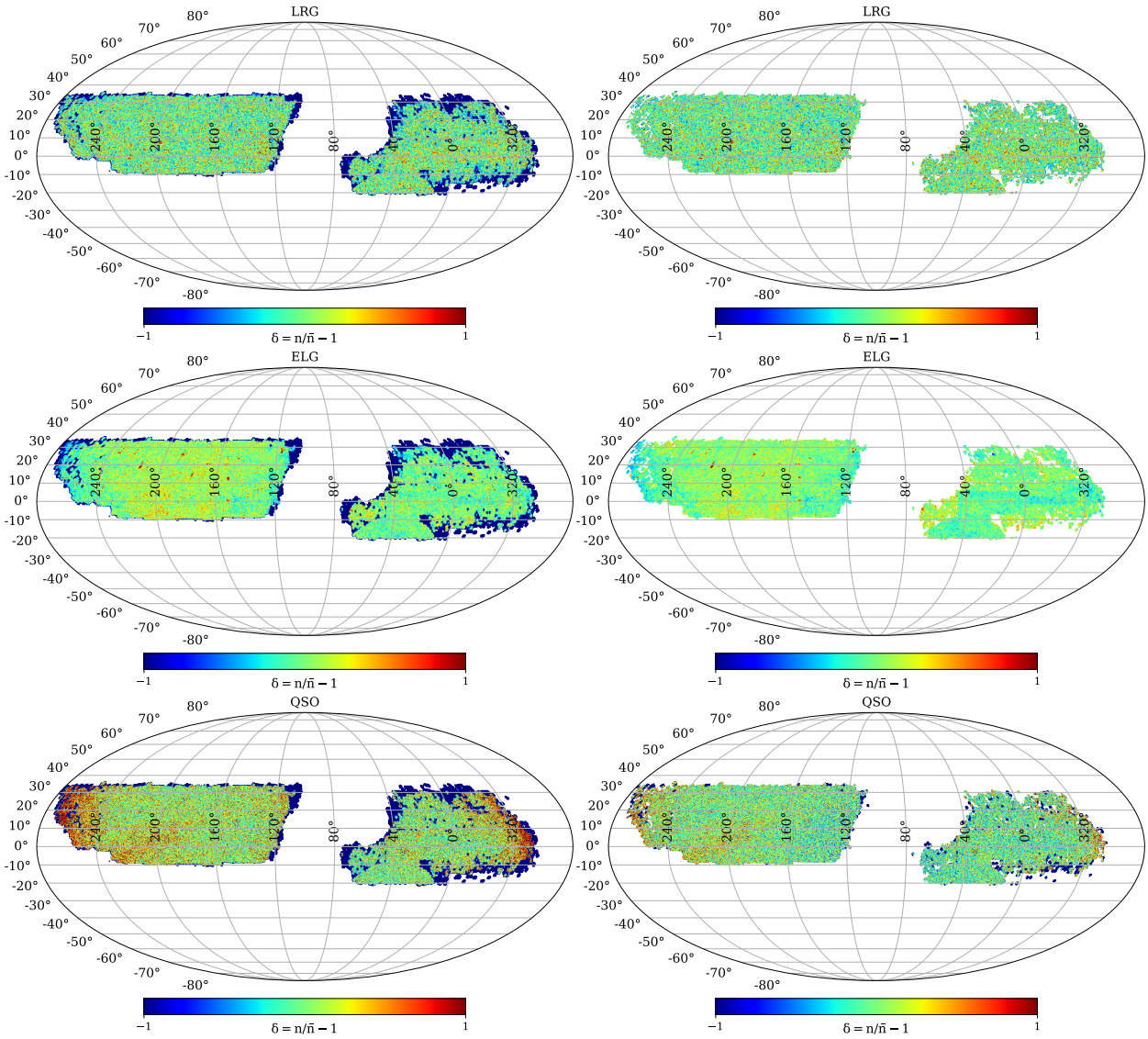

(a) Unmasked. (b) Masked.

Figure 3.9: Maps of the density contrast $\delta = n/\bar{n} - 1$ calculated with `HEALPix` resolution $N_{\mathrm{SIDE}} = 256$. Mollweide projection in equatorial coordinates with right ascension centered at RA = 100°. Masked data (right) is less impacted by stellar contamination and variations in imaging depth than raw data (left).

stars (such as Arcturus) which have been successfully masked, but which cause dramatic and complex artifacts in the image beyond the expected masking radius due to reflections of pupil ghosts. Finally, looking at the density of QSOs, there remains noticeable stellar contamination along the galactic plane even after applying conservative masks, as well as the Sagittarius Stream in the north, and there are also some effects at the edges of the footprint.

Outlier analysis

As another test of spatial variation, we perform a jackknife-inspired outlier analysis on the data. Again using the `HEALPix` scheme, we divide the footprint into large pixels and re-calculate $w(\theta)$ with each non-empty pixel excluded in turn, still performing the full bootstrap error analysis on the remaining pixels for each iteration. We begin with the coarsest pixels, corresponding to $N_{\rm SIDE} = 1$, and increase the resolution as needed to resolve any anomalies that are detected. For LRGs and ELGs, the results are indistinguishable even at this minimum resolution. However, for QSOs, we find two pixels at resolution $N_{\rm SIDE} = 4$ which, when either is excluded, lead to a significant change in the correlation function (see Figure 3.10). Likely culprits are the Coma Cluster (Abell 1656), which contains over 1,000 galaxies, and M3/NGC 5272, one of the largest and brightest globular clusters in the sky.

3.6 Potential Systematics

Potential systematics include astrophysical foregrounds, variations in observing conditions, and uncertainties in data calibration, processing, and reduction (for similar studies in the context of SDSS, see e.g. Myers et al. 2006, Crocce et al. 2011, Ross et al. 2011; for similar analyses using DES Verification Data, see e.g. Suchyta et al. 2016, Crocce et al. 2016, Leistedt et al. 2016, Elvin-Poole et al. 2018). We introduce maps of spatially-varying potential systematics in Section 3.6, and examine their impact on the densities of DESI targets, before and after applying photometric weights, in Section 3.6. The purpose of these weights is to mitigate the density trends by up-weighting (or down-weighting) regions where target density is diminished (or enhanced) due to systematics. Finally, in Section 3.6, we cross-correlate the targets with stars and attempt to quantify stellar contamination in the QSO sample.

Maps of potential systematics

We begin by using the `HEALPix` scheme with $N_{\rm SIDE} = 256$ to divide the data into equal-area pixels of approximately 0.05 square degrees each. This resolution was chosen to avoid the shot noise limit in which most pixels contain zero or one targets. For our LRG, ELG, QSO samples with approximate mean densities (per square degree) 500, 2400, and 260,

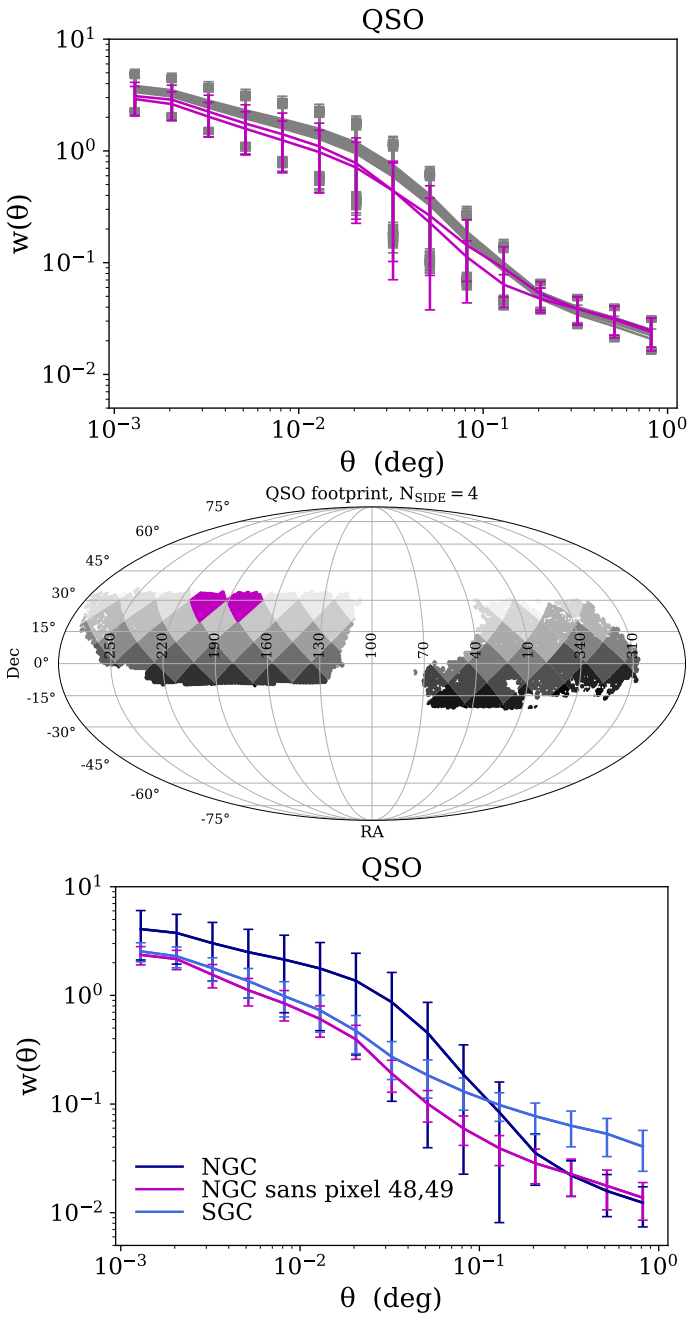

Figure 3.10: Upper: The angular correlation function is re-calculated with each pixel excluded in turn, still performing a complete bootstrap analysis on the remaining pixels. Two neighboring pixels in the NGC affect the result when either is excluded (violet lines). Middle: Map highlighting the location of the two pixels which were found to affect clustering. Lower: When both these pixels are excluded, the disparity between the NGC and SGC is dramatically reduced on small scales.

respectively, it produces an average of 10-20 LRGs/QSOs and ∼100 ELGs per pixel.[13] In every pixel, an average value for the potential systematic is calculated. For survey properties measured per CCD, unless otherwise noted, we first average over overlapping exposures to obtain a mean value for each random, then pixelise using the randoms. The resultant maps are shown below, along with brief descriptions of how they are determined and why they are included in the analysis.

1. Stellar density

   In addition to the detection issues near bright foreground stars discussed in Section 3.4, the presence of stars impacts the measured density and clustering of galaxies in other ways (e.g. Crocce et al. 2011, Ross et al. 2011). Stars with similar colors (see Figure 3.12) can contaminate the samples, and the inclusion of a separate population manifests as an enhanced clustering signal. The observed clustering may also be imprinted with the density gradient of stars, which increases towards the galactic plane. Furthermore, residual PSF tails of some fainter stars may pollute the pixels used to calculate sky background and therefore affect target photometry.

   We create a catalog of stars from DECaLS by selecting objects lying in the stellar locus (using the color cut $17 < r < 18$) with PSF morphology. The density of this class of objects, shown in the top left panel of Figure 3.11, indicates that it is a reliable stellar template.

2. Galactic extinction

   Galactic extinction is the wavelength-dependent absorption and scattering of light by interstellar dust in the Milky Way, causing sources to appear redder. DESI and its imaging surveys deliberately avoid regions of high extinction along the galactic plane. In addition, we use extinction-corrected fluxes in our analysis. The total extinction in each band is provided by the DECaLS pipeline, calculated from the SFD98 dust map combined with a set of extinction coefficients A_λ/E_{B-V} for each DECam and WISE filter. The extinction coefficients were determined at airmass = 1.3 from the values recommended by Schlafly & Finkbeiner (2011) using the Fitzpatrick (1999) extinction curve at $R_V = 3.1$. These values are 3.214, 2.165, 1.211 for g, r, z. However, it has been shown in other surveys that residual errors in this correction may cause spurious clustering (see e.g. Scranton et al. 2002, Myers et al. 2006, Ross et al. 2006). In addition, erroneously correcting the photometry of stars in the foreground of the dust could potentially bias their color and cause some of them to scatter into target selection. Hence, we treat E_{B-V} as a potential systematic and test its effect on the density field.

[13] Note that most of the systematics studied here (with the exception of E_{B-V} and stellar density) are not available at higher resolution than this pixelisation scheme in any case, as they are measured per CCD.

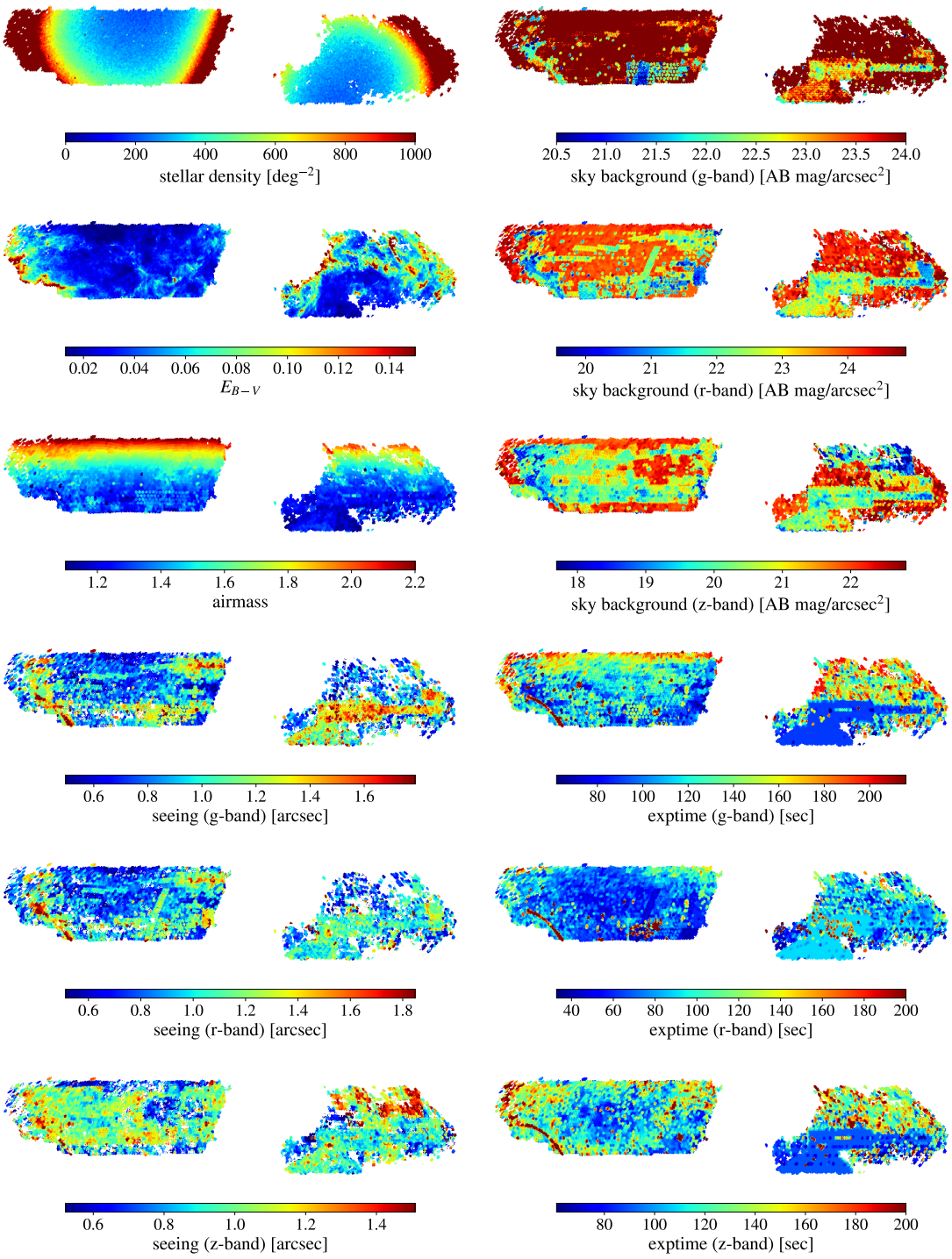

Figure 3.11: Maps of spatially-varying potential systematics in equatorial coordinates with Mollweide projection and astronomy convention (east towards left).

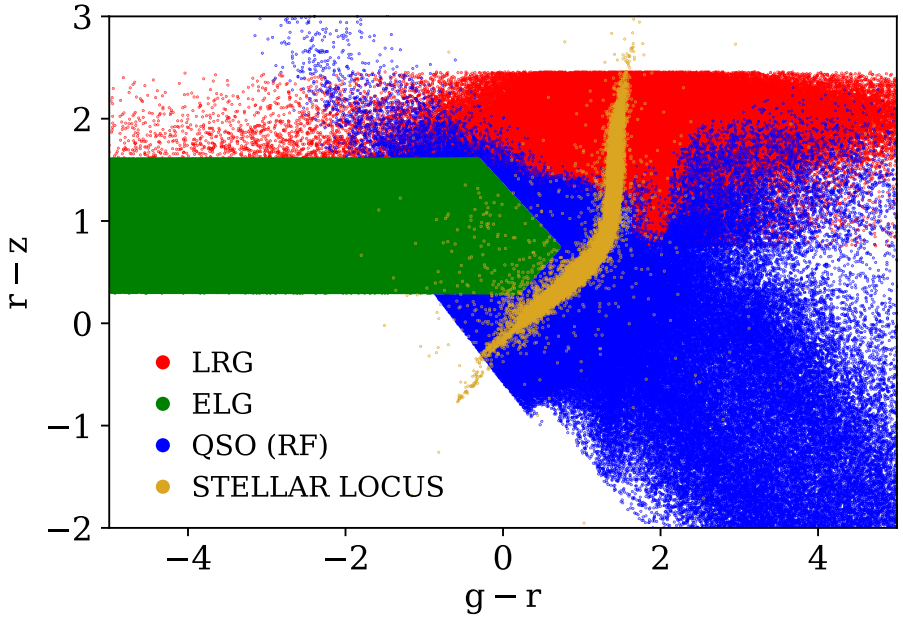

Figure 3.12: Color-color plot of LRG, ELG, QSO target selection, with the shape of the stellar locus selected from DECaLS as PSF-type objects with $17 < r < 18$.

3. Seeing

   Astronomical seeing is the blurring of an image due to turbulence in the Earth's atmosphere. The distortions fill out a point spread function (PSF) whose full width at half maximum quantifies the quality of the seeing conditions. In DECaLS, seeing is determined by fitting the median PSF of stars on the CCD to a 2D Gaussian. Since seeing varies between nights and even exposures, a mean value is reported, calculated by averaging the inverse of the effective number of pixels in the PSF (such that images with better seeing dominate the mean, as they contain more information). We use this mean PSF size to determine the impact of seeing conditions on the density field, since bad seeing causes larger magnitude errors as well as more cross-contamination with stars due to poor morphological fits.

4. Airmass

   Airmass is the optical path length of light through the Earth's atmosphere. When photons from a celestial source travel to a terrestrial observer, they are absorbed and scattered by the atmosphere. Light that must traverse more atmosphere will be attenuated more, so sources appear dimmer at the horizon than at the zenith. For zenith angles $\lessapprox 60°$, we can approximate the atmosphere as plane-parallel, and also assume its density is more or less constant. In this limit, the airmass is simply the secant of

the angle from the zenith to the source location on the sky. We treat the mean airmass as a potential systematic, as it contributes to magnitude errors (for instance, airmass induces atmospheric differential refraction as a function of color, which can affect the photometry) and is entangled with the extinction and seeing corrections.

5. Sky brightness

   Variations in the background brightness of the sky (due to various sources such as airglow, scattered starlight, Moon phase, light pollution) can affect the measured flux errors and therefore the density of targets by scattering objects in or out of color cuts. Sky brightness also has a strong dependence on airmass, which increases the brightness of airglow. We include the mean sky background in each band measured on the individual CCDs as a potential systematic.

6. Exposure time

   DECam can attain the depths required for DESI targeting in total exposure times of 166, 134, and 200 sec for g, r, z bands, given median observing conditions. As part of the imaging strategy, dynamic exposure times are increased to compensate for poor observing conditions in order to obtain a more uniform sample. We look at variations with mean exposure time in each band, which affects depth and is correlated with other potential systematics, to see how it modulates the observed density.

Target densities vs. potential systematics

We can determine the post-masking target density per pixel using the random catalogs. Since the randoms are uniformly distributed, counting the number of post-masking randoms in a pixel is equivalent to measuring its effective area, up to a proportionality factor:

$$\delta_i = n_i^{\rm gal}/\bar{n}^{\rm gal} - 1 = N_i^{\rm gal}/N_i^{\rm ran} \times N_{\rm masked}^{\rm ran}/N_{\rm masked}^{\rm gal} - 1 \tag{3.21}$$

For each potential systematic, we bin the pixels by systematic value and then plot the average density versus the average systematic value of the bins. The results are shown in Figure 3.13, with LRGs, ELGs, and QSOs plotted together in each subplot and cumulative sky fraction displayed in the upper panels. The errors bars represent the Poisson noise in each bin; using standard error of the mean gives minuscule error bars, as the variance within each bin is very small, regardless of the exact bin size or pixel resolution used. In general, LRGs show very little dependence on survey properties, while ELGs and QSOs appear more impacted, with QSOs often displaying a nonlinear dependence likely due to the more complex selection function. We find that the NGC and SGC density trends are similar and thus do not need to be plotted separately, with the exception of E_{B-V} for ELGs and stellar density for QSOs. For these two special cases, we include the NGC-only (dashed) and SGC-only (dotted) trend lines in Figure 3.13.

The most significant systematic effects indicated are from stellar density and extinction. ELG density decreases significantly with increasing stellar density and extinction, with 10% level effects in some areas, while QSO density presents the opposite trend. The observed correlation between stellar density and QSO density, and anti-correlation between stellar density and ELG density, is also present in the angular cross-correlation results (Section 3.6). One possible explanation for the extinction dependence is the issue of infrared emission from background galaxies contaminating the SFD dust maps used to correct DECaLS magnitudes. This has been shown to lead to underestimation of the reddening in low extinction ($E_{B-V} < 0.15$) regions (Yahata et al. 2007, Kashiwagi et al. 2013, Kashiwagi et al. 2015), attributed to the fact that the extragalactic contamination dominates the dust signal in such regions. Looking at the shape of the targets selection functions in colorspace (Figure 3.12), underestimation of reddening could preferentially scatter objects out of the ELG selection or into the QSO selection. While the resultant underestimation of extinction in these regions is small, it may be highly correlated with the targets.

Some minor dependence on seeing and sky background are also observable, particularly for QSOs, as it is more difficult to distinguish between QSOs and stars in regions with bad seeing and bright sky backgrounds. The relationships between target densities and mean exposure times is more complex. Due to the use of dynamic exposure times, there is entanglement with other systematics; for example, exposures are scaled longer for higher airmass or regions of higher galactic extinction. CCDs with exposure times less than 30 sec are automatically removed in the image reduction pipeline, and the "jumps" or discontinuities in sky fraction at various other times are artifacts of the observing strategy. The fact that we are averaging the exposure times over multiple overlapping CCDs slightly muddies the interpretation as well. Nevertheless, it is clear that the attempt to obtain more uniform depths through dynamic exposure times is not perfectly successful for QSOs.

Based on these findings, we create photometric weights to reduce the variance in target densities due to systematics. Working directly with the HEALPix pixels defined in the previous section, we use principal component analysis (PCA) to transform the list of potential systematics into a minimum set of linearly uncorrelated variables. PCA using a full SVD solver reduces the dimensionality from 12 scaled features to 11 components. The first component explains ∼22% of the variance and last component explains ∼3% of the variance, with ∼50% of the variance explained by the first 3 components and ∼75% of the variance explained by the first 6 components

Unsurprisingly, we find that exposure times contain a great deal of information, as they are correlated with all of the other systematics by design. However, since exposure times are difficult to interpret, we also perform a version of the component analysis with the exposure times removed from consideration, in order to show more clearly how the other features contribute and in what combinations. We find that nearly equal contributions from stellar density and galactic extinction tend to strongly dominate a few components, while more complex mixtures of sky background, seeing, and airmass features dominate the others, as physical intuition might lead us to expect.

We discretize the feature-space to reduce the impact of noisy pixels and outliers, then

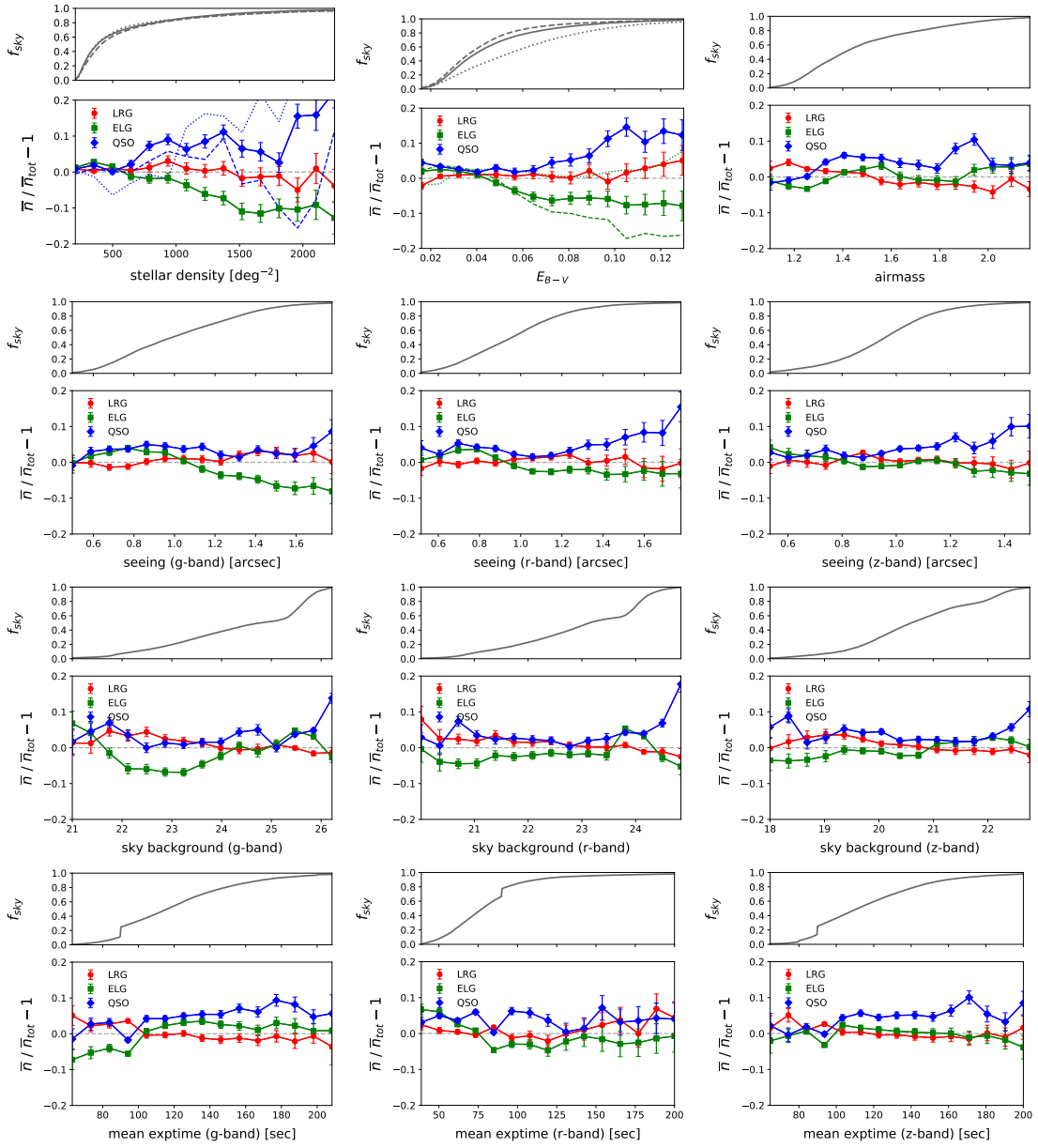

Figure 3.13: Systematic dependences before applying photometric weights: Mean density fluctuations for LRGs (red circles), ELGs (green squares), and QSOs (blue diamonds), as a function of (from top-left to bottom-right) mean stellar density, color excess E_{B-V}, airmass, seeing, sky background, and exposure time in each band, with Poisson errors. The top panel in each figure is the cumulative sky fraction for each systematic. We generally find that splitting between NGC and SGC has negligible effects on the 1D density trends, with the exception of E_{B-V} for ELGs and stellar density for QSOs; for these two cases, we have added the NGC-only (dashed) and SGC-only (dotted) trend lines.

apply multilinear regression. The resulting model of density as a function of potential systematics is used to generate weights.[14] We apply our photometric weights to the randoms, modulating the effective area (and therefore target density) of the survey based on the local values of systematics. Weights are normalized in the sense that the proportionality factor in Equation 3.21 changes from the number of randoms in the masked footprint to the sum of their weights. Plots of the density vs. systematics after applying weights is shown in Figure 3.14, with the linear parts of the trends improved. Figure 3.16 demonstrates the effect of applying these weights on the angular correlation functions. All clustering results presented in Section 3.7 and Section 3.8 are computed using the weighted values.

Correlation with stars and stellar contamination fraction

We also measure the angular cross-correlation between the targets (after masking but before weighting) and our stellar catalog, with the results shown in Figure 3.15. Consistent with the density trends observed in Figure 3.13, LRGs appear uncorrelated with stars, while ELGs demonstrate a small constant anticorrelation, and QSOs show a more significant constant correlation.

Using the angular cross-correlation, we can estimate the fraction of stellar contamination in the QSO sample. Let us assume that the observed number of QSOs at any given location includes some non-trivial number of contaminants, as seems strongly indicated. Let $N_{\rm star}$ be the total number of stars that modulate the QSO density in some way:

$$N_{\rm obs} = N_{\rm true} + \bar{\epsilon} N_{\rm star} \tag{3.22}$$

where $\bar{\epsilon}$ is the average number of impacted sources associated with each star. For stars which are simply misclassified as QSOs, $\epsilon = 1$. For spurious QSO detections in the immediate vicinity of stars, $\epsilon > 0$. For occulted QSOs in the immediate vicinity of stars, $\epsilon < 0$. Note that for the latter two effects (spurious or occulted sources near stars) we are considering fainter stars that were not masked out in Section 3.4. Thus, any cross-correlations between these sources and their own associated star are negligible beyond very small scales, so the cross-correlation between contaminants and stars is dominated by the autocorrelation of stars times the multiplicative factor ϵ.

The fraction of the total sample which is made up of these problematic stars is approximately given by

$$f_{\rm star} = \frac{\langle N_{\rm star} \rangle}{\langle N_{\rm obs} \rangle} \tag{3.23}$$

where the brackets signify a spatial average. Similarly, the fraction of true objects is

$$f_{\rm true} = \frac{\langle N_{\rm true} \rangle}{\langle N_{\rm obs} \rangle} \tag{3.24}$$

[14] For randoms where any of the potential systematics were undefined due to lack of exposures in one or more bands, the weights were manually set to one. The randoms used in our clustering analysis have had the completeness mask of Section 3.4 applied, and thus are not affected by this.

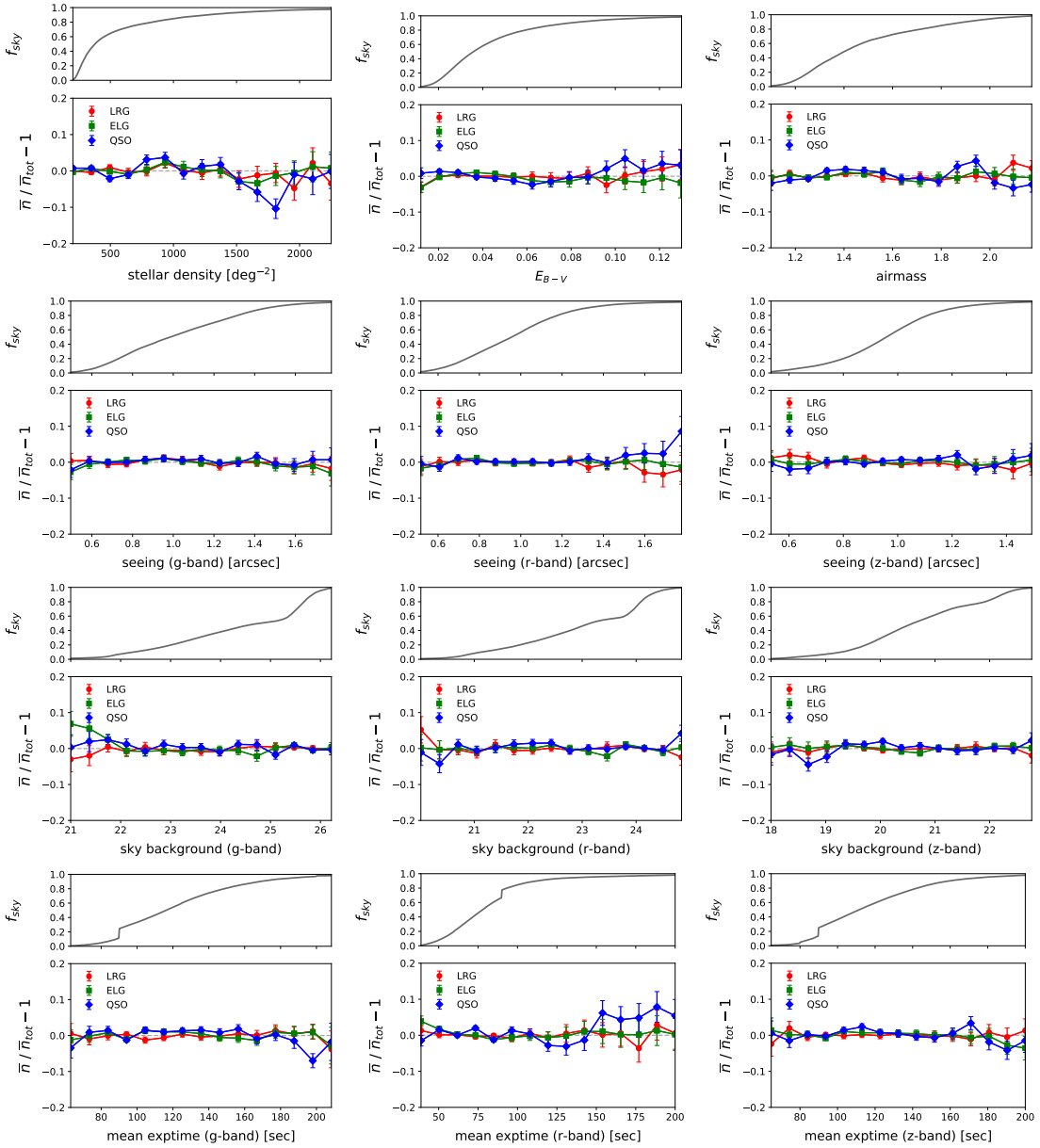

Figure 3.14: Systematic dependences after applying photometric weights: Mean density fluctuations for LRGs (red circles), ELGs (green squares), and QSOs (blue diamonds), as a function of (from top-left to bottom-right) mean stellar density, color excess E_{B-V}, airmass, seeing, sky background, and exposure time in each band, with Poisson errors. The top panel in each figure is the cumulative sky fraction for each systematic.

We can rewrite this in terms of the density contrasts $\delta = N/\langle N\rangle - 1$, by exploiting the fact that $\langle N_{\rm obs}\rangle = \langle N_{\rm star}\rangle/f_{\rm star} = \langle N_{\rm true}\rangle/f_{\rm true}$, such that the observed density of objects is

$$\begin{aligned}\delta_{\rm obs} &= \frac{N_{\rm obs}}{\langle N_{\rm obs}\rangle} - 1 = \frac{N_{\rm true}}{\langle N_{\rm obs}\rangle} + \bar{\epsilon}\frac{N_{\rm star}}{\langle N_{\rm obs}\rangle} - 1 \\ &= f_{\rm true}\frac{N_{\rm true}}{\langle N_{\rm true}\rangle} + \bar{\epsilon} f_{\rm star}\frac{N_{\rm star}}{\langle N_{\rm star}\rangle} - 1 \\ &= f_{\rm true}(\delta_{\rm true}+1) + \bar{\epsilon} f_{\rm star}(\delta_{\rm star}+1) - 1 \\ &= f_{\rm true}\delta_{\rm true} + \bar{\epsilon} f_{\rm star}\delta_{\rm star} \end{aligned} \tag{3.25}$$

Thus we can extract the contamination fraction by dividing the QSO-star cross-correlation by the stellar autocorrelation function, $w_{\rm cross}(\theta)/w_{\rm star}(\theta) = \langle\delta_{\rm obs},\delta_{\rm star}\rangle/\langle\delta_{\rm star},\delta_{\rm star}\rangle = \bar{\epsilon} f_{\rm star} \equiv f_{\rm contam}$, since the cross-correlation between true QSOs and stars vanishes.[15]

As the stellar density varies significantly across the sky (see Figure 3.11), with a strong gradient towards the galactic plane, we first divide the sky into three bins: $|b| < 40$, $40 < |b| < 60$, and $|b| > 60$. For each galactic latitude bin, we calculate $w_{\rm cross}(\theta)$ and $w_{\rm star}(\theta)$, averaged across all angular scales (as both correlation functions are flat, within error bars, for all bins), and then bootstrap upon these averaged values to obtain error bars. The resulting stellar contamination fractions are $f_{\rm contam} = 7\% \pm 4.9\%$ for $|b| < 40$, $f_{\rm contam} = 4.9\% \pm 2.7\%$ for $40 < |b| < 60$, and $f_{\rm contam} = 4.1\% \pm 2.3\%$ for $|b| > 60$.

3.7 Angular Clustering Measurements

Mean densities

The average target densities for DR7 are given in Table 3.5. We present the raw densities as well as the densities after observational effects have been accounted for using the masks and weights described in this chapter. Here, densities are calculated by taking the ratio of the total number of objects and the total area, with the latter being estimated using counts of uniform randoms with the masks and weights applied to them. For an independent calculation of raw target densities, column 2 of the counts-in-cells tables in Section 3.7 gives the average number of objects $\bar{N}$ within a square cell of some width, and thus can be divided by the corresponding cell area to give the mean (raw) density smoothed over that scale.

Angular correlation functions with r_0, γ fits

The measured angular correlation functions for the three target classes are shown in Figure 3.16. We present the correlation functions at various stages of analysis, to demonstrate

[15] We have assumed an ideal stellar template; in reality, there may be a small fraction of true QSOs in the star sample, or a fraction of galaxies in both the QSO and star samples which correlate with each other, but these fractions should be much smaller than the fraction of stellar contaminants in the QSO sample, and hence we can ignore them to first order.

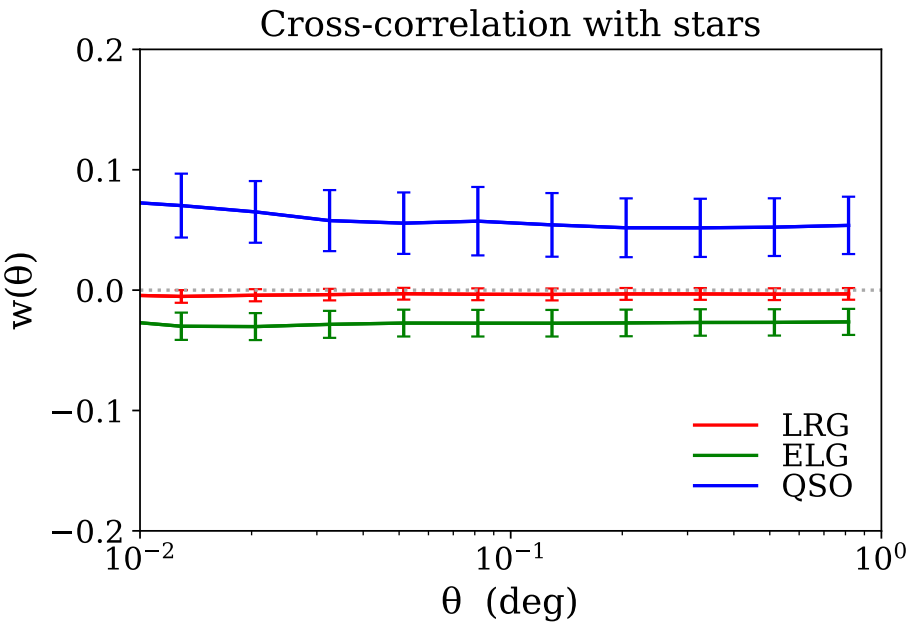

Figure 3.15: Angular cross-correlation between DESI targets and stars, with errors from bootstrapping on the area.

	Avg. density (deg^{-2})			
Target	Raw	Masked	Masked & Weighted	FDR
LRG	525.0	501.4	498.9	480
ELG	2497.5	2351.8	2352.7	2400
QSO	336.1	261.2	256.2	260

Table 3.5: Average densities for each target type, calculated over the available footprint. The first column is the uncorrected densities, the second column has only had the masks of Section 3.4 applied, and the third column has additionally had the photometric weights of Section 3.6 applied. The projected target densities from the FDR are also included for reference.

the effects of applying masks, weights, and so on. The final, "cleanest" version is fit to theory, as described below.

According to the current paradigm of galaxy formation, galaxies form within collapsed overdensities of dark matter called "halos" (for a recent review on the galaxy-halo connection, see Wechsler & Tinker 2018). Under this model, the correlation function of galaxies is the sum of two contributions: a 2-halo term corresponding to pairs of galaxies within different halos, and a 1-halo term corresponding to pairs of galaxies within the same halo. On small scales, where the 1-halo term dominates, the correlation function depends on the complex baryonic physics of galaxy formation and evolution, while on larger scales, where the 2-halo term dominates, the correlation function is characterized by the halo bias describing how dark matter halos trace the dark matter distribution. When combined, these two terms result in an approximate power law, with a feature corresponding to the 1-halo to 2-halo transition occurring around 1-2 h^{-1} Mpc, the typical virial radius of a halo. Motivated by this, we assume the real-space correlation function is a simple power law of the form $\xi(r) = (r/r_0)^{-\gamma}$. Using tabulated dN/dz for each target and applying the Limber approximation (Equation 3.5), we obtain constraints on r_0 and γ, listed in Table 3.6.

For LRGs, we determine $r_0 = 7.78 \pm 0.26$ h^{-1}Mpc and $\gamma = 1.98 \pm 0.02$, which agrees well with previous results for similar samples from the literature; for example, Sawangwit et al. (2011) (Table 2, row 4) finds $r_0 = 7.56 \pm 0.03$ h^{-1}Mpc and $\gamma = 1.96 \pm 0.01$ for a photometric subsample of LRGs from SDSS imaging with $\bar{z} = 0.68$ and a similar redshift distribution, over approximately the same range of angular scales. While the LRG correlation function shows some additional structure that is not fit perfectly by a power law model, no strong features are observed on these scales, which is generally consistent with earlier findings from eBOSS and SDSS LRG studies (see e.g. Zehavi et al. 2005).

We find that the ELG correlation function has a broken form. When fitting from $\theta = 0.001°$ to $\theta = 0.01°$, the correlation function is well fit by $r_0 = 6.70 \pm 0.10$ h^{-1}Mpc and $\gamma = 1.85 \pm 0.01$. However, for scales $\theta > 0.05°$, the slope becomes shallower, and the correlation function is better fit by $r_0 = 5.45 \pm 0.10$ h^{-1}Mpc and $\gamma = 1.54 \pm 0.01$. At the mean effective redshift of the DESI ELG sample, $z \sim 0.85$, the co-moving scale of this break is approximately 1 h^{-1}Mpc, consistent with a 1-halo to 2-halo transition. The second slope matches with the findings of Favole et al. (2016), who modeled a sample of ELGs selected from the Canada-France Hawaii Telescope Legacy Survey (CFHTLS), cross-matched with BOSS ELG and VIPERS redshifts, at mean redshift $\bar{z} \approx 0.8$, to obtain $s_0 = 5.3 \pm 0.2$ h^{-1}Mpc and $\gamma = 1.6 \pm 0.1$. Furthermore, when calculating the angular correlation function over the full CFHTLS footprint, they also observed a change of slope occurring at $\theta \approx 0.01° - 0.05°$, and found that this clustering was consistent with an HOD model having halo masses on the order of $10^{12} M_\odot$ and satellite fraction $f_{\rm sat} \sim 22\%$. Similarly, Jouvel et al. (2015) found $s_0 = 4.2 \pm 0.26$ h^{-1}Mpc and $\gamma = 1.48 \pm 0.04$ for a bright sample of eBOSS ELGs selected from DES photometry at $\bar{z} = 0.86$. The real-space clustering amplitudes and slopes for both LRGs and ELGs are also consistent with the results from Mostek et al. (2013) for red and blue galaxy populations in DEEP2.

The QSO correlation function still contains a significantly enhanced clustering signal due

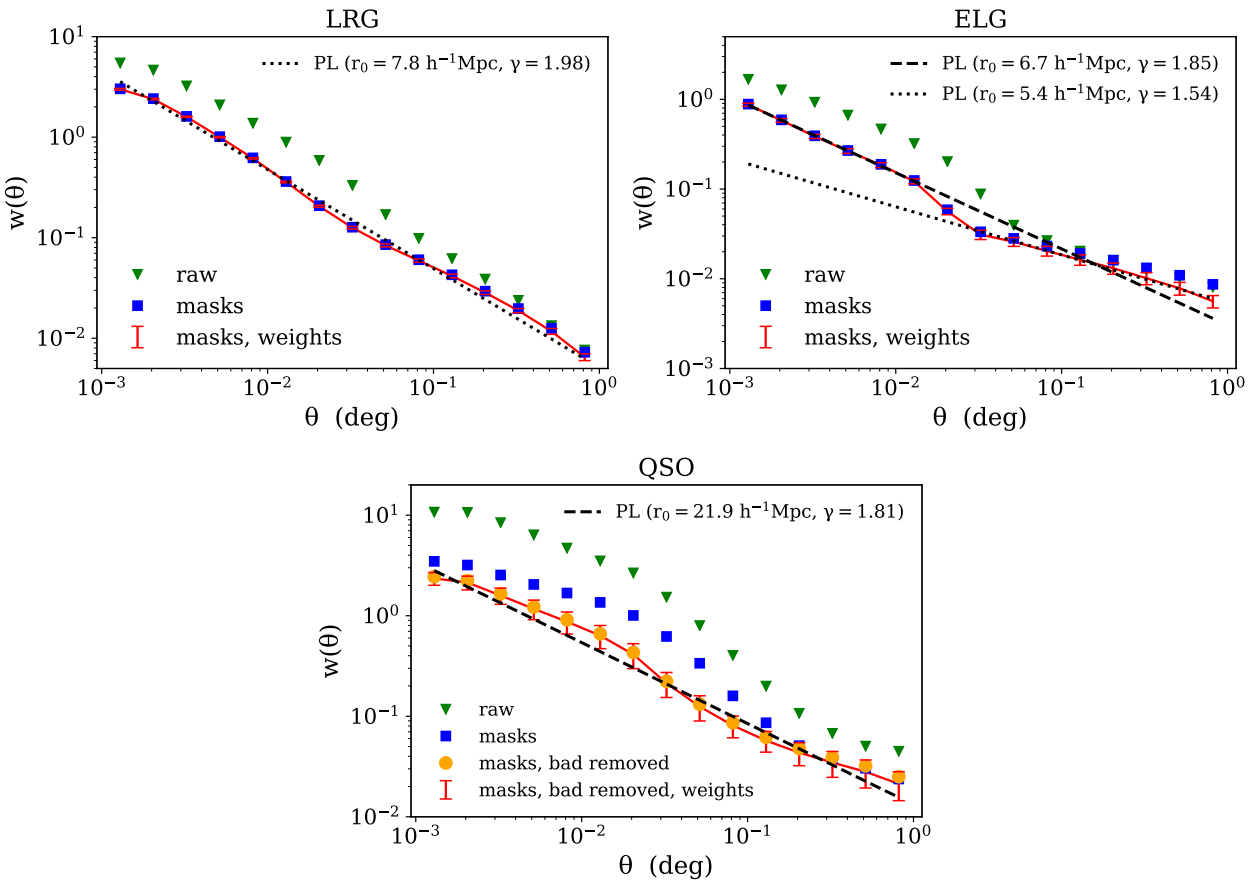

Figure 3.16: Two-point angular correlation functions for LRGs, ELGs, and QSOs at several levels of systematics analysis: without any corrections (green triangles), after applying masks (blue squares), and after applying both masks and photometric weights (red error bars). For QSOs, we perform the additional intermediate step of removing the anomalous regions discussed in Section 3.5 (orange circles). The red lines are fit to a power-law model for the three-dimensional clustering $\xi(r) = (r/r_0)^{-\gamma}$. The values of these fits are listed in more detail in Table 3.6.

to systematics and contamination, with $r_0 = 21.9 \pm 0.10$ h^{-1}Mpc and $\gamma = 1.81 \pm 0.02$. By comparison, some fiducial values of QSO clustering amplitude at $z \sim 2$ from the literature are: $r_0 = 5.84 \pm 0.33$ and $\gamma = 1.65 \pm 0.05$ (Croom et al., 2005), or $r_0 = 4.56 \pm 0.48$ at fixed $\gamma = 1.5$ (Myers et al., 2009).

Target	$\theta_{\rm min}, \theta_{\rm max}$	r_0 (h^{-1}Mpc)	γ	$\log_{10} A_w$
LRG	0.001°, 1°	7.78 ± 0.26	1.98 ± 0.02	-4.01 ± 0.05
ELG	0.001°, 1°	5.98 ± 0.30	1.90 ± 0.03	-4.25 ± 0.06
	0.001°, 0.01°	6.70 ± 0.10	1.85 ± 0.01	-4.01 ± 0.02
	0.05°, 1°	5.45 ± 0.10	1.54 ± 0.01	-3.22 ± 0.02
QSO	0.001°, 1°	21.9 ± 1.01	1.81 ± 0.03	-3.31 ± 0.07

Table 3.6: Results from fitting the correlation functions to a power-law $\xi(r) = (r/r_0)^{-\gamma}$, where we have used the expected redshift distributions of DESI targets in the Limber approximation to convert between angular clustering and real-space clustering. We list the angular scales fitted over, the expected $\bar{z}$ of each sample, and the best fit parameter values and errors.

Angular power spectra with $b_0, b(k)$ fits

We measure the angular power spectra of the three main DESI target samples using the methods described in Section 3.2. We reiterate that the results presented here have already had the masks and weights of the previous sections applied. Similar to their effect on the angular correlation functions, the impact of the photometric weights derived in Section 3.6 on the angular power spectra is to reduce power on large scales. For LRGs, not using the weights would increase the amplitude by $\sim 15\%$ at $\ell \sim 20$ down to $\sim 1\%$ at $\ell \sim 75$. For ELGs, it would increase by $\sim 43\%$ at $\ell \sim 20$ down to $\sim 1\%$ at $\ell \sim 150$. For QSOs, it would increase by $\sim 12\%$ at $\ell \sim 20$ down to $< 1\%$ at $\ell \sim 75$.

From the angular power spectra, we fit the linear bias. First, we restrict to very large scales where the bias is approximately constant, then relax this restriction as we probe the scale dependence of the bias using the "P model" (Smith et al. 2007, Hamann et al. 2008, Cresswell & Percival 2009), which treats the nonlinear correction to the bias as an extra non-Poissonian shot noise term arising from the assumption that galaxies populate halos (Seljak 2001, Schulz & White 2006, Guzik et al. 2007):

$$P_g \to P_g + P \implies \tag{3.26}$$
$$b(z)^2 = \frac{b_0^2}{D(z)^2} \to b(k,z)^2 = \frac{b_0^2}{D(z)^2}\left(1 + \frac{P}{b_0^2 P_m(k,z)}\right)$$

In terms of the angular power spectra, which involve convolution with the radial distributions

(see Equation 3.13), we have

$$C_\ell \to C_\ell + C$$
$$C = P \int d\chi \; f(\chi)^2 \frac{1}{\chi^2} \frac{1}{D(z)^2} \tag{3.27}$$

Using `CLASS`, we compare C_ℓ derived from linear and HALOFIT (Smith et al., 2003) predictions of the matter power spectrum to estimate $\ell_{\rm max}$ where they begin to diverge, taking the common assumption that the nonlinear correction to the matter power spectrum becomes significant at approximately the same scale as nonlinear effects in the galaxy bias (see e.g. Fry & Gaztanaga 1993, Modi et al. 2017, Desjacques et al. 2018, Wilson & White 2019). We find that $\ell_{\rm max} \approx 200$ is appropriate for LRGs and ELGs, and slightly conservative for QSOs, which are at higher mean redshift.

LRGs

With $\ell_{\rm max} = 200$, we use the linear theory matter power spectrum and fit the scale-independent bias in two ways: first, by fixing the Poisson shot noise term $\tilde{W} = 1/\bar{n}$ and only fitting b_0, and second, by simultaneously fitting b_0 and $\tilde{W}$. Then, we extend out to $\ell_{\rm max} = 500$ and add the additional P parameter to our model. We fit P in several ways: both using the previously found values of b_0 and $\tilde{W}$ from the $\ell_{\rm max} = 200$ case, and also doing a simultaneous fit to b_0 and P, with $\tilde{W}$ absorbed into P. The results of all fits are shown in Table 3.7 for LRGs, with all models giving similar results and showing agreement with expectation. In Figure 3.17, we plot the binned data, the best fit model, and the FDR expectation curve.

ELGs

For ELGs, we find that attempting to co-fit the bias and shot noise terms simultaneously returns unphysical negative values for the latter, due to enhanced power at scales $\ell < 150$ even after applying masks and weights (fortunately, these scales should not directly impact BAO and RSD measurements). However, when fixing the shot noise as $\tilde{W} = 1/\bar{n}$, we obtain $b_0 = 1.273 \pm 0.005$, which agrees well with e.g. Comparat et al. (2013), Delubac et al. (2017).

We also calculate the corresponding C_ℓ for each of the two power-law model $w(\theta)$ fits in Figure 3.16 and plot these as well in Figure 3.18, with shot noise contributions fitted as additional free parameters. The results show consistency between our $w(\theta)$ and C_ℓ results, both of which give clustering parameters falling within the range of fiducial values found in previous studies.

The DESI FDR assumes a conservative lower limit of $b_0 = 0.84$, also plotted in Figure 3.18, and we confirm that the ELG clustering bias is higher than this value. This is significant as it has the effect of improving the statistical errors on BAO, while also somewhat degrading the RSD forecasts, since more strongly biased tracers exhibit weaker anisotropy. We note that allowing the shot noise term to float in the FDR curve in order to raise its

LRG, $b_0^{FDR} = 1.7$						
$\ell_{max} = 200$ scale-independent bias			$\ell_{max} = 500$ P model			
b_0	$\bar{n}\tilde{W}$	$\frac{\chi^2}{\text{d.o.f}}$	b_0	$\bar{n}\tilde{W}$	P	$\frac{\chi^2}{\text{d.o.f}}$
1.570 ± 0.014	1 (fixed)	5.0 / 9	-	-	3539 ± 99	12.6 / 25
1.607 ± 0.040	1.61 ± 0.43	3.7 / 8	-	-	965 ± 99	18 / 25
			1.569 ± 0.017	0 (fixed)	7120 ± 198	12.6 / 24

Table 3.7: Fitting the LRG large-scale bias from the angular power spectra. We initially limit to $\ell \leq 200$ and fit the linear bias to a constant; first, by fixing the Poisson shot noise term as $1/\bar{n}$, and second, by fitting the bias and noise simultaneously. Then we extend to $\ell = 500$ and fit an additional parameter P for the scale-dependent bias model; first, by holding the previously found values fixed and fitting only the non-Poisson shot noise term P at larger ℓ, and second, by fitting the linear bias and P simultaneously, with P now absorbing both shot noise terms.

amplitude still results in a very poor fit, as it flattens the curve such that it can only achieve artificial agreement with observation at very large ℓ.

QSOs

For QSOs, the angular power spectrum, like the angular correlation function, is significantly inflated with non-cosmological signals. As such, we do not report fitted values, but merely plot the results in Figure 3.19 alongside FDR expectation to demonstrate the discrepancy. Furthermore, whereas the LRGs and ELGs show no difference when comparing NGC and SGC measurements, QSOs once again show a mismatch between galactic hemispheres; after removing the problematic pixels found in Section 3.5, which caused disproportionately strong small-scale clustering in the NGC, the shapes of the angular power spectra in the NGC and SGC become identical, but the SGC is enhanced on all scales compared to the NGC. This is consistent with our other findings, namely that the SGC has more stellar contamination than the NGC and that the clustering of these stellar contaminants is relatively flat across scales (Section 3.6).

[16]Since uncertainty in the shot noise terms would normally dominate the model errors (see Figure 3.17), the "envelope" with fixed shot noise appears very thin.

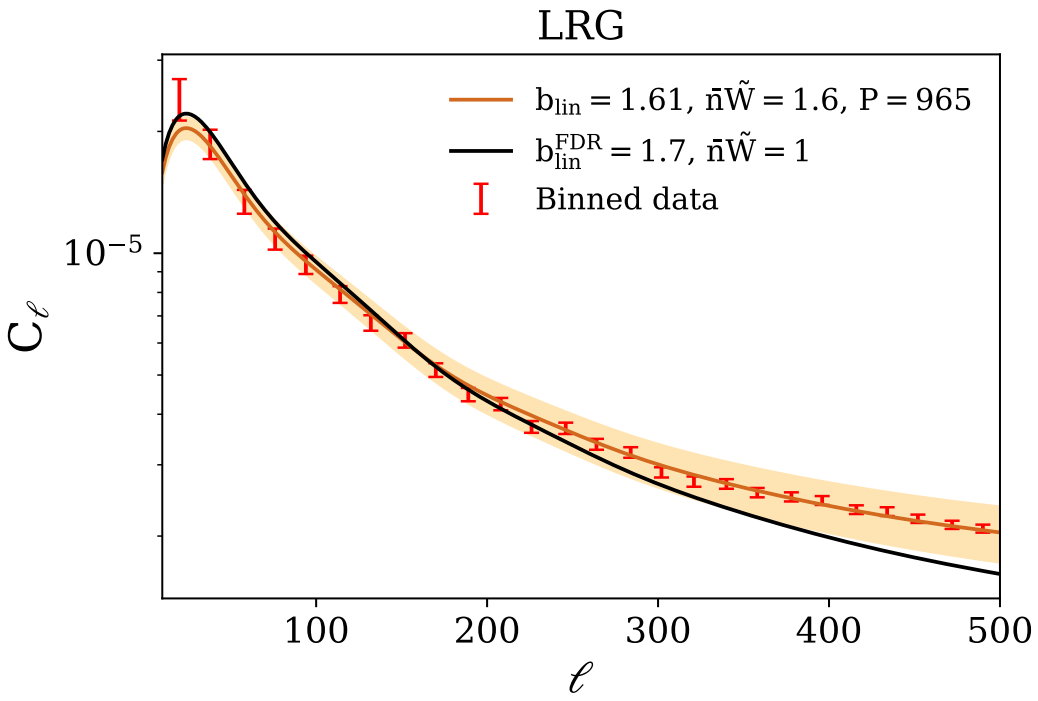

Figure 3.17: Angular power spectrum C_ℓ for LRGs. The red error bars are the binned errors from Equation 3.12. The solid black line is the theoretical curve using the FDR value for the linear bias. The orange envelope is our best fitting P-model result, with the model errors dominated by uncertainty in the shot noise terms.

Counts-in-cells moments

As discussed in Section 3.2, detailed small-scale clustering information is invaluable for accurate modelling and mock calibration. We calculate the counts-in-cells statistics over two large fields, one in each galactic hemisphere, with effective areas $S_{\text{eff},N} = 3300$ deg^2 and $S_{\text{eff},S} = 562.5$ deg^2 (Figure 3.20). We select these fields to be regular in shape and relatively smooth, avoiding areas that are tattered or full of holes. We calculate the probability distribution $P(N)$ for each field, then measure the weighted average and standard error of the

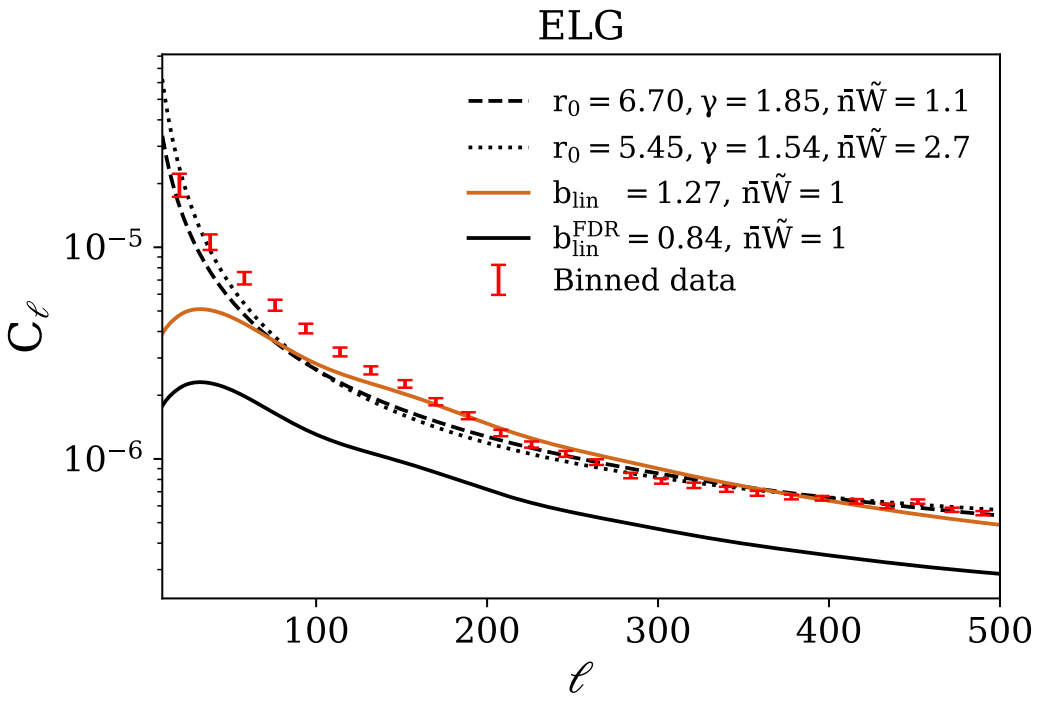

Figure 3.18: Angular power spectrum C_ℓ for ELGs. The red error bars are the binned errors from Equation 3.12. The solid black line is the theoretical curve using the FDR value for the linear bias. The orange envelope[16] is our best fit for the linear bias, using fixed shot noise $\tilde{W} = 1/\bar{n}$. The dashed and dotted lines are the angular power spectra corresponding to the power-law fits to the angular clustering determined in Section 3.7, with the shot noise terms fit as extra free parameters.

factorial moments F_p (Wolk et al., 2013):

$$\bar{F}_p = \frac{\sum_{i=N,S} S_{\mathrm{eff},i} F_{p,i}}{\sum_{i=N,S} S_{\mathrm{eff},i}}$$

$$(\Delta F_p)^2 = \frac{\sum_{i=N,S} S_{\mathrm{eff},i} (F_{p,i} - \bar{F}_p)^2}{\sum_{i=N,S} S_{\mathrm{eff},i}}$$

Following the reasoning of Wolk et al. (2013), we do not perform the complex error propagation from factorial moments to correlation functions, as the error estimate is already a crude approximation limited by the small number of fields.

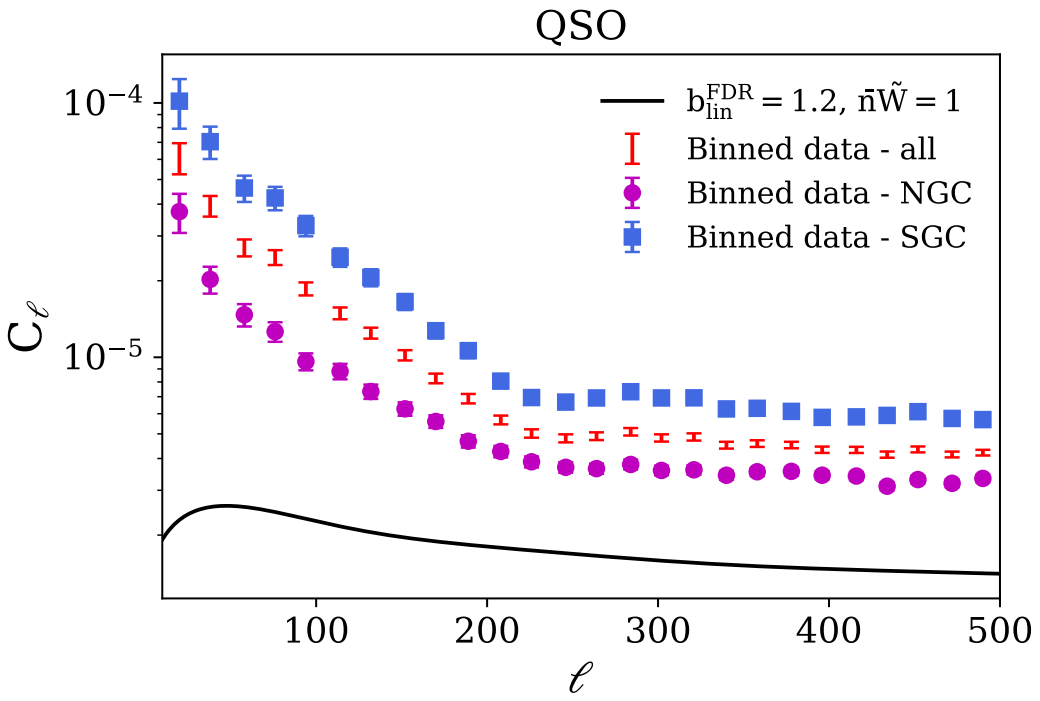

Figure 3.19: Angular power spectrum C_ℓ for QSOs. The red error bars are the binned errors from Equation 3.12. The magenta circles and blue squares are for measurements restricted to the NGC and SGC, respectively. The solid black line is the theoretical curve using the FDR value for the linear bias and fixed shot noise $\tilde{W} = 1/\bar{n}$.

Figure 3.21 shows the probability distributions $P(N)$ evaluated in square cells with different widths from $\theta = 0.01°$ to $\theta = 1°$ for each target class, with a cell width close to the fiber patrol radius ($1.4' \approx 0.023°$) highlighted. The dashed vertical line drawn for this highlighted cell represents the expected number of targets calculated from multiplying the mean target density with the cell area. Note that even for ELGs, the first few angular bins are shot-noise dominated ($\bar{N} < 1$ so most cells contain one or zero targets).

Table 3.8 presents the following quantities for each of the three main target classes:

- mean $\bar{N} \equiv \langle N \rangle$
- variance $\sigma^2 \equiv \langle (N - \bar{N})^2 \rangle$
- skewness $\langle (N - \bar{N})^3 \rangle / \sigma^3$
- kurtosis $\langle (N - \bar{N})^4 \rangle / \sigma^4$
- cell-averaged angular correlation functions $\overline{w}_2$, $\overline{w}_3$, $\overline{w}_4$

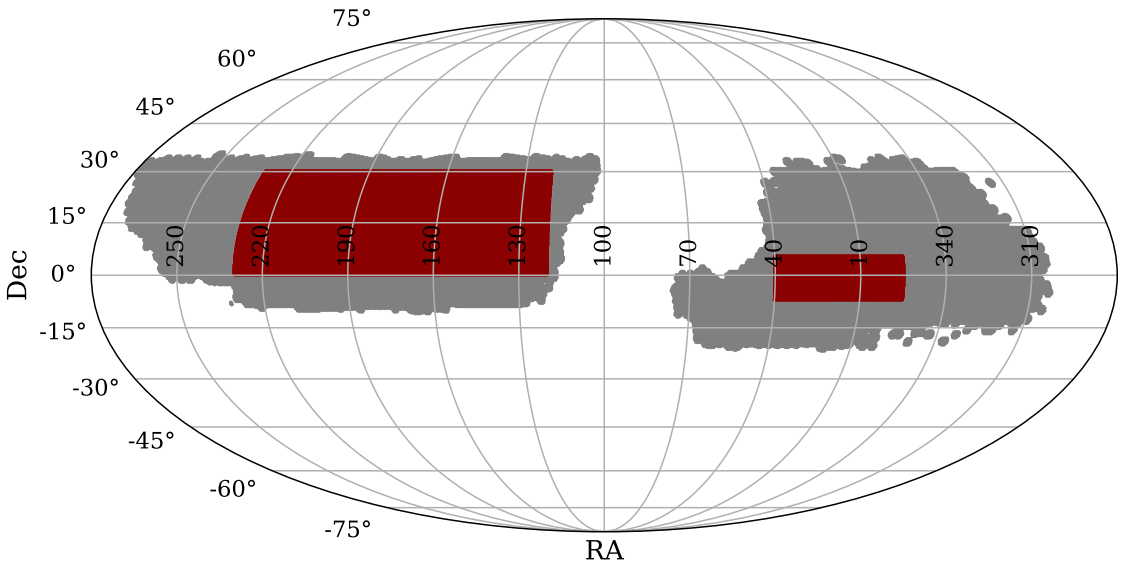

Figure 3.20: Two patches over which we calculate the counts-in-cells distributions and moments. These were chosen by eye as survey regions with no tattered edges and relatively few holes.

From the above quantities, other quantities of interest can be determined, such as the hierarchical moments $S_p = \overline{w}_p/\overline{w}_2^{p-1}$ (Szapudi & Szalay 1993b, Colombi & Szapudi 2001), fitted power law parameters for $\overline{w}_2$ (see e.g. Blake & Wall 2002), etc. More directly, these quantities can be used for the training and testing of mock catalogs.

Clustering as a function of magnitude

Angular clustering is expected to scale with sample depth (Peebles, 1980), so analyzing $w(\theta)$ as a function of magnitude provides another test for the presence of systematics.

We divide the LRG and ELG samples into eight disjoint, equally wide magnitude slices, from the bright limit ($m_z = 18.01$ for LRGs, $m_g = 21$ for ELGs) to the faint limit ($m_z = 20.41$ for LRGs, $m_g = 23.4$ for ELGs) of the target selection. For each bin, we evaluate $w(\theta)$[17]. The results are shown in Figures 3.22 and Figures 3.23, with the upper plots showing $w(\theta)$ for each slice, and the lower plots showing the same functions but with the angular dependence divided out using a representative value of γ determined from fitting the full sample (Table 3.6).

Qualitatively, the results match expectation: the brighter subsamples have larger clustering amplitudes and break from the power law form at larger scales. We also note that, for both LRGs and ELGs, the minimum inflection slides to smaller scales at fainter magnitudes, again consistent with a 1-halo to 2-halo transition; fainter bins are at higher redshift (so the

[17]Note, we do not re-evaluate the photometric weights for each magnitude bin but instead apply the same weights to all bins.

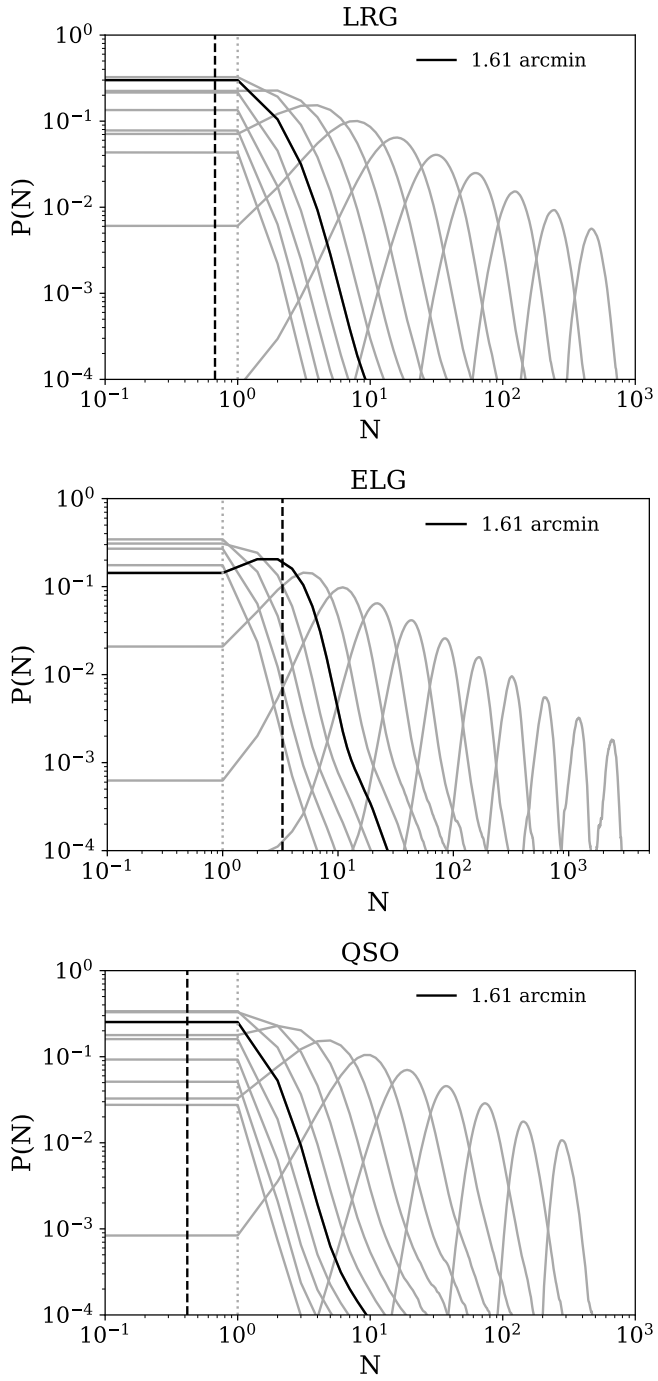

Figure 3.21: $P(N)$ vs. N for 15 logarithmically spaced cell widths from $\theta = 0.01°$ to $\theta = 1°$. The highlighted cell has width $0.268° \approx 1.61$ arcmin, close to the fiber patrol radius of 1.4 arcmin, and the dashed vertical lines correspond to the average target density times the cell area. The dotted vertical line at $N = 1$ marks the limit where shot noise dominates ($\bar{N} < 1$).

	Width	$\bar{N}$	σ^2	$\frac{\langle(N-\bar{N})^3\rangle}{\sigma^3}$	$\frac{\langle(N-\bar{N})^4\rangle}{\sigma^4}$	$\overline{w}_2$	$\overline{w}_3$	$\overline{w}_4$
LRG	0.010°	0.0490 ± 0.0019	0.0550 ± 0.0023	7.50 ± 0.23	260 ± 35	2.410 ± 0.014	250 ± 18	88000 ± 8100
	0.014°	0.0950 ± 0.0036	0.1120 ± 0.0047	7.30 ± 0.35	340 ± 49	1.870 ± 0.022	146.0 ± 9.4	40000 ± 3400
	0.019°	0.1840 ± 0.0069	0.2320 ± 0.0097	7.50 ± 0.45	410 ± 58	1.420 ± 0.025	81.0 ± 4.3	16000 ± 1200
	0.027°	0.350 ± 0.013	0.490 ± 0.020	8.10 ± 0.48	470 ± 55	1.060 ± 0.025	45.0 ± 1.5	6200 ± 300
	0.037°	0.680 ± 0.026	1.050 ± 0.042	9.10 ± 0.45	550 ± 44	0.780 ± 0.024	24.90 ± 0.21	2520 ± 21
	0.052°	1.320 ± 0.050	2.290 ± 0.086	10.00 ± 0.38	620 ± 29	0.560 ± 0.020	13.10 ± 0.15	990 ± 26
	0.072°	2.550 ± 0.096	5.10 ± 0.18	10.10 ± 0.22	617.0 ± 4.3	0.390 ± 0.015	6.30 ± 0.21	360 ± 28
	0.100°	4.90 ± 0.19	11.40 ± 0.36	9.200 ± 0.090	500 ± 22	0.270 ± 0.012	2.80 ± 0.13	110 ± 12
	0.139°	9.50 ± 0.36	26.00 ± 0.75	7.550 ± 0.016	330 ± 20	0.1820 ± 0.0086	1.090 ± 0.066	27.0 ± 3.5
	0.193°	18.40 ± 0.70	61.0 ± 1.6	5.710 ± 0.016	190 ± 12	0.1260 ± 0.0063	0.410 ± 0.028	5.80 ± 0.83
	0.268°	35.0 ± 1.3	145.0 ± 3.2	4.070 ± 0.049	95.0 ± 6.9	0.0880 ± 0.0047	0.150 ± 0.012	1.20 ± 0.19
	0.373°	69.0 ± 2.6	359.0 ± 6.0	2.790 ± 0.093	45.0 ± 4.2	0.0620 ± 0.0036	0.0560 ± 0.0060	0.250 ± 0.044
	0.518°	132.0 ± 5.1	906.0 ± 8.7	1.90 ± 0.13	21.0 ± 2.6	0.0440 ± 0.0029	0.0210 ± 0.0031	0.050 ± 0.011
	0.720°	256.0 ± 9.8	2338.0 ± 5.3	1.30 ± 0.14	11.0 ± 1.6	0.0320 ± 0.0024	0.0080 ± 0.0016	0.0100 ± 0.0028
	1.000°	490 ± 19	6110 ± 99	0.90 ± 0.13	6.0 ± 1.1	0.0230 ± 0.0020	0.00360 ± 0.00083	0.00230 ± 0.00080
ELG	0.010°	0.2350 ± 0.0030	0.290 ± 0.010	5.0 ± 1.2	90 ± 47	1.10 ± 0.27	30 ± 15	2000 ± 1100
	0.014°	0.4530 ± 0.0058	0.630 ± 0.034	5.0 ± 1.5	110 ± 56	0.90 ± 0.21	19.0 ± 9.4	800 ± 520
	0.019°	0.870 ± 0.011	1.40 ± 0.10	6.0 ± 1.8	120 ± 61	0.70 ± 0.16	12.0 ± 5.7	400 ± 230
	0.027°	1.690 ± 0.022	3.20 ± 0.30	7.0 ± 2.0	140 ± 67	0.50 ± 0.12	7.0 ± 3.4	200 ± 100
	0.037°	3.260 ± 0.042	7.30 ± 0.79	7.0 ± 2.2	160 ± 75	0.380 ± 0.088	4.0 ± 1.9	80 ± 49
	0.052°	6.290 ± 0.080	17.0 ± 1.9	7.0 ± 2.2	150 ± 72	0.260 ± 0.055	1.90 ± 0.92	30 ± 18
	0.072°	12.10 ± 0.15	37.0 ± 3.7	6.0 ± 1.8	110 ± 54	0.170 ± 0.030	0.80 ± 0.35	7.0 ± 4.6
	0.100°	23.40 ± 0.30	83.0 ± 5.6	5.0 ± 1.2	70 ± 30	0.110 ± 0.013	0.30 ± 0.11	1.60 ± 0.92
	0.139°	45.30 ± 0.57	192.0 ± 3.3	4.00 ± 0.50	50 ± 11	0.0720 ± 0.0036	0.110 ± 0.021	0.40 ± 0.12
	0.193°	87.0 ± 1.1	460 ± 24	3.40 ± 0.25	34.0 ± 3.4	0.0490 ± 0.0018	0.0480 ± 0.0058	0.110 ± 0.019
	0.268°	169.0 ± 2.1	1200 ± 170	3.0 ± 1.0	30 ± 15	0.0350 ± 0.0049	0.030 ± 0.013	0.050 ± 0.038
	0.373°	326.0 ± 3.9	3100 ± 760	3.0 ± 1.7	30 ± 24	0.0260 ± 0.0065	0.020 ± 0.014	0.030 ± 0.034
	0.518°	628.0 ± 7.3	9000 ± 3000	3.0 ± 2.1	30 ± 28	0.0200 ± 0.0071	0.010 ± 0.013	0.020 ± 0.027
	0.720°	1210 ± 14	30000 ± 11000	3.0 ± 2.3	30 ± 29	0.0170 ± 0.0071	0.010 ± 0.010	0.020 ± 0.020
	1.000°	2340 ± 25	80000 ± 39000	2.0 ± 2.2	20 ± 25	0.0140 ± 0.0068	0.0070 ± 0.0079	0.010 ± 0.012
QSO	0.010°	0.02990 ± 0.00011	0.03700 ± 0.00054	18.0 ± 1.6	1500 ± 290	7.90 ± 0.42	2900 ± 440	1900000 ± 420000
	0.014°	0.05780 ± 0.00022	0.0800 ± 0.0018	25.0 ± 3.2	3000 ± 650	6.70 ± 0.43	2300 ± 410	1500000 ± 360000
	0.019°	0.11160 ± 0.00042	0.1820 ± 0.0064	36.0 ± 5.7	5000 ± 1300	5.70 ± 0.44	1800 ± 370	1100000 ± 300000
	0.027°	0.21550 ± 0.00081	0.440 ± 0.022	49.0 ± 8.9	9000 ± 2300	4.70 ± 0.44	1300 ± 310	800000 ± 230000
	0.037°	0.4160 ± 0.0016	1.080 ± 0.077	60 ± 12	12000 ± 3400	3.80 ± 0.41	900 ± 240	500000 ± 150000
	0.052°	0.8030 ± 0.0030	2.70 ± 0.25	70 ± 15	13000 ± 4200	2.90 ± 0.37	600 ± 170	240000 ± 85000
	0.072°	1.5510 ± 0.0058	6.70 ± 0.76	70 ± 17	12000 ± 4200	2.10 ± 0.30	300 ± 100	100000 ± 38000
	0.100°	2.990 ± 0.011	16.0 ± 2.1	70 ± 16	10000 ± 3300	1.50 ± 0.22	170 ± 54	40000 ± 13000
	0.139°	5.780 ± 0.021	39.0 ± 5.2	60 ± 13	7000 ± 2300	1.00 ± 0.15	80 ± 24	11000 ± 4000
	0.193°	11.160 ± 0.040	90 ± 12	50 ± 10	5000 ± 1500	0.640 ± 0.094	34.0 ± 9.9	3000 ± 1100
	0.268°	21.550 ± 0.077	210 ± 27	42.0 ± 7.5	3400 ± 930	0.400 ± 0.055	13.0 ± 3.6	700 ± 250
	0.373°	41.60 ± 0.15	450 ± 59	32.0 ± 5.4	2000 ± 510	0.240 ± 0.033	4.0 ± 1.2	140 ± 49
	0.518°	80.30 ± 0.29	1000 ± 130	23.0 ± 3.7	1000 ± 260	0.140 ± 0.019	1.40 ± 0.38	25.0 ± 8.5
	0.720°	155.20 ± 0.56	2100 ± 270	16.0 ± 2.5	500 ± 130	0.080 ± 0.011	0.40 ± 0.11	4.0 ± 1.4
	1.000°	300.0 ± 1.1	4500 ± 570	10.0 ± 1.5	230 ± 54	0.0460 ± 0.0061	0.120 ± 0.031	0.60 ± 0.20

Table 3.8: Mean, variance, skewness, kurtosis, and cell-averaged n-point angular correlation functions for each of the three main DESI target classes measured in square cells.

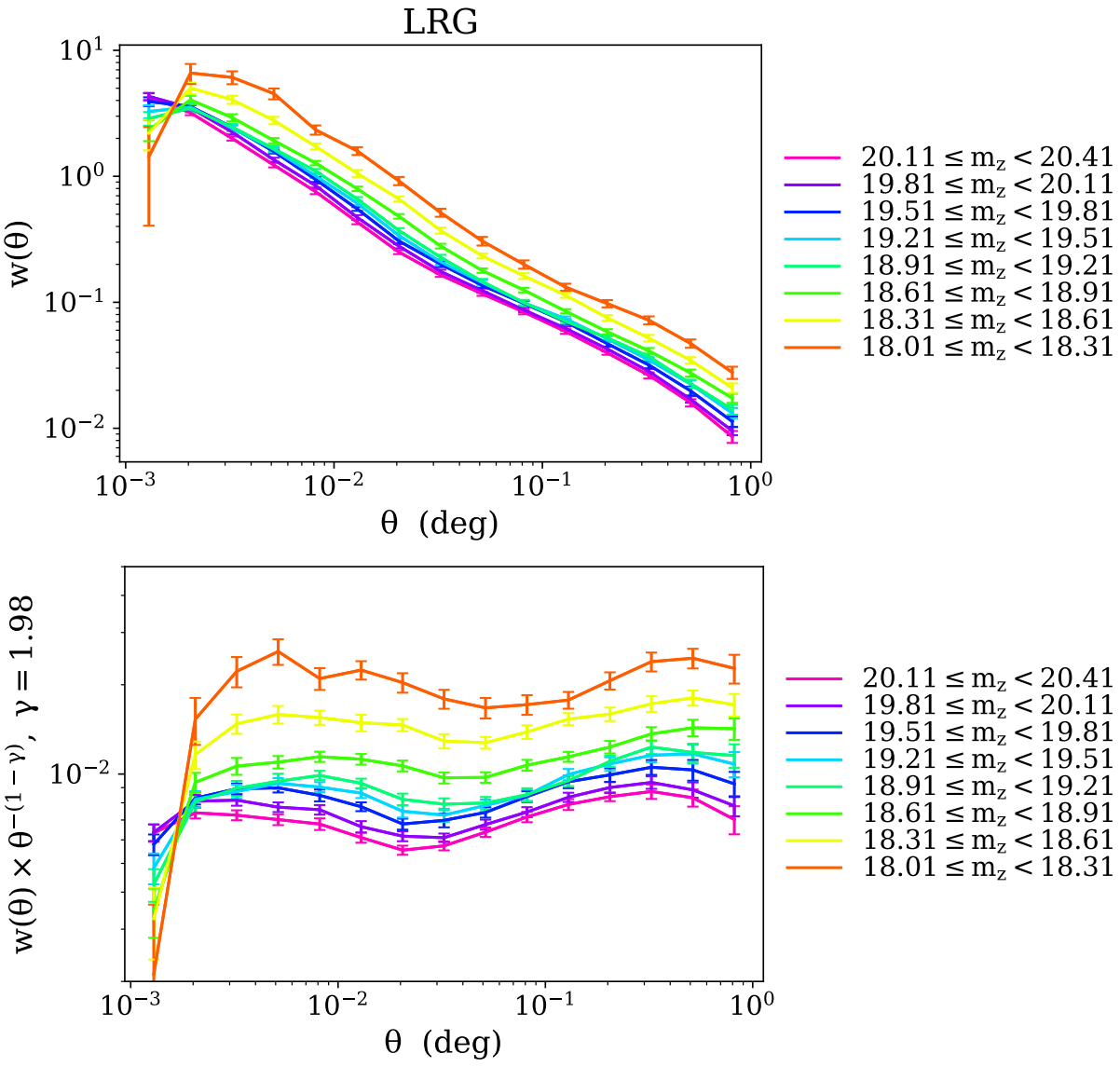

Figure 3.22: Angular correlation functions for LRGs in eight magnitude bins (upper plot), with the angular dependence scaled out for a fixed slope of $\gamma = 1.98$ (lower plot), which is the slope determined from fitting over the full LRG sample in Table 3.6.

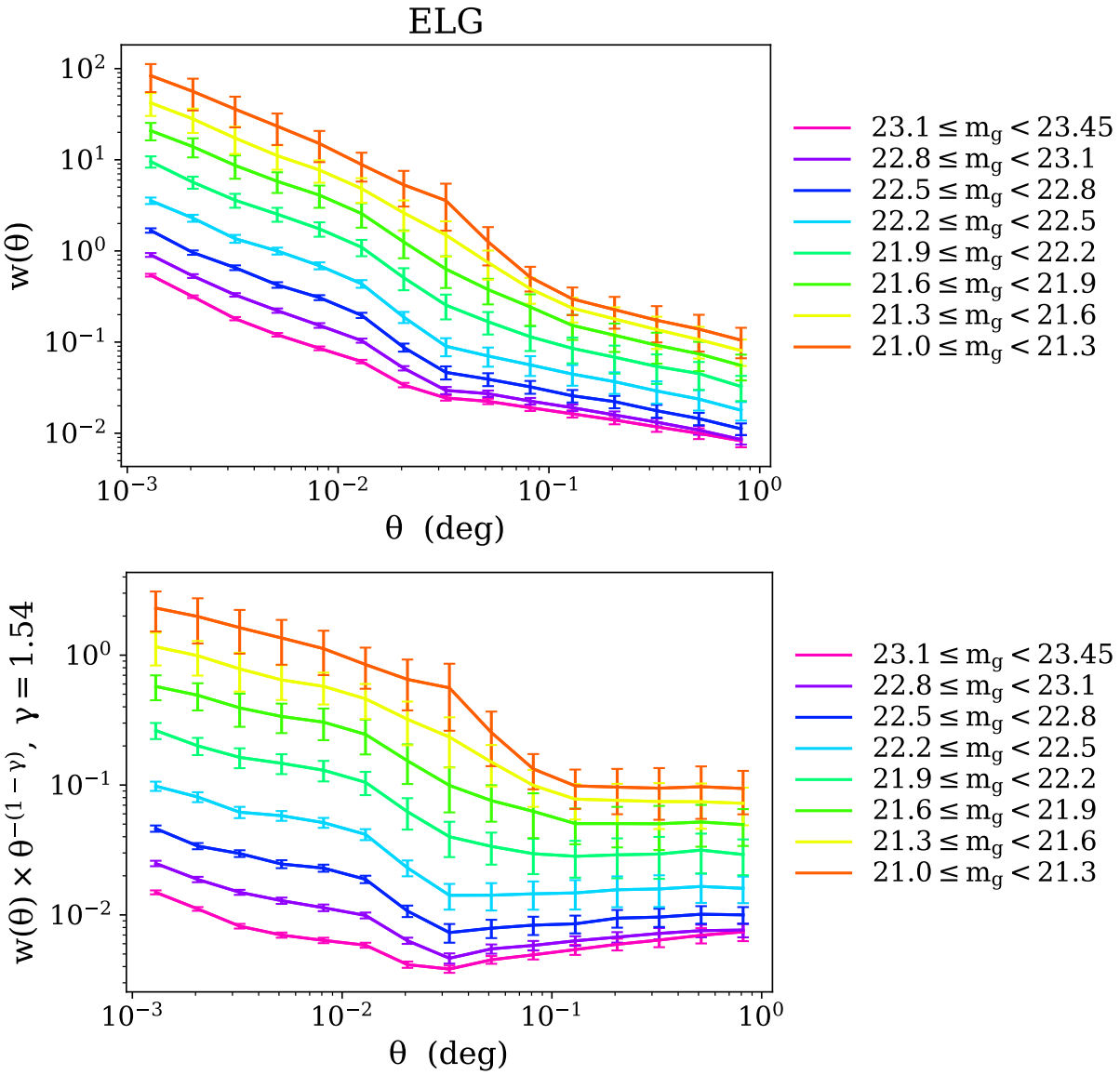

Figure 3.23: Angular correlation functions for ELGs in eight magnitude bins (upper plot), with the angular dependence scaled out for a fixed slope of $\gamma = 1.54$ (lower plot), which is the slope determined from fitting over the full ELG sample in Table 3.6.

characteristic scale of the transition will shift to smaller angles due to the larger angular diameter distance) and/or lower luminosity (thus the 1-halo term will be weaker, as less luminous galaxies reside in less massive halos).

The best fit values for the clustering amplitudes A_w and slopes γ are reported in Tables 3.9 and 3.10. We fit A_w with the fixed representative value of γ, and also fit A_w and γ simultaneously, finding similar results in either case. We also perform the fits over different sets of angular scales, starting with a minimum cutoff of $\theta = 0.005$ for LRGs to avoid scales where the power law model appears to break down, and obtaining fits for $\theta < 0.05^\circ$ and $0.05^\circ < \theta < 1^\circ$ separately as well as for the full range.

3.8 Spectroscopic Cross-Correlations

Clustering as a function of redshift

External catalogs

To probe the clustering as a function of redshift through cross-correlations, as described in Sections 3.2 and 3.2, we make use of several external spectroscopic catalogs. We use the CMASS galaxy sample from DR12 of the Baryon Oscillation Spectroscopic Survey (BOSS; Eisenstein et al. 2011; Dawson et al. 2013a), which selects higher redshift galaxies at $0.4 < z < 0.8$ and has significant angular overlap with the DECaLS footprint. We also use galaxies from the the final data release of the VIMOS Public Extragalactic Redshift Survey[18] (VIPERS; Scodeggio et al. 2018). VIPERS extends over two narrow CFHTLS fields, `W1` and `W4`, with a combined area of approximately 23.5 deg^2, and has nearly 90,000 redshifts out to $z \sim 1$. Finally, we use the main sample of QSOs from eBOSS DR14 (Dawson et al., 2016), which overlaps with the DECaLS footprint in the south galactic cap. Figure 3.24 shows where the footprints of these surveys intersect with DECaLS DR7, and Figure 3.25 demonstrates how their redshift distributions span the expected redshift ranges of the DESI targets.

Projected real-space cross-correlation functions

We present the real-space projected cross-correlation functions (derived in Section 3.2) for LRGs in Figure 3.26, using CMASS galaxies, VIPERS galaxies, and eBOSS QSOs in bins of width $\delta z = 0.1$. Some noisy redshift bins are omitted from the plots. The error bars are from bootstrapping on the area, and therefore are likely overestimated for VIPERS, which has very small fields.

For ELGs, we initially find that the cross-correlations with CMASS galaxies flatten above $\theta \sim 0.01^\circ$ for all redshift bins. However, using the CMASS systematics weights in concert with our own photometric weights eliminates this effect, indicating a correlation between

[18] http://vipers.inaf.it/

LRG						
$\theta_{\rm min}$, $\theta_{\rm max}$	m_z bin	med m_z	# objects	$\log_{10} A_w$ ($\gamma = 1.98$)	$\log_{10} A_w$	γ
0.005°, 0.05°	20.11, 20.41	20.26	868849	$-3.94^{-3.92}_{-3.96}$	$-4.01^{-3.88}_{-4.15}$	$2.00^{2.07}_{1.93}$
	19.81, 20.11	19.96	790503	$-3.90^{-3.88}_{-3.92}$	$-3.97^{-3.82}_{-4.12}$	$2.00^{2.08}_{1.92}$
	19.51, 19.81	19.66	692920	$-3.83^{-3.81}_{-3.86}$	$-3.91^{-3.72}_{-4.10}$	$2.00^{2.09}_{1.91}$
	19.21, 19.51	19.37	596349	$-3.80^{-3.78}_{-3.82}$	$-3.87^{-3.71}_{-4.04}$	$2.00^{2.08}_{1.92}$
	18.91, 19.21	19.06	518696	$-3.77^{-3.75}_{-3.79}$	$-3.84^{-3.68}_{-4.01}$	$2.00^{2.08}_{1.92}$
	18.61, 18.91	18.78	434355	$-3.69^{-3.68}_{-3.70}$	$-3.76^{-3.66}_{-3.86}$	$2.00^{2.04}_{1.96}$
	18.31, 18.61	18.48	257434	$-3.56^{-3.55}_{-3.58}$	$-3.63^{-3.50}_{-3.76}$	$2.00^{2.06}_{1.94}$
	18.01, 18.31	18.19	137380	$-3.41^{-3.39}_{-3.43}$	$-3.48^{-3.25}_{-3.72}$	$2.00^{2.10}_{1.90}$
0.05°, 1°	20.11, 20.41	20.26	868849	$-3.85^{-3.83}_{-3.87}$	$-3.56^{-3.50}_{-3.61}$	$1.87^{1.91}_{1.83}$
	19.81, 20.11	19.96	790503	$-3.82^{-3.80}_{-3.85}$	$-3.56^{-3.50}_{-3.61}$	$1.88^{1.92}_{1.84}$
	19.51, 19.81	19.66	692920	$-3.78^{-3.76}_{-3.81}$	$-3.43^{-3.39}_{-3.48}$	$1.85^{1.88}_{1.82}$
	19.21, 19.51	19.37	596349	$-3.75^{-3.72}_{-3.78}$	$-3.31^{-3.26}_{-3.35}$	$1.81^{1.85}_{1.78}$
	18.91, 19.21	19.06	518696	$-3.74^{-3.71}_{-3.77}$	$-3.27^{-3.22}_{-3.31}$	$1.80^{1.83}_{1.77}$
	18.61, 18.91	18.78	434355	$-3.67^{-3.65}_{-3.69}$	$-3.25^{-3.23}_{-3.27}$	$1.82^{1.83}_{1.81}$
	18.31, 18.61	18.48	257434	$-3.55^{-3.53}_{-3.57}$	$-3.20^{-3.17}_{-3.23}$	$1.85^{1.86}_{1.83}$
	18.01, 18.31	18.19	137380	$-3.43^{-3.41}_{-3.46}$	$-3.01^{-2.96}_{-3.06}$	$1.82^{1.85}_{1.78}$
0.005°, 1°	20.11, 20.41	20.26	868849	$-3.90^{-3.88}_{-3.92}$	$-3.65^{-3.60}_{-3.70}$	$1.90^{1.93}_{1.87}$
	19.81, 20.11	19.96	790503	$-3.87^{-3.85}_{-3.88}$	$-3.68^{-3.63}_{-3.74}$	$1.92^{1.95}_{1.89}$
	19.51, 19.81	19.66	692920	$-3.81^{-3.80}_{-3.83}$	$-3.67^{-3.62}_{-3.73}$	$1.94^{1.97}_{1.91}$
	19.21, 19.51	19.37	596349	$-3.78^{-3.76}_{-3.80}$	$-3.61^{-3.56}_{-3.67}$	$1.93^{1.96}_{1.90}$
	18.91, 19.21	19.06	518696	$-3.76^{-3.74}_{-3.77}$	$-3.62^{-3.56}_{-3.67}$	$1.94^{1.96}_{1.91}$
	18.61, 18.91	18.78	434355	$-3.68^{-3.67}_{-3.69}$	$-3.55^{-3.51}_{-3.59}$	$1.94^{1.96}_{1.92}$
	18.31, 18.61	18.48	257434	$-3.55^{-3.54}_{-3.57}$	$-3.45^{-3.40}_{-3.49}$	$1.94^{1.97}_{1.92}$
	18.01, 18.31	18.19	137380	$-3.43^{-3.41}_{-3.44}$	$-3.40^{-3.33}_{-3.47}$	$1.97^{2.00}_{1.94}$

Table 3.9: Best fit parameters from modelling the angular clustering of LRGs in z-band magnitude bins using Equation 3.5. The clustering amplitude A_w is reported for a fixed slope of $\gamma = 1.98$ (taken from the fit over the full LRG sample; see Table 3.6), as well as the results of fitting amplitude and slope simultaneously. $\theta_{\rm min}$ and $\theta_{\rm max}$ are the angular scales fit over, and m_z is in AB magnitudes.

ELG						
$\theta_{\rm min}$, $\theta_{\rm max}$	m_z bin	med m_z	# objects	$\log_{10} A_w$ ($\gamma = 1.54$)	$\log_{10} A_w$	γ
0°, 0.05°	23.1, 23.4	23.27	8530522	$-3.15^{-3.08}_{-3.22}$	$-4.10^{-3.98}_{-4.22}$	$1.80^{1.87}_{1.73}$
	22.8, 23.1	22.97	4768510	$-2.98^{-2.91}_{-3.07}$	$-4.66^{-4.59}_{-4.72}$	$1.99^{2.02}_{1.95}$
	22.5, 22.8	22.68	2462312	$-2.67^{-2.59}_{-2.76}$	$-4.43^{-4.32}_{-4.54}$	$2.00^{2.05}_{1.95}$
	22.2, 22.5	22.38	1224671	$-2.36^{-2.27}_{-2.47}$	$-4.09^{-3.94}_{-4.24}$	$2.00^{2.06}_{1.94}$
	21.9, 22.2	22.07	614394	$-1.97^{-1.88}_{-2.09}$	$-3.68^{-3.53}_{-3.84}$	$2.00^{2.05}_{1.95}$
	21.6, 21.9	21.77	334669	$-1.74^{-1.61}_{-1.90}$	$-3.31^{-3.16}_{-3.47}$	$2.00^{2.05}_{1.95}$
	21.3, 21.6	21.47	205434	$-1.74^{-1.45}_{-2.28}$	$-3.00^{-2.90}_{-3.11}$	$2.00^{2.03}_{1.97}$
	21.0, 21.3	21.16	138431	$-1.74^{-1.17}_{-2.31}$	$-2.68^{-2.62}_{-2.75}$	$2.00^{2.01}_{1.98}$
0.05°, 1°	23.1, 23.4	23.27	8530522	$-3.23^{-3.21}_{-3.26}$	$-2.93^{-2.87}_{-2.99}$	$1.43^{1.48}_{1.39}$
	22.8, 23.1	22.97	4768510	$-3.15^{-3.13}_{-3.17}$	$-2.80^{-2.79}_{-2.82}$	$1.41^{1.42}_{1.40}$
	22.5, 22.8	22.68	2462312	$-2.99^{-2.98}_{-3.01}$	$-2.76^{-2.74}_{-2.78}$	$1.45^{1.46}_{1.44}$
	22.2, 22.5	22.38	1224671	$-2.77^{-2.76}_{-2.78}$	$-2.64^{-2.62}_{-2.65}$	$1.49^{1.50}_{1.48}$
	21.9, 22.2	22.07	614394	$-2.47^{-2.46}_{-2.48}$	$-2.53^{-2.49}_{-2.58}$	$1.56^{1.59}_{1.54}$
	21.6, 21.9	21.77	334669	$-2.22^{-2.19}_{-2.25}$	$-2.51^{-2.42}_{-2.60}$	$1.66^{1.71}_{1.61}$
	21.3, 21.6	21.47	205434	$-2.04^{-2.01}_{-2.08}$	$-2.47^{-2.33}_{-2.61}$	$1.72^{1.80}_{1.65}$
	21.0, 21.3	21.16	138431	$-1.93^{-1.89}_{-1.97}$	$-2.37^{-2.17}_{-2.57}$	$1.72^{1.83}_{1.62}$
0°, 1°	23.1, 23.4	23.27	8530522	$-3.17^{-3.12}_{-3.21}$	$-4.08^{-3.99}_{-4.17}$	$1.79^{1.85}_{1.74}$
	22.8, 23.1	22.97	4768510	$-3.05^{-2.99}_{-3.11}$	$-4.16^{-4.06}_{-4.25}$	$1.87^{1.92}_{1.81}$
	22.5, 22.8	22.68	2462312	$-2.80^{-2.73}_{-2.87}$	$-4.09^{-3.99}_{-4.19}$	$1.92^{1.96}_{1.87}$
	22.2, 22.5	22.38	1224671	$-2.53^{-2.45}_{-2.63}$	$-4.00^{-3.89}_{-4.11}$	$1.98^{2.02}_{1.94}$
	21.9, 22.2	22.07	614394	$-2.32^{-2.22}_{-2.43}$	$-3.69^{-3.59}_{-3.79}$	$2.00^{2.04}_{1.96}$
	21.6, 21.9	21.77	334669	$-2.13^{-2.04}_{-2.24}$	$-3.35^{-3.25}_{-3.44}$	$2.00^{2.03}_{1.97}$
	21.3, 21.6	21.47	205434	$-1.98^{-1.88}_{-2.09}$	$-3.11^{-2.99}_{-3.23}$	$2.00^{2.04}_{1.96}$
	21.0, 21.3	21.16	138431	$-1.89^{-1.80}_{-2.01}$	$-2.99^{-2.76}_{-3.22}$	$2.00^{2.09}_{1.91}$

Table 3.10: Best fit parameters from modelling the angular clustering of ELGs in g-band magnitude bins using Equation 3.5. The clustering amplitude A_w is reported for a fixed slope of $\gamma = 1.54$ (taken from the fit over the full ELG sample; see Table 3.6), as well as the results of fitting amplitude and slope simultaneously. $\theta_{\rm min}$ and $\theta_{\rm max}$ are the angular scales fit over, and m_g is in AB magnitudes.

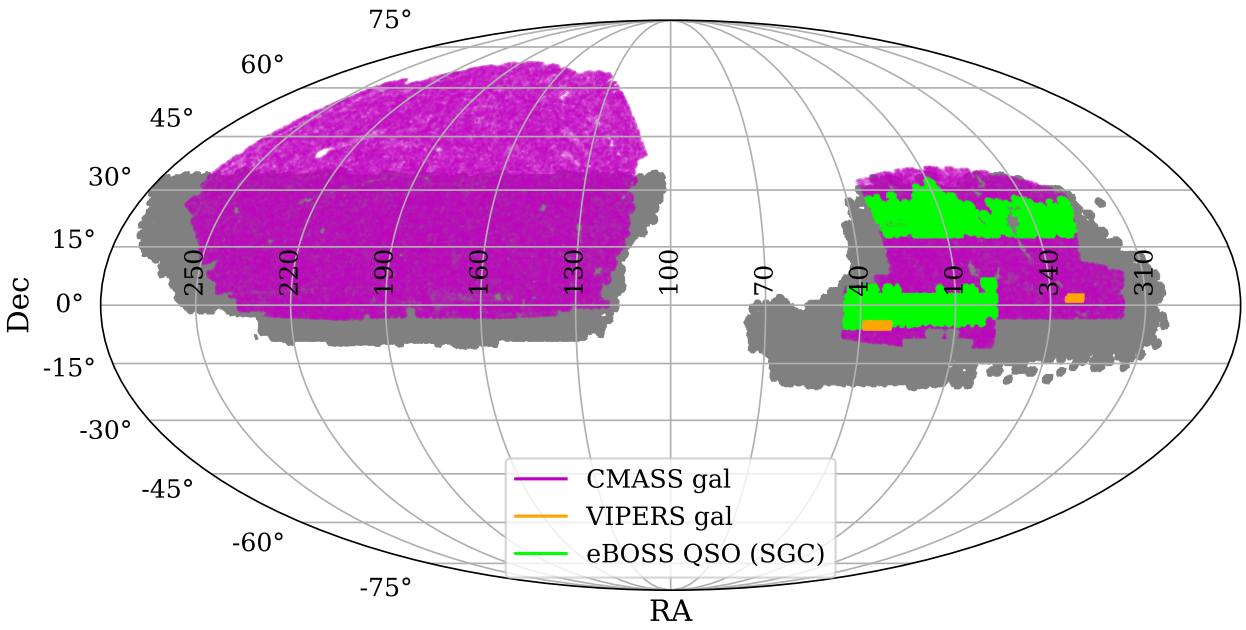

Figure 3.24: Visualizing the overlap between the DECaLS DR7 footprint (gray) and the footprints of the external catalogs used for cross-correlations. Positions are mapped using Mollweide projection.

systematics in the two catalogs, likely the anti-correlation with stars found in both DESI ELGs and CMASS samples. The projected real-space cross-correlations are plotted in Figure 3.27, along with the power-law predictions from the ELG $w(\theta)$ fits in Table 3.6, which we translate into $w_p(r_p)$ using Equation 3.7. We thus have consistency between ELG $w(\theta)$ in Figure 3.16, C_ℓ in Figure 3.18, and $w_p(r_p)$ in Figure 3.27. We also note that the break at small scales becomes less pronounced at higher redshift, as the 2-halo term becomes more dominant.

More puzzlingly, ELGs appear to show no correlation with eBOSS QSOs over the overlapping redshift range. This null signal is consistent within error bars across all redshift bins, and remains null even when switching to brighter ELG subsamples. At present, we wish to avoid speculating on why there is no cross-correlation between ELGs and eBOSS QSOs, as a full investigation with survey validation data and spectra is expected to paint a much clearer picture. Given the reasonable ELG autocorrelation and ELG $\times$ CMASS cross-correlation, we do not believe this is indicative of catastrophic failure in the ELG sample. Finally, we note that the QSO cross-correlations are too noise-dominated to obtain a meaningful signal.

Clustering dN/dz

For ELGs and QSOs, issues with cross-correlation measurements discussed in the previous section prevent us from obtaining meaningful dN/dz over the full redshift ranges of the

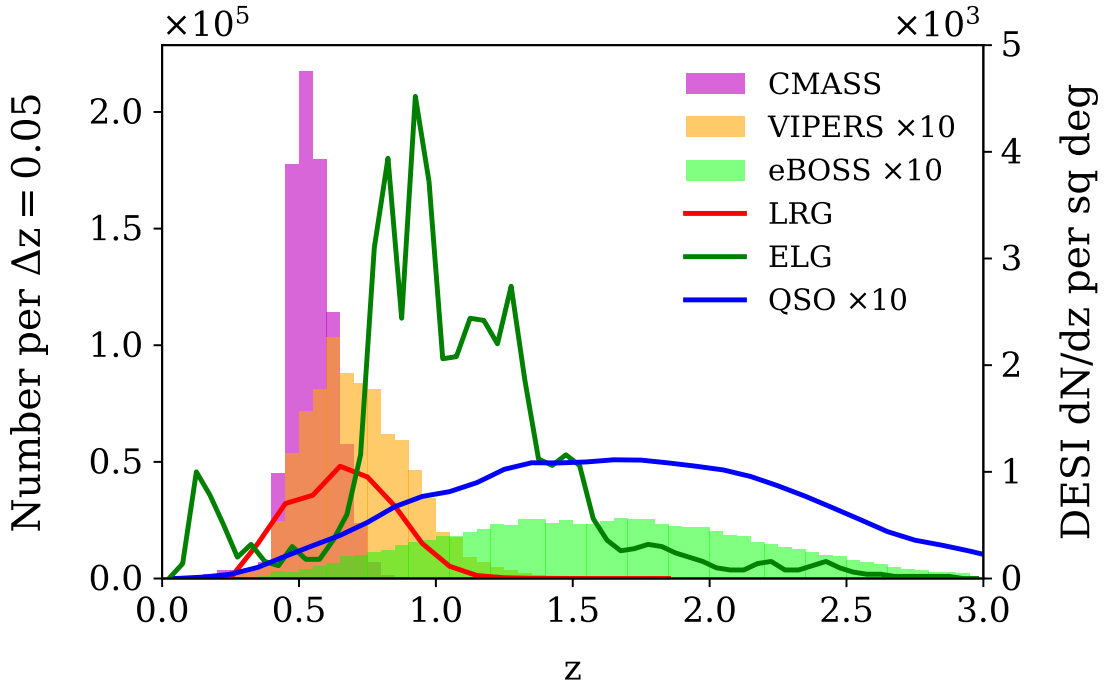

Figure 3.25: Visualizing the redshift ranges for DESI targets compared to catalogs from spectroscopic surveys which overlap the DECaLS footprint. The solid lines correspond to the expected dN/dz per square degree of the DESI target classes, while the histograms are from the external catalogs.

targets. We therefore focus on LRGs and defer further investigation of ELGs and QSOs to a future work.

Using the method outlined in Section 3.2, we integrate over each set of cross-correlations in the overlapping redshift ranges to piece together the shape of the LRG dN/dz. We choose the minimum and maximum physical scales of integration in such a way as to reduce the propagated errors on dN/dz; for LRG $\times$ CMASS and LRG $\times$ VIPERS, we use $s_{\rm min} = 0.05$ h^{-1} Mpc, $s_{\rm max} = 5$ h^{-1} Mpc, whereas for LRG $\times$ eBOSS we use $s_{\rm min} = 0.2$ h^{-1} Mpc, $s_{\rm max} = 10$ h^{-1} Mpc.

To minimize the potential impact of bias evolution in the photometric sample, we first divide it by color before cross-correlating each subsample separately, as discussed by Ménard et al. (2013), Schmidt et al. (2013), Rahman et al. (2015), Gatti et al. (2018),. In Figure 1 of Prakash et al. (2016), the photometric redshifts of eBOSS LRGs are plotted in color-space, with a transition from mostly $z < 0.6$ objects to mostly $0.6 < z < 1.0$ objects occurring when $r - W1$ is in the range between 2 and 3. Motivated by this, we select a roughly median value of $r - W1 = 2.6$ to create two similarly sized LRG subsamples. We cross-correlate these two subsamples separately with the three external catalogs, with the combined results

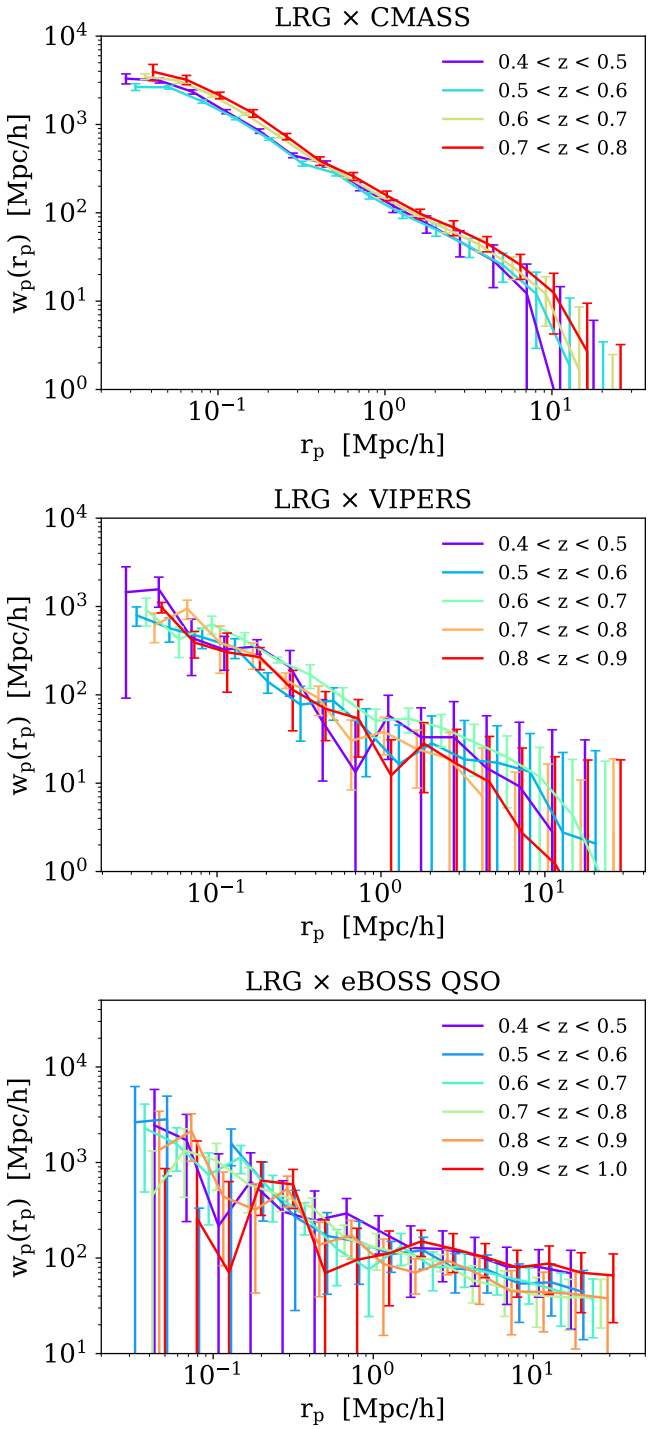

Figure 3.26: Projected real-space cross-correlations between LRGs and three external samples with spectroscopic redshifts: CMASS galaxies, VIPERS galaxies, and eBOSS QSOs. Error bars are from bootstrapping.

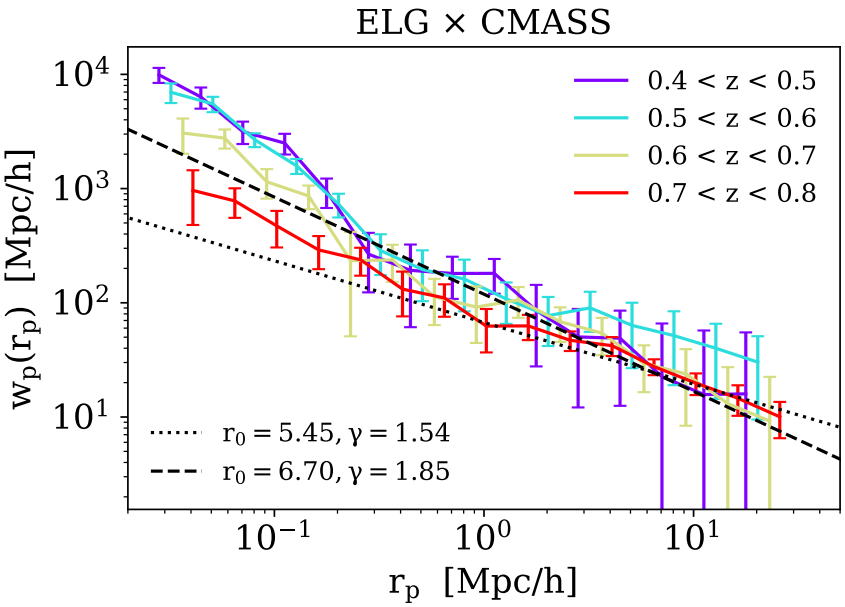

Figure 3.27: Projected real-space cross-correlations between ELGs and CMASS galaxies. Error bars are from bootstrapping. Dashed and dotted lines are the power-law fits of the ELG autocorrelation from Table 3.6.

shown in Figure 3.28 and compared to the results derived without binning the sample.

We find that the clustering dN/dz from all three cross-correlations match very well with the fiducial FDR dN/dz.[19] Along with the excellent agreement between measured and fiducial bias found in Section 3.7, this suggests that the LRG sample will be able to fully meet the cosmology goals of the collaboration. Additionally, the upper panel of Figure 3.28 confirms that the color cut at $r - W1 = 2.6$ effectively splits the LRG sample into high and low redshift subsamples with an approximate boundary at $z \sim 0.65$.

Clustering as a function of luminosity

By cross-correlating magnitude binned LRGs with redshift binned spectroscopic catalogs, we can also probe the luminosity dependence of the sample. We begin by dividing the LRGs into three broader magnitude bins from $m_z = 18.01$ to $m_z = 20.41$, the bright and faint limits, respectively, of the target selection. To improve signal-to-noise, we also double the widths of the redshift bins to $\delta z = 0.2$ and focus on the cross-correlations with CMASS galaxies, which involve the smallest error bars. Through these cross-correlations, we can crudely reconstruct dN/dz for each of the magnitude bins, shown in Figure 3.29. The behavior

[19] We note that the fiducial redshift distributions in Figure 3.25 are of the targets selected from imaging, including contaminants.

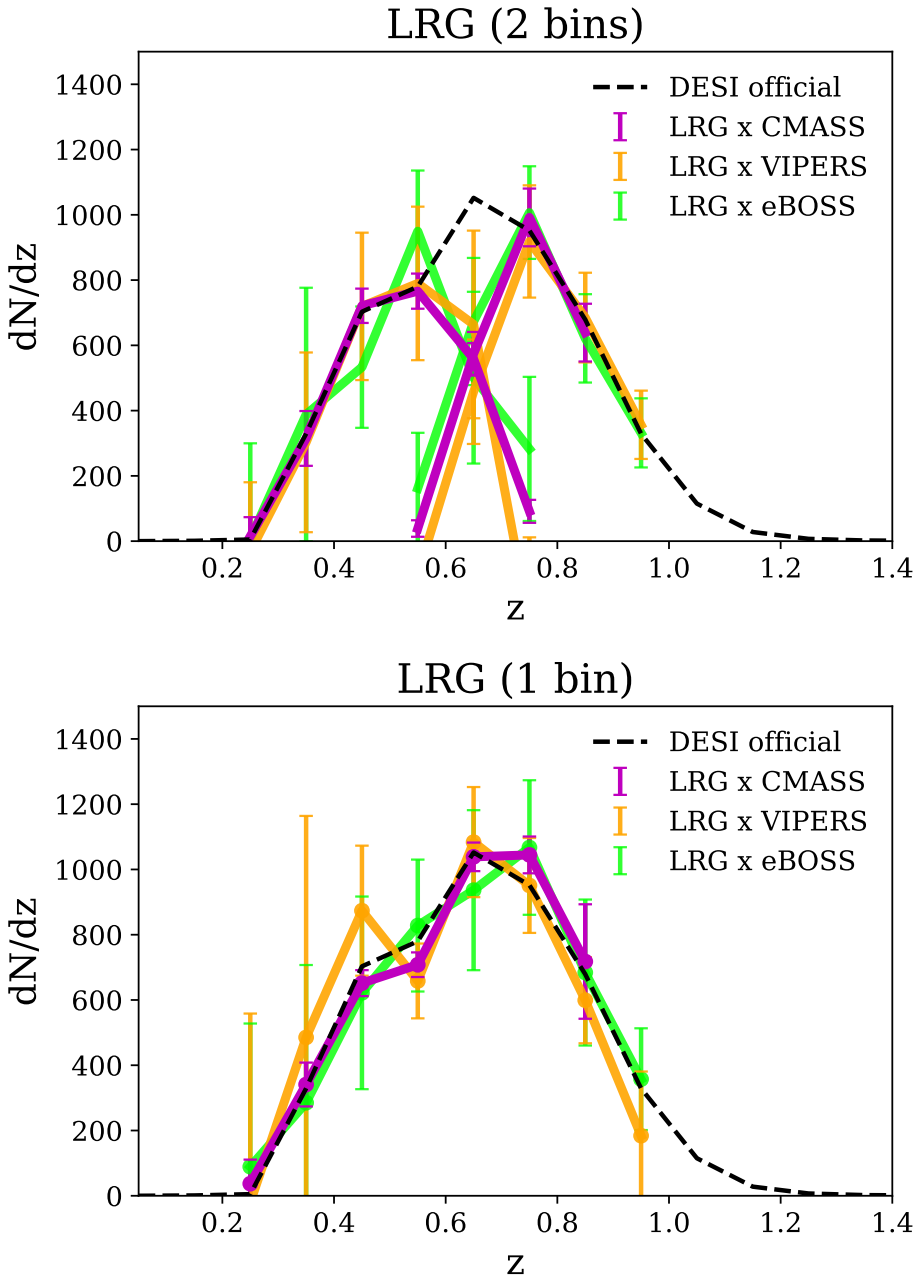

Figure 3.28: The clustering-based dN/dz for LRGs derived from cross-correlations with CMASS galaxies (magenta), VIPERS galaxies (orange), and eBOSS QSOs (lime), with the expected dN/dz plotted as a dashed line. The upper plot shows dN/dz calculated using two $r-W1$ color bins, a proxy for a $z \sim 0.6$ cut in order to reduce the impact of bias evolution, while the lower plot is determined using the full sample. Error bars are from propagating bootstrap errors from the cross-correlations through the dN/dz calculation.

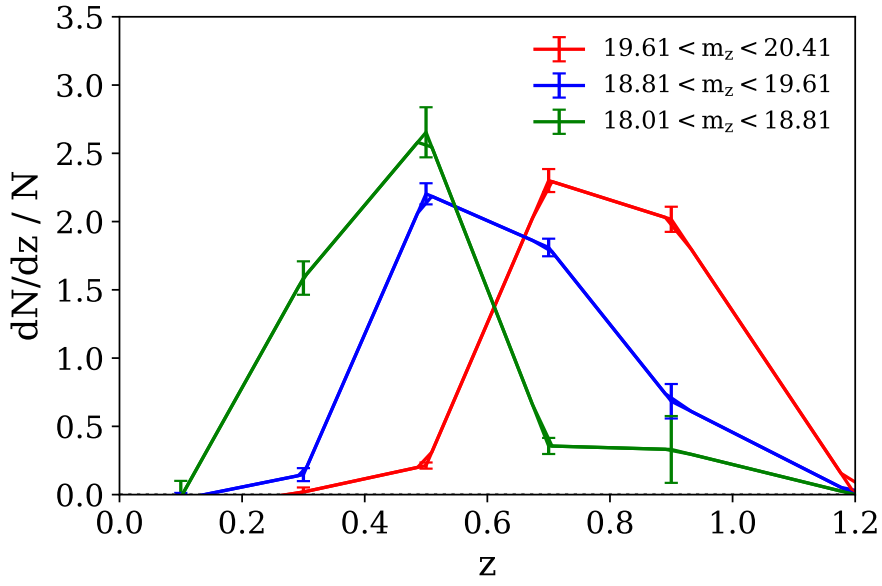

Figure 3.29: Normalized dN/dz for each of three broad magnitude bins, derived from cross-correlations with CMASS galaxies in broad redshift bins of $\delta z = 0.2$. Error bars are from propagating bootstrap errors from the cross-correlations through the dN/dz calculation.

is as expected; brighter objects are at lower mean redshift, with the redshift distributions generally appearing as deeper and deeper copies of each other.

This result allows us to convert angular cross-correlations into projected real-space cross-correlations, as detailed in Section 3.2, giving us $w_p(r_p)$ in three broad luminosity bins for a given redshift bin. We select a bin near the middle of the CMASS redshift range[20], $0.4 < z < 0.6$, and fit the clustering for each corresponding luminosity bin to a power law, $w_p(r_p) = Ar_p^{1-\gamma}$. The results are given in Table 3.11.

3.9 Summary and Conclusions for Chapter 3

In order to fully realize the statistical power of the DESI experiment, it is vital to assess the quality of the imaging data and target definitions, and to account for any non-cosmological sources of spatial fluctuations in the galaxy catalogs that could bias the cosmological analyses. In the first part of this chapter, we diagnose causes of systematic errors in the clustering of DESI main targets selected from imaging and present masks and photometric weights aimed at reducing these effects. The masks and weights will be used in construction of cosmological clustering samples. Our key results are summarized below:

[20]Since CMASS galaxies are selected by color cuts, as are our LRGs, objects at the edges of the redshift range (particularly the low end, where interlopers become more probable) may be physically different from objects in the middle, with different clustering.

LRG × CMASS, $0.4 < z < 0.6$		
m_z bin	$M_z(\bar{z} = 0.5)$	$\log_{10} A$ ($\gamma = 1.98$)
19.61, 20.41	-21.87, -21.07	$-3.40\ ^{-3.36}_{-3.44}$
18.81, 19.61	-22.67, -21.87	$-2.51\ ^{-2.49}_{-2.53}$
18.01, 18.81	-23.47, -22.67	$-2.56^{-2.54}_{-2.59}$

Table 3.11: Fits to the luminosity binned LRG-CMASS cross-correlations assuming $w_p(r_p) = Ar_p^{1-\gamma}$. The first column specifies the LRG apparent magnitude bins, while the second column calculates the corresponding absolute magnitude bin at the midpoint of the CMASS redshift bin $0.4 < z < 0.6$.

- We find that obscuration due to bright stars in the foreground creates significant variations in density, particularly for QSOs. Implementing aggressive masks around Tycho-2 and WISE stars, which remove 7-8% of the usable sky area for galaxies and 28% of the usable sky area for QSOs, dramatically improves the agreement of the angular correlation functions with cosmological predictions.
- We determine that a general mask around large galaxies and other extended sources is not indicated; however, by visual inspection, we discover that failing to mask around the Coma cluster and M3 will create a significantly overestimated clustering signal for QSOs in the north galactic cap. Additionally, the images of a small number of very bright stars are plagued by complex patterns of reflected pupil ghosts, which create structures in the ELG density beyond the scope of even our highly conservative bright star masks.
- We find that masked LRGs exhibit only minor density variations as a function of potential systematics such as stellar density, extinction, airmass, seeing, sky brightness, and exposure time. By contrast, masked ELG and QSO densities still fluctuate significantly, with the most dominant systematics, stellar density and extinction, affecting densities by as much as 10%. We find that ELGs are anti-correlated with stars and extinction, while QSOs are positively correlated. Photometric weights calculated by performing multilinear regression on these trends significantly ameliorates them.
- We perform angular cross-correlations between the targets and stars, and again find that LRGs are uncorrelated, ELGs are anti-correlated, and QSOs are positively correlated. Dividing the stars into three galactic latitude bins, we use QSO-star cross-correlations and star autocorrelations to estimate the stellar contamination fraction in the QSO sample as a function of galactic latitude.

We stress that this process has been highly iterative, with our efforts continuously informing the evolution of DESI's imaging data reduction pipelines and target selection algorithms.

The Legacy Survey Data Release 9, which is currently being processed and will be used for DESI target selection, has made several algorithmic upgrades motivated in part by the feedback in this study. These include changes to the pixel-level flat-field response functions and an improved modeling of sky subtraction. The latter improvements are most pronounced for ELG targets that are faint relative to the sky and therefore have their target densities modulated by errors in the sky modeling. The new sky model also helps with issues of scattered light around bright stars that affect the selection of QSO targets. In addition, the imaging team has added more aggressive foreground masking and has flagged other bad data from the list of problematic regions identified in this study (such as the ghost pupils around certain visibly bright stars, and the M3/NGC contaminants in the north). Similarly, the target selection algorithms have been iteratively updated many times in response to our findings.

In addition to being a crucial first step towards constraining cosmology with DESI clustering measurements, our findings have important implications for other ongoing and future imaging surveys. As multi-epoch surveys become deeper and more sensitive, they will be increasingly limited by systematic uncertainties from instrument calibration, survey characteristics, and observing conditions. Our framework for identifying and mitigating the effects of such systematics, such as our new approach to quantifying contamination due to stars, is therefore highly relevant and widely applicable to future imaging surveys.

After applying masks and weights, we devote the second part of this chapter to modeling the properties of the samples, providing the first large-scale clustering analysis of DESI targets. Modeling the samples is an important first step for doing cosmology with DESI, and our clustering results will also aid in the creation and validation of accurate mock catalogs. Additionally, we present several new methodologies, including the technique of probing the luminosity dependent clustering by cross-correlating magnitude-binned photometric samples with redshift-binned spectroscopic samples. These methods can be applied to other clustering studies with deep photometric data, for instance in future studies with data from the Large Synoptic Survey Telescope (LSST Science Collaboration et al., 2009). Our main results are outlined below:

- We present the average densities before and after the corrections have been applied, finding that all three target densities are in reasonably good agreement with expectation after masking and weighting.

- We model the angular correlation functions of the samples, assuming power law spatial correlation functions. For LRGs, we recover values which agree very well with earlier studies. For ELGs, we see a broken power law, with different slopes for $\theta < 0.01^\circ$ and $\theta > 0.05^\circ$ which agree reasonably well with similar studies. For QSOs, we obtain a highly inflated value for the clustering amplitude, indicating that substantial contamination remains.

- We compare the observed angular power spectra to theory to determine the linear large-scale bias, and also probe the scale dependence of the bias in the weakly nonlinear regime. For LRGs, we find a value of b_0 that agrees very well with the DESI FDR prediction. For

ELGs, we find a value of b_0 that is higher than the conservative lower limit given by the FDR but is similar to values from the literature and is self-consistent with our angular and real-space clustering measurements. By contrast, the observed angular power spectrum for QSOs is a poor fit to theory, with all scales seemingly affected by non-cosmological signals.

- We use cross-correlations with external spectroscopy to determine real-space projected cross-correlation functions in redshift bins, through which we also derive clustering dN/dz. For LRGs, the clustering as a function of redshift behaves as expected, and we see an excellent match with the expected dN/dz from target selection. For ELGs, the redshift-binned cross-correlations with CMASS are consistent with expectation, but cross-correlations with eBOSS QSOs show no significant correlation. For QSOs, the cross-correlations are not currently clean enough to meaningfully model dN/dz.

- The clustering of LRGs and ELGs as a function of magnitude also behaves as predicted, with clustering amplitude scaling with depth. We provide fits to the angular correlation functions in magnitude bins. We also cross-correlate magnitude binned LRGs with redshift binned CMASS galaxies to probe luminosity dependent clustering.

- We present counts-in-cells moments and cell-averaged higher order correlation functions to further facilitate mock calibration and validation.

Overall, our results suggest that the quality of the imaging and the selection of targets are suitable for achieving the ambitious scientific objectives of the DESI collaboration. With imaging surveys completed and spectroscopic first light announced in October 2019, the commissioning phase is on track for completion in January 2020. After a survey validation period in the spring, the 5-year survey is expected to begin in the summer of 2020. We look forward to the exciting and impactful new science that DESI will enable in the coming decade.

Chapter 4

Cross-Correlating DESI LRGs with CMB Lensing

Cross-correlations between the lensing of the cosmic microwave background and tracers of large-scale structure provide a unique way to reconstruct the growth of dark matter, break degeneracies between cosmology and galaxy physics, and test theories of modified gravity. In this chapter, we present a detection of the cross-correlation between DESI-like luminous red galaxies (LRGs) selected from DECaLS imaging and CMB lensing maps reconstructed with the Planck satellite at a significance of $S/N = 27.2$ over scales $\ell_{\rm min} = 30$, $\ell_{\rm max} = 1000$. To correct for magnification bias, we determine the slope of the LRG cumulative magnitude function at the faint limit as $s = 0.999 \pm 0.015$, finding corrections on the order of a few percent for $C_\ell^{\kappa g}, C_\ell^{gg}$ across the scales of interest. We fit the large-scale galaxy bias at the effective redshift of the cross-correlation $z_{\rm eff} \approx 0.68$ using two different bias evolution agnostic models: a HaloFit times linear bias where the bias evolution is folded into the clustering-based estimation of the redshift kernel, and a Lagrangian perturbation theory model of the clustering evaluated at $z_{\rm eff}$. We also determine the error on the bias from uncertainty in the redshift distribution; within this error, the two methods show excellent agreement with each other and with DESI survey expectations.

4.1 Introduction

Modern cosmology hinges on observations of the large-scale structure of the Universe, which is rich with clues about gravity, dark energy, and the mechanisms of cosmic expansion. Next-generation galaxy surveys, including spectroscopic experiments such as the Dark Energy Spectroscopic Instrument (DESI, DESI Collaboration et al. 2016) and deep imaging experiments such as the Large Synoptic Survey Telescope (LSST, LSST Science Collaboration et al. 2009), will map billions of galaxies in the coming decade and tighten constraints on key fundamental parameters. While spectroscopic redshifts can be obtained for some subset of imaged galaxies, the majority will increasingly rely on photometric redshift estimates (see

e.g. Hogg et al. 1998 and references contained therein) or clustering-based redshift estimates (see e.g. Newman 2008), enabling higher number density but noisier catalogs of galaxy positions.

Measurements of the cosmic microwave background (CMB) provide another window into the growth of large-scale structure, due to the lensing of the CMB photons as they free-stream through the Universe and are deflected (on the order of a few arcminutes) by the gravitational potentials of matter in their path. In the weak regime, gravitational lensing remaps the CMB temperature and polarization primary anisotropies in predictable ways that can be exploited to reconstruct high resolution maps of the projected matter density over the past 13 billion years (Zaldarriaga & Seljak 1999, Hu & Okamoto 2002, Lewis & Challinor 2006). Detections of this mass lensing signal from the CMB have been made in a number of ways, including cross-correlations with other tracers of large-scale structure (see e.g. Omori et al. 2019 for a recent list).

CMB lensing offers the advantage of directly probing the underlying distribution of dark matter, but suffers from information loss since it is a two-dimensional projection of the three-dimensional matter density integrated along the line of sight from the surface of last scattering ($z \approx 1100$) to the present day. In contrast, galaxy samples with narrow redshift windows are relatively well localized in position but are biased tracers of dark matter due to the complex processes involved in galaxy formation. This leads to degeneracies between these galaxy bias parameters and cosmological parameters of interest such as σ_8. Cross-correlations between CMB lensing and galaxy catalogs thus provide a means to chart the growth of dark matter with time and break the degeneracy between galaxy physics and cosmology. Additionally, on a practical level, systematics in the galaxy sample are unlikely to be correlated to systematics in the CMB lensing maps, and a higher degree of uncertainty in the galaxy redshift distribution can also be tolerated due to the broad redshift kernel of the CMB lensing.

In this work, we leverage the high number density and completeness of the luminous red galaxy (LRG) target class as defined by DESI and selected from deep multi-band imaging, in combination with the all-sky CMB lensing convergence maps of the Planck collaboration, to detect a galaxy-matter cross-correlation at high significance out to small scales $\ell_{\rm max} = 1000$. We jointly model the angular auto- and cross- spectra to probe the amplitude and evolution of the galaxy bias. In the absence of spectroscopic redshifts, we use a combination of photometric and clustering-based estimations of the galaxy redshift distribution. Within a simple linear bias model $P_{\rm gg}(k,z) \approx b_{\rm g}(z) P_{\rm mm}(k,z)$, the advantage of the the clustering-based method is that it allows us to measure an effective bias without assuming a bias evolution model. By comparing results using photometric versus clustering redshift distributions, we also evaluate the impact of uncertainty in the redshift distribution on the inferred parameters.

This chapter is organized as follows: Section 4.2 describes the lensing products and imaging data, and outlines the construction of the DESI-like LRG catalog. In Section 4.3, we characterize the redshift distribution of the galaxy sample based on angular cross-correlations with external spectroscopic catalogs, and present a framework for modeling bias evolution using these results. Section 4.4 outlines our methods for measuring and modelling angular

power spectra and covariances on a partial sky. Section 4.5 is devoted to determining and applying corrections for the effects of magnification bias. In Section 4.6, we present and model the resulting spectra, with Section 4.6 fitting the linear Eulerian galaxy bias under the HaloFit (Smith et al., 2003) prescription while Section 4.6 interprets the results within a Lagrangian perturbation theory framework. Finally, in Section 4.7, we summarize our findings and suggest future directions.

Throughout, we work in co-moving coordinates and assume the fiducial cosmology of the Planck 2018 results (Planck Collaboration et al. 2018a, Table 2, Column 7). All magnitudes are quoted as AB magnitudes, unless otherwise specified.

4.2 Data

Planck CMB lensing maps

Using the most recent reconstructed lensing convergence maps and analysis masks provided in the Planck 2018 release[1] (Planck Collaboration et al., 2018b), we focus mainly on the baseline estimates obtained from the SMICA DX12 CMB maps with a minimum-variance (MV) estimate determined from both the temperature and polarization maps. To gauge the impact of the thermal Sunyaev-Zeldovich (tSZ) effect, which has been shown to bias the lensing reconstruction and contaminate cross-correlations with other tracers of large-scale structure (see e.g. Osborne et al. 2014; van Engelen et al. 2014; Madhavacheril & Hill 2018; Schaan & Ferraro 2019), we also repeat the analysis using the lensing estimate obtained from a temperature-only SMICA map where tSZ has been deprojected using multifrequency component separation. Throughout the remainder of this chapter, these two lensing maps will be referred to as `BASE` and `DEPROJ`, respectively.

The spherical harmonic coefficients of the reconstructed lensing convergence maps are provided in HEALPix[2] (Górski et al., 2005) format with maximum order $\ell_{\rm max} = 4096$, and the associated analysis masks are given as HEALPix maps with resolution $N_{\rm SIDE} = 2048$. The approximate lensing noise power spectrum for the fiducial cosmology used in Planck Collaboration et al. (2018b) is also provided up to $\ell_{\rm max} = 4096$.

Photometric DESI LRGs

The Dark Energy Spectroscopic Instrument (DESI; DESI Collaboration et al. 2016) is an upcoming Stage IV[3] dark energy experiment, installed on the Mayall 4m telescope at Kitt Peak. DESI aims to produce the largest ever three-dimensional map of the Universe, with a massively multiplexed spectrograph that will use robotic fiber positioners to measure as many as 5000 spectra in parallel. Among the four main classes targeted by DESI are luminous

[1] `https://wiki.cosmos.esa.int/planck-legacy-archive`
[2] `http://healpix.sf.net`
[3] As defined in the Dark Energy Task Force report (Albrecht et al., 2006).

red galaxies (LRGs) out to $z \approx 1$. LRGs, as their name suggests, are luminous and intrinsically red due to their high stellar mass and lack of recent star formation activity. LRGs are excellent tracers of large-scale structure; as early-type galaxies with generally old populations of stars, they are expected to reside in massive halos and therefore cluster strongly. Furthermore, their inherent brightness and the strong 4000Å feature in their spectral energy distributions enable the efficient selection of a homogeneous sample using photometry.

DECaLS imaging data

The DECam Legacy Survey (DECaLS) is a deep, wide-field survey providing the optical imaging used to conduct targeting for approximately two-thirds of the DESI footprint, covering the region bounded by $\delta \lesssim 32°$. Through the DECam instrument (Flaugher et al., 2015) on the Blanco 4m telescope, DECaLS observes in three optical and near-IR bands (g, r, z), with four additional mid-IR bands ($W1$, $W2$, $W3$, $W4$) provided by the Wide-field Infrared Survey Explorer (WISE; Wright et al. 2010). DECam images are processed and calibrated though the National Optical Astronomy Observatory (NOAO) Community Pipeline, then fed into *The Tractor*[4] (Lang et al., 2016), which uses forward-modeling to perform source extraction and produce probabilistic inference of source properties.

Our analysis is based on Data Release 8 (DR8), the final data release of the Legacy Survey (Dey et al., 2018), which contains DECaLS observations from August 2014 through March 2019 (NOAO survey program 0404). DR8 also includes some non-DECaLS observations from the DECam instrument, mainly from the Dark Energy Survey (DES; DES Collaboration et al. 2005). In total, the DECaLS +DES portion of DR8 covers approximately 14,996 square degrees in the g-band, 15,015 square degrees in the r-band, 15,130 square degrees in the z-band, and 14,781 square degrees in all three optical bands jointly.[5]

Galaxy selection

DESI LRGs are selected from DECaLS by applying a complex series of color cuts on extinction-corrected magnitudes in g, r, z, and $W1$:

$$\begin{gathered} z_{\text{fiber}} < 21.5 \\ r - z > 0.7 \\ (z - W1) > 0.8\,(r - z) - 0.6 \\ ((g - W1 > 2.6)\ \text{AND}\ (g - r > 1.4))\ \text{OR}\ (r - W1 > 1.8) \\ (r - z > (z - 16.83)\ 0.45)\ \text{AND}\ (r - z > (z - 13.80)\ 0.19) \end{gathered} \tag{4.1}$$

We note that the faint magnitude limit uses fiber flux, which is defined as the flux within

[4] https://github.com/dstndstn/tractor

[5] Estimated from using randoms distributed uniformly across the footprint to sum up the areas with at least one exposure in each band.

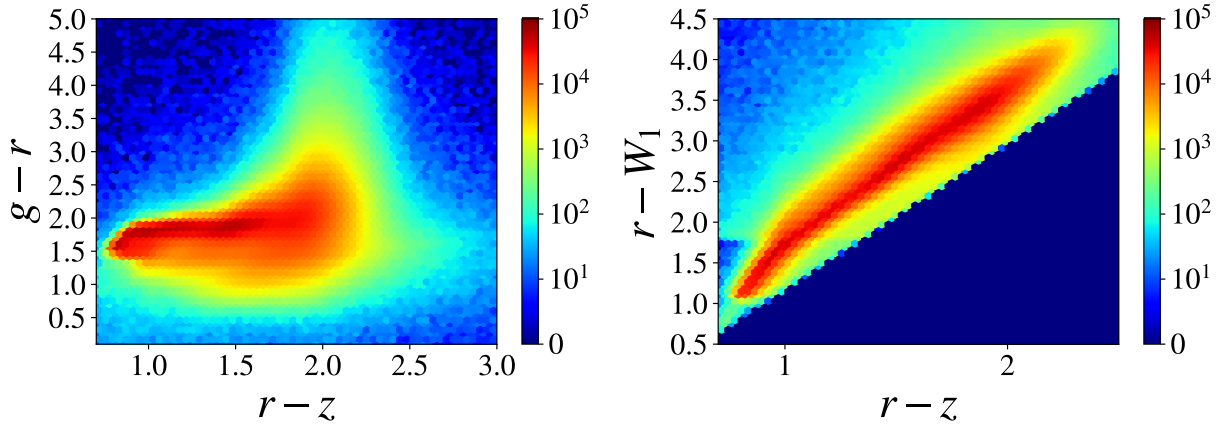

Figure 4.1: Color-color plots of the LRG target selection in DECaLS DR8.

a 1.5 arcsec diameter circular aperture centered on the model convolved with a 1.0 arcsec FWHM Gaussian. Color-color plots of the resulting sample are displayed in Figure 4.1.

Masks

Instrument effects and transients create artifacts in the images which may impact the detection or fitting of sources. Additionally, bright foregrounds, including point sources such as stars and extended sources such as large galaxies, globular clusters, and planetary nebulae, can contaminate the pixels around them with false targets, thereby affecting the apparent angular distribution of the target sample. DR8 provides bitmasks which leverage the NOAO Community Pipeline's data quality map, as well as several external catalogs, to reject bad pixels and mask around foregrounds. The bits we use in our analysis are summarized in Table 4.1 and briefly described below:

The `ALLMASK_X` bits are set for pixels that touch a bad pixel (as flagged by the NOAO Community Pipeline) in all of the overlapping X-band images. The `WISEM1` and `WISEM2` bits are set for pixels that touch a pixel in a mask around bright stars from the WISE catalog, with the two masks using the $W1$ and $W2$ bands, respectively. The `MEDIUM` bit is set for pixels that touch a pixel containing a medium-bright (`phot_g_mean_mag` < 16) star from the Gaia DR2 catalog (**?**) or a bright ($VT < 13$) star from the Tycho-2 catalog (Høg et al., 2000). The `GALAXY` bit is set for pixels that touch a pixel containing a large galaxy, where the source catalog used for this mask is taken from John Moustakas' Legacy Survey Large Galaxy Atlas[6] work with Dustin Lang. Finally, clusters and nebulae from OpenNGC[7] are masked around using a circular mask whose diameter is equal to the major axis of the object being masked, and the `CLUSTER` bit is set for pixels touching this mask.

[6] https://github.com/moustakas/LSLGA
[7] https://github.com/mattiaverga/OpenNGC

Mask		Number	Area (deg^2)	f_{survey}
no masks		9003243	14610.72	1.000
bits	ALLMASK_G	9002762	14610.72	1.000
	ALLMASK_R	9002742	14610.72	1.000
	ALLMASK_Z	9002458	14610.72	1.000
	WISEM1	8578461	14230.96	0.974
	WISEM2	8679070	14406.05	0.986
	MEDIUM	8566358	13945.27	0.954
	GALAXY	8996317	14599.17	0.999
	CLUSTER	9003232	14609.73	1.000
	all bits	8559863	13933.29	0.954
geometric	Tycho-2	8675511	14181.29	0.971
	WISE	8488111	14094.18	0.965
	all geometric	8399015	13859.42	0.949
all masks		8390823	13851.50	0.948

Table 4.1: Summary of foreground masks.

As demonstrated in Table 4.1, foreground stars are the dominant consideration. To determine whether any additional stellar masking is warranted, we measure the density of targets as a function of proximity to stars after the above bitmasks have been applied. Using the Tycho-2 and WISE catalogs, we first bin the stars by their magnitudes (using the VT and $W1$ bands, respectively), and then determine the density of LRGs in annular bins around these stacks of stars. We find that there are still residual effects near Tycho-2 stars, particularly for the brightest bins, that are not entirely captured by the bitmasks. We find even more significant effects around WISE stars, with the LRG density peaking beyond the radius of the bitmasks. We fit a magnitude-dependent masking radius for each star catalog to apply as additional geometric masks:

$$R = \begin{cases} 10^{\,3.41\,-\,0.16\,\times\,VT}\ \text{arcsec}, & \text{Tycho-2} \\ 10^{\,2.87\,-\,0.13\,\times\,W1}\ \text{arcsec}, & \text{WISE} \end{cases} \tag{4.2}$$

The addition of the geometric masks results in a slight increase in the total masked area.

Tests of potential systematics

Astrophysical foregrounds, poor observing conditions, and systematic errors in instrument calibration or data reduction can introduce non-cosmological density variations in the galaxy sample, which may in turn bias cosmological analyses (see e.g. Myers et al. 2006, Crocce et al. 2011, Ross et al. 2011, Suchyta et al. 2016, Crocce et al. 2016, Leistedt et al. 2016, Elvin-Poole et al. 2018 for studies of imaging systematics in the context of other surveys). A full analysis of the effect of imaging systematics on the clustering of DESI main targets using data from DECaLS DR7 is presented in Kitanidis et al. 2019. Here, we briefly perform tests of the LRG dependence on these potential systematics using DR8 data and target selection.

We use the `HEALPix` scheme with $N_{\mathrm{SIDE}} = 256$ to divide the footprint into pixels of equal area, over which we average each systematic. These pixelised maps are shown in Figure 4.2. The survey properties we look at are stellar density, galactic extinction, airmass, seeing, sky background, and exposure time. For full descriptions of these survey properties, how they are calculated, and why they are included in the analysis, see Section 6 of Kitanidis et al. 2019.

For each map, we bin the pixels by the value of the survey property, and then determine the average density per bin. The resulting plots of LRG density contrast $\delta = n/\bar{n} - 1$ as a function of survey properties are shown in Figure 4.3, with the cumulative sky fractions shown in the upper panels and the dotted lines corresponding to 1% fluctuations. We show that LRG density variation due to systematic sources of error are controlled to within 5% and, more often than not, 1%. As such, we conclude that imaging systematics should not significantly affect our cross-correlation measurements.

4.3 Galaxy Redshift Distribution

In order to convert between angular and 3D measurements, information about the distribution of the redshifts of the photometrically selected galaxies is required. One option is to use photometrically determined redshifts (photo-z's) for this purpose; for instance, Zhou et al. 2020 outlines a method for determining photo-z's for DESI LRGs selected from DECaLS DR7 using a machine learning method based on decision trees. We use the DR8 version of the resulting dN/dz provided by Rongpu Zhou in private communications. However, such methods have intrinsic scatter due to photometric errors and can be biased if the distribution of galaxies used in the training set is not representative of the overall population. It is thus useful to have an alternative method for estimating the redshift distribution, if only as a proxy to gauge the effect of errors in dN/dz on the desired parameter estimation. We apply a clustering-based redshift method, as described in the following sections.

Clustering redshift formalism

As modern deep imaging surveys probe ever greater volumes, they detect many more sources than can realistically be targeted for spectroscopy. The idea of leveraging cross-correlations

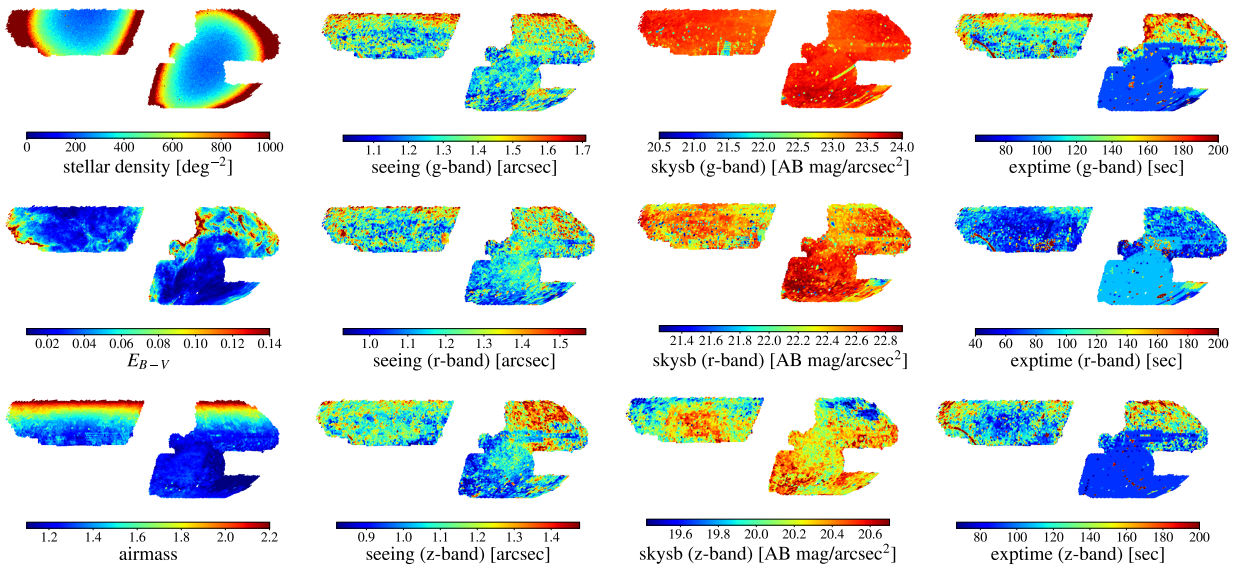

Figure 4.2: Maps of spatially-varying potential systematics in equatorial coordinates with Mollweide projection and the astronomy convention (east towards left).

between a spectroscopic sample and a photometric sample to infer redshift information about the latter is not a new one (see e.g. Seldner & Peebles 1979, Phillipps & Shanks 1987, Landy et al. 1996, Ho et al. 2008, Newman 2008). However, as clustering-based redshift estimation presents an attractive alternative to photometric redshift methods, it has experienced a recent resurgence in popularity. Over the last decade or so, a number of clustering dN/dz estimators have been presented and analyzed (Matthews & Newman 2010, Schulz 2010, Matthews & Newman 2012, McQuinn & White 2013, Ménard et al. 2013) and tested on real or simulated data (Schmidt et al. 2013, Scottez et al. 2016, Hildebrandt et al. 2017, Scottez et al. 2018, Davis et al. 2018, Gatti et al. 2018, Chiang et al. 2018, Kitanidis et al. 2019, Krolewski et al. 2019).

We use a version of the estimator proposed by Ménard et al. (2013), which exploits small-scale clustering information and avoids using autocorrelation functions since they are necessarily more impacted by systematic errors than cross-correlations. We provide a detailed derivation of our formalism and its assumptions in Appendix A, and simply state the key result here:

$$w_{\rm ps}(\theta, z_{\rm i}) \propto \phi_{\rm p}(z_{\rm i}) \frac{H(z_{\rm i})}{c} b_{\rm p}(z_{\rm i}) b_{\rm s}(z_{\rm i}) I(\theta, z_{\rm i}) \tag{4.3}$$

where $w_{\rm ps}$ is the angular cross-correlation, $\phi_{\rm p}(z_{\rm i})$ is the photometric redshift distribution, $b_{\rm p}(z_{\rm i})$ and $b_{\rm s}(z_{\rm i})$ are the large-scale biases of the two samples, and

$$I(\theta, z_{\rm i}) \equiv \int_{\chi_{\rm min}}^{\chi_{\rm max}} d\chi \; \xi_{\rm mm}\left(\sqrt{\chi_{\rm i}^2\theta^2 + (\chi - \chi_{\rm i})^2}, z_{\rm i}\right) \tag{4.4}$$

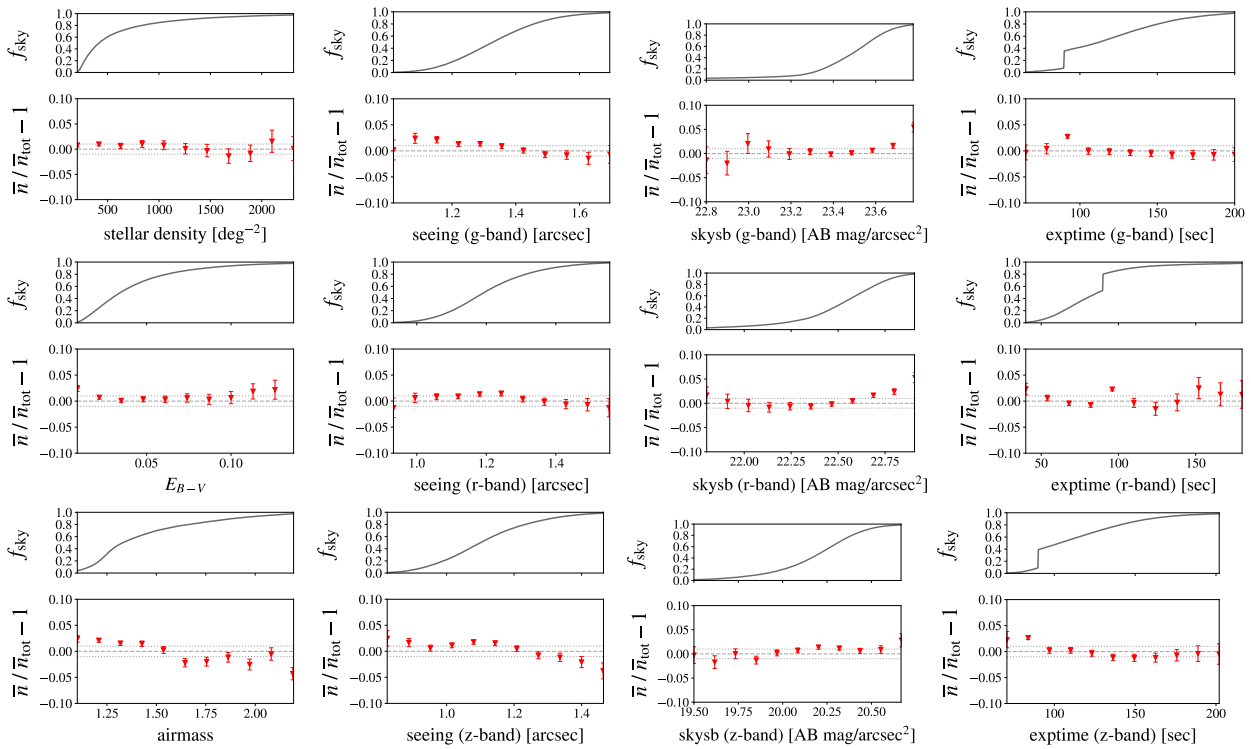

Figure 4.3: Density of LRGs as a function of stellar density, galactic extinction (color excess), airmass, seeing in each optical band, sky subtraction in each optical band, and exposure time in each optical band. Densities and survey properties are smoothed over the scale of the pixelised maps in Figure 4.2. The upper panels show the cumulative sky fractions for each survey property, and the dotted lines correspond to $\pm 1\%$ density fluctuations.

can be computed directly from Hankel transforming the theoretical dark matter power spectrum,

$$\xi_{\rm mm}(r, z) = \int_0^\infty \frac{dk}{2\pi^2} k^2 P_{\rm mm}(k, z) j_0(kr) \tag{4.5}$$

Bias evolution

Note that we do not need to know the amplitudes of the biases $b_{\rm p}$ and $b_{\rm s}$ in order to leverage Equation 4.3, since they are degenerate with the overall normalization of $\phi_{\rm p}$. We only need to know the shapes of the bias evolutions. For the spectroscopic catalog, this can be determined directly. For the photometric catalog, we use two complementary methods for modelling $b_{\rm p}(z) = b_0 \times f(z)$ for some unknown evolution $f(z)$:

1. Fit "effective" bias $b_{\rm eff} \equiv \int dz\ b_{\rm p}(z)\phi_{\rm p}(z)$.

2. Assume parametric form for $f(z)$, fit present day bias b_0.

These two methods are explained in detail in the subsections below.

Fit $b_{\rm eff}$ without parametric $f(z)$

In principle, we do not need to know the evolution of $b_{\rm p}$ in order to model the angular power spectra C_ℓ, since $b_{\rm p}(z)\phi_{\rm p}(z)$ is the quantity that enters the C_ℓ integrals for a linear bias model (see e.g. Equation 4.22). Equations 4.3-4.4 allow us to constrain $f(z)dN_{\rm p}/dz$ times some unknown proportionality constant.[8] After normalization, we obtain the quantity

$$q(z) \equiv \frac{f(z)dN_{\rm p}/dz}{\int dz'\ f(z')dN_{\rm p}/dz'} \tag{4.6}$$

Meanwhile, in the C_ℓ equations, the term $b_{\rm p}(z)\phi_{\rm p}(z)$ can be rewritten

$$b_{\rm p}(z)\phi_{\rm p}(z) = \frac{b_0 f(z)dN_{\rm p}/dz}{\int dz'\ dN_{\rm p}/dz'} = \frac{b_0 q(z)\int dz'\ f(z')dN_{\rm p}/dz'}{\int dz'\ dN_{\rm p}/dz'} \tag{4.7}$$

$$= b_{\rm eff} q(z) \tag{4.8}$$

where $b_{\rm eff}$ is the effective bias term

$$b_{\rm eff} \equiv \frac{b_0 \int dz\ f(z)dN_{\rm p}/dz}{\int dz\ dN_{\rm p}/dz} \tag{4.9}$$

$$= \int dz\ b_0 f(z)\phi_{\rm p}(z) = \int dz\ b_{\rm p}(z)\phi_{\rm p}(z) \tag{4.10}$$

Thus, by not assuming a shape for the bias evolution, we are fitting an integrated effective bias $b_{\rm eff}$ rather than the present day bias b_0. This $b_{\rm eff}$ essentially represents the bias weighted by the redshift distribution; for a sharply peaked photometric redshift distribution and weakly evolving bias as expected in the LRG sample, $b_{\rm eff} \approx b(z_{\rm eff})$.

Fit b_0 with parametric $f(z)$

Working with a parametric form (e.g. $b_p(z) = b_0/D(z)$ based on DESI's Final Design Report), b_0 can be measured directly. Equations 4.3-4.4 constrain $dN_{\rm p}/dz$ times some unknown proportionality constant. After normalizing to get $\phi_{\rm p}(z)$, we insert this into the C_ℓ integrals, along with the parametric $f(z)$. Thus by "floating" b_0 until theory matches observation, we obtain a value for b_0.

[8] We are using dN/dz to refer to the un-normalized redshift distributions, whereas $\phi(z)$ is normalized.

Integrating over scales

Following the method of Ménard et al. 2013, we integrate $w_{\rm ps}$ over a range of angular scales as the sensitivity of the estimator is improved by encoding information from many clustering scales. In order to maximize the SNR, we weight each point by θ^{-1}, which gives equal amounts of clustering information per logarithmic scale:

$$\bar{w}_{\rm ps}(z_{\rm i}) = \int_{\theta_{\rm min}}^{\theta_{\rm max}} d\theta \; \frac{1}{\theta} w_{\rm ps}(\theta, z_{\rm i}) \tag{4.11}$$

Hence, we have

$$\bar{w}_{\rm ps}(z_{\rm i}) \propto \phi_{\rm p}(z_{\rm i}) \frac{H(z_{\rm i})}{c} b_{\rm p}(z_{\rm i}) b_{\rm s}(z_{\rm i}) \bar{I}(z_{\rm i}) \tag{4.12}$$

where

$$\bar{I}(z_{\rm i}) = \int_{\theta_{\rm min}}^{\theta_{\rm max}} d\theta \; \frac{1}{\theta} \int_{\chi_{\rm min}}^{\chi_{\rm max}} d\chi \; \xi_{\rm mm}\left(\sqrt{\chi_{\rm i}^2\theta^2 + (\chi - \chi_{\rm i})^2}, z_{\rm i}\right) \tag{4.13}$$

In order to integrate over the same range of physical scales for each redshift bin, we take the following approach: for each photometric-spectroscopic pair, we assume that the photometric object is at the same redshift as the spectroscopic object, allowing us to convert from angle θ to projected distance $r_p = \chi(z_{\rm i})\theta$. Thus, we obtain an r_p-binned $w_{\rm ps}$ measurement. Then, in our equations, we perform a change of variables from θ to r_p:

$$\bar{w}_{\rm ps}(z_{\rm i}) = \int_{r_{\rm p,min}}^{r_{\rm p,max}} dr_{\rm p} \; \frac{1}{r_{\rm p}} w_{\rm ps}(r_{\rm p}, z_{\rm i}) \tag{4.14}$$

$$\bar{I}(z_{\rm i}) = \int_{r_{p,\rm min}}^{r_{\rm p,max}} dr_{\rm p} \; \frac{1}{r_{\rm p}} \int_{\chi_{\rm min}}^{\chi_{\rm max}} d\chi \; \xi_{\rm mm}\left(\sqrt{r_{\rm p}^2 + (\chi - \chi_{\rm i})^2}, z_{\rm i}\right) \tag{4.15}$$

Note that in this section we have implicitly assumed scale-independent biases. In Appendix A, we explore how scale-dependent bias can make the shape of the estimated redshift distribution sensitive to the choice of $\theta_{\rm min}$, $\theta_{\rm max}$.

Measurement

We use three well-defined spectroscopic samples that overlap significantly with our LRG sample and span its full redshift range (see Figure 4.4): CMASS galaxies from Data Release 12 of the Baryon Oscillation Spectroscopic Survey (BOSS; Eisenstein et al. 2011, Dawson et al. 2013a); galaxies from the the final data release of the VIMOS Public Extragalactic Redshift Survey (VIPERS; Scodeggio et al. 2018); and the main sample of quasars (QSOs) from Data Release 14 of eBOSS (Dawson et al. 2016) in the South Galactic Cap. We assume passive bias evolution for the CMASS and VIPERS galaxies, based on previous

clustering studies of these samples (e.g. Rodríguez-Torres et al. 2016 and Laurent et al. 2017, respectively) and for the eBOSS QSOs, we assume the functional fit to $b(z)$ published in Marulli et al. 2013 (and further validated using finer redshift bins in Krolewski et al. 2019).

To measure the angular cross-correlation $w_{\rm ps}(\theta, z_{\rm i})$ between photometric sources and spectroscopic sources, with the latter first divided into narrow redshift bins $z_{\rm i} \pm \delta z_{\rm i}$, we use the Landy-Szalay pair-count estimator (Landy & Szalay, 1993),

$$\hat{w}_{LS}(\theta) = \frac{D_1 D_2 - D_1 R_2 - D_2 R_1 + R_1 R_2}{R_1 R_2} \tag{4.16}$$

where DD, DR, and RR are the counts of data-data, data-random, and random-random pairs at average separation θ, within annular bins $\theta \pm \delta\theta$. We use 16 logarithmically spaced angular bins from $\theta = 0.001^\circ$ to $\theta = 1^\circ$. For each redshift bin, we convert the angular bins into bins of projected distance r_p using the mean redshift of the bin. If we make the modest approximation that every photometric object is at the same redshift as the spectroscopic object it is being correlated with, we can obtain the angular correlation function binned in r_p rather than θ, $w_{\rm ps}(r_p, z_{\rm i})$.

We estimate the errors on $w_{\rm ps}$ using bootstrapping (Efron, 1979). Rather than resampling on individual objects, which has been shown to lead to unreliable errors (Mo et al. 1992, Fisher et al. 1994), we partition the sky into equal area sub-regions, using the `HEALPix` scheme with coarse resolution $N_{\rm SIDE} = 4$. We discard any sub-regions that are fully disjoint from either the photometric or spectroscopic survey, then randomly select (with replacement) from the remaining sub-regions until the number of randoms in each bootstrap realization is similar to the total number of randoms in the overlapping part of the footprint[9]. The mean and variance are estimated from 500 bootstrap realizations, and are found to be highly robust to increasing or decreasing the number of bootstrap realizations.

As Table 4.2 and Figure 4.4 show, the three spectroscopic catalogs vary widely in their available overlapping area, their number density, and the widths of their redshift distributions. In order to maximize the signal-to-noise of each cross-correlation, the hyper parameters are adjusted individually. For instance, since VIPERS is made up of two very small windows, we must use a higher resolution of $N_{\rm SIDE} = 16$ to create the sub-regions for bootstrapping. The greatest signal-to-noise is achieved from the cross-correlation with the CMASS sample, whose large overlapping area and high number density near the peak of the LRG distribution allows us to use finer redshift bins of $\delta z = 0.05$ compared to $\delta z = 0.1$ used for the other two samples.

Results

Following Equation 4.3, we obtain an estimate for $dN_{\rm p}/dz$ from each cross-correlation. Bootstrap errors from $w_{\rm ps}$ are propagated to $\phi(z)$ by performing the full calculation, including

[9]Since the randoms are uniformly distributed and massively oversampled, the number of randoms can be treated as as a proxy for the effective area.

Spectroscopic Catalog	CMASS	VIPERS	eBOSS QSO
Overlapping Area (deg^2)	∼7461	∼23.5	∼940
Overlapping Number	615,056	68,022	19,266
Redshift Bin Size Used	0.05	0.1	0.1
N_{SIDE} Resolution Used	4	16	4
# Bootstrap Ensembles	500	500	500
$r_{\mathrm{p,min}}$, $r_{\mathrm{p,max}}$ (h^{-1} Mpc)	0.5, 5	0.005, 1	0.5, 5

Table 4.2: Summary of the external spectroscopic catalogs and the parameters of the cross-correlation analysis. "Overlapping Area" is the approximate intersection of the spectroscopic and DESI-DECaLS DR8 footprints. "Overlapping Number" is the number of spectroscopic objects falling within this overlap with redshifts in the range $0.1 < z < 1.2$ (see Figure 4.4 for a visualization of the overlap in redshift distributions). For bootstrapping, we reject any pixels lying entirely outside either survey; the remaining sub-regions are sampled with replacement to create the bootstrap ensembles.

normalization, with each bootstrap separately, and then determining the standard deviation in $\phi(z)$. We use a cubic B-spline to fit the combined results, where each value ϕ_i is weighed by the inverse of its standard deviation, $w_i = 1/\sigma_i$. A common rule of thumb recommends using a value of the smoothness parameter s in the range $m \pm \sqrt{2m}$ where m is the number of data points being fit; based on this, we choose a value of $s = 41$, which results in 6 interior knots. In order the respect the physicality of $\phi(z) \geq 0$ for all z, we force any negative spline coefficients to be zero. The clustering-based $\phi(z)$ points and fit are shown in Figure 4.5, along with the photo-z derived $\phi(z)$. Unsurprisingly, the spline fit is dominated by the CMASS cross-correlations (highlighted in blue in the figure) due to the comparatively high signal-to-noise of these cross-correlations. The photo-z and clustering redshift distributions are qualitatively similar but not identical, with the clustering $\phi(z)$ having a sharper peak.

4.4 Measuring Angular Power Spectra

Angular power spectra in the Limber approximation

Galaxy overdensity δ_g and CMB lensing convergence κ are both projections of 3D density fields, expressed as line-of-sight integrals over their respective projection kernels. The angular

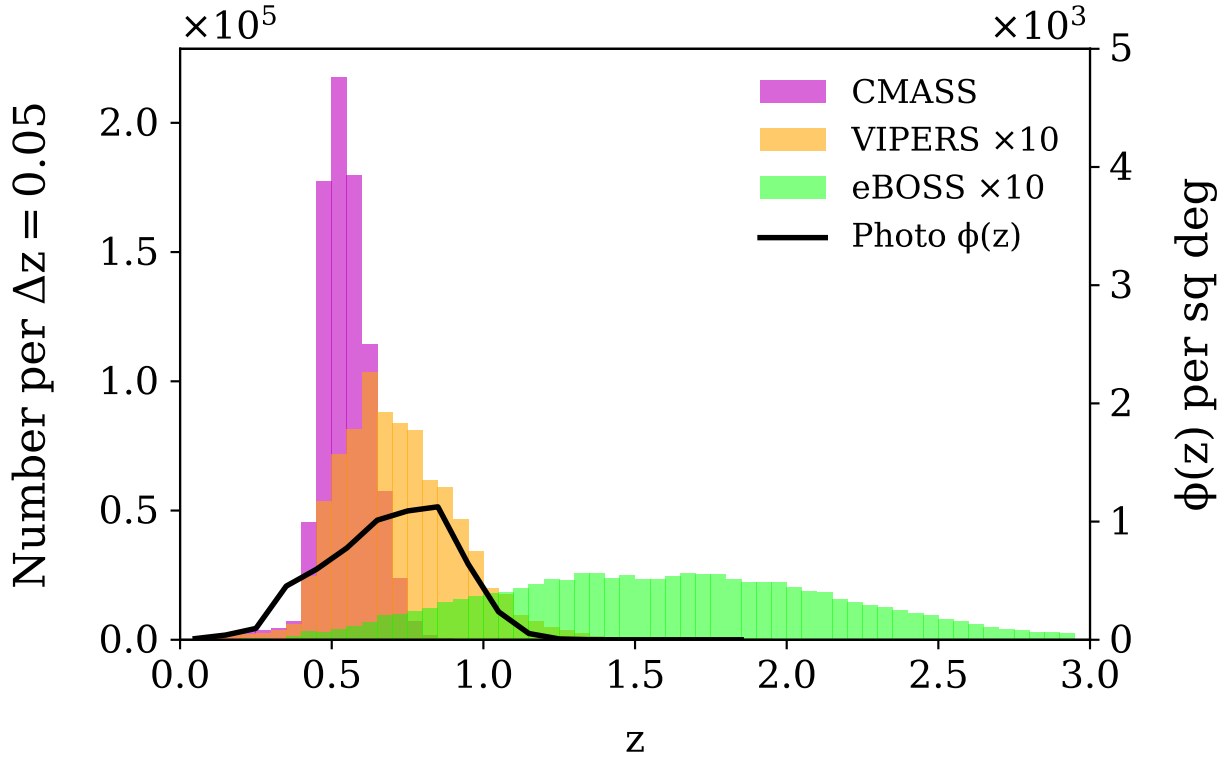

Figure 4.4: Visualizing how the redshifts of the external spectroscopic catalogs (histograms) overlap with the redshift distribution of DESI LRGs selected from DECaLS, as estimated using photometric redshifts (solid line).

cross-spectrum between two such fields X and Y is given by

$$C_\ell^{XY} = \int d\chi_1 \int d\chi_2 \; W^X(\chi_1) \; W^Y(\chi_2) \\ \int \frac{2}{\pi} k^2 dk \; P_{XY}(k; z_1, z_2) \; j_\ell(k\chi_1) \; j_\ell(k\chi_2) \tag{4.17}$$

where W^X and W^Y are the projection kernels, P_{XY} is the real-space power cross-spectrum, and j_ℓ are spherical Bessel functions of the first kind. As we are primarily interested in angular scales $\lesssim 1^\circ$ ($\ell \gtrsim 100$), we can adopt the Limber approximation (Limber, 1953; Rubin, 1954) and its first order correction (Loverde & Afshordi, 2008), under which the k integral evaluates to

$$P_{XY}\left(k = \frac{\ell + 1/2}{\chi_1}; z\right) \frac{1}{\chi_1^2} \delta^D(\chi_1 - \chi_2) \tag{4.18}$$

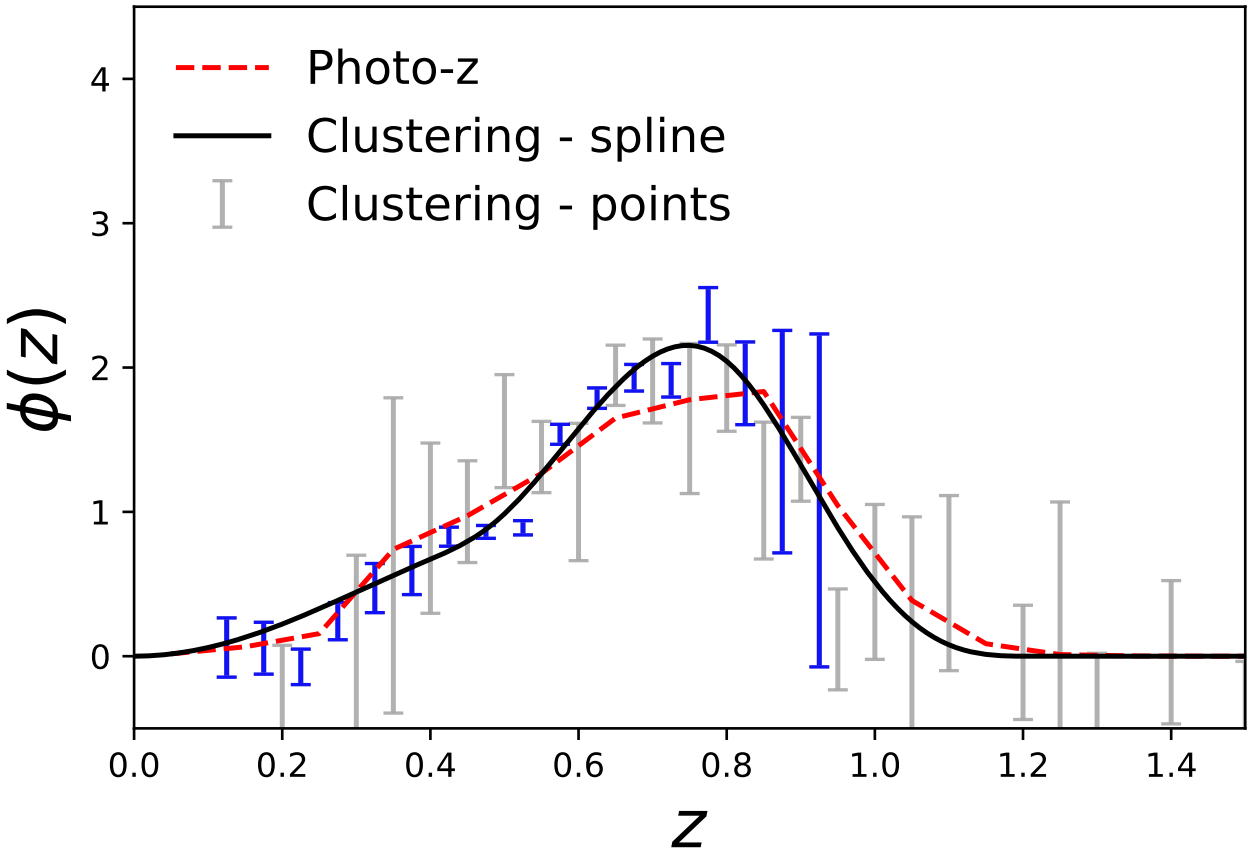

Figure 4.5: The normalized redshift distribution derived from cross-correlations with external spectroscopy (gray error bars) and resulting cubic B-spline fit (black solid line). The normalized redshift distribution derived from photo-z's is shown for comparison (red dashed line). The spline fit is dominated by the cross-correlation with CMASS galaxies (blue highlight).

Hence the angular cross-spectrum may be expressed as a single integral over line-of-sight co-moving distance,

$$C_\ell^{XY} = \int d\chi\ W^X(\chi) W^Y(\chi) \frac{1}{\chi^2} P_{XY}\left(k = \frac{\ell + 1/2}{\chi}; z\right) \tag{4.19}$$

$$= \int dz\ \frac{H(z)}{c} W^X(z) W^Y(z) \frac{1}{\chi^2} P_{XY}\left(k = \frac{\ell + 1/2}{\chi}; z\right) \tag{4.20}$$

The projection kernels for galaxy overdensity and CMB lensing convergence are, respectively,

$$\begin{aligned} W^g(z) &= \phi(z) = \frac{c}{H(z)}\phi(\chi) = \frac{c}{H(z)} W^g(\chi) \\ W^\kappa(z) &= \frac{3}{2c}\Omega_{m0}\frac{H_0^2}{H(z)}(1+z)\frac{\chi(\chi_* - \chi)}{\chi_*} = \frac{c}{H(z)} W^\kappa(\chi) \end{aligned} \tag{4.21}$$

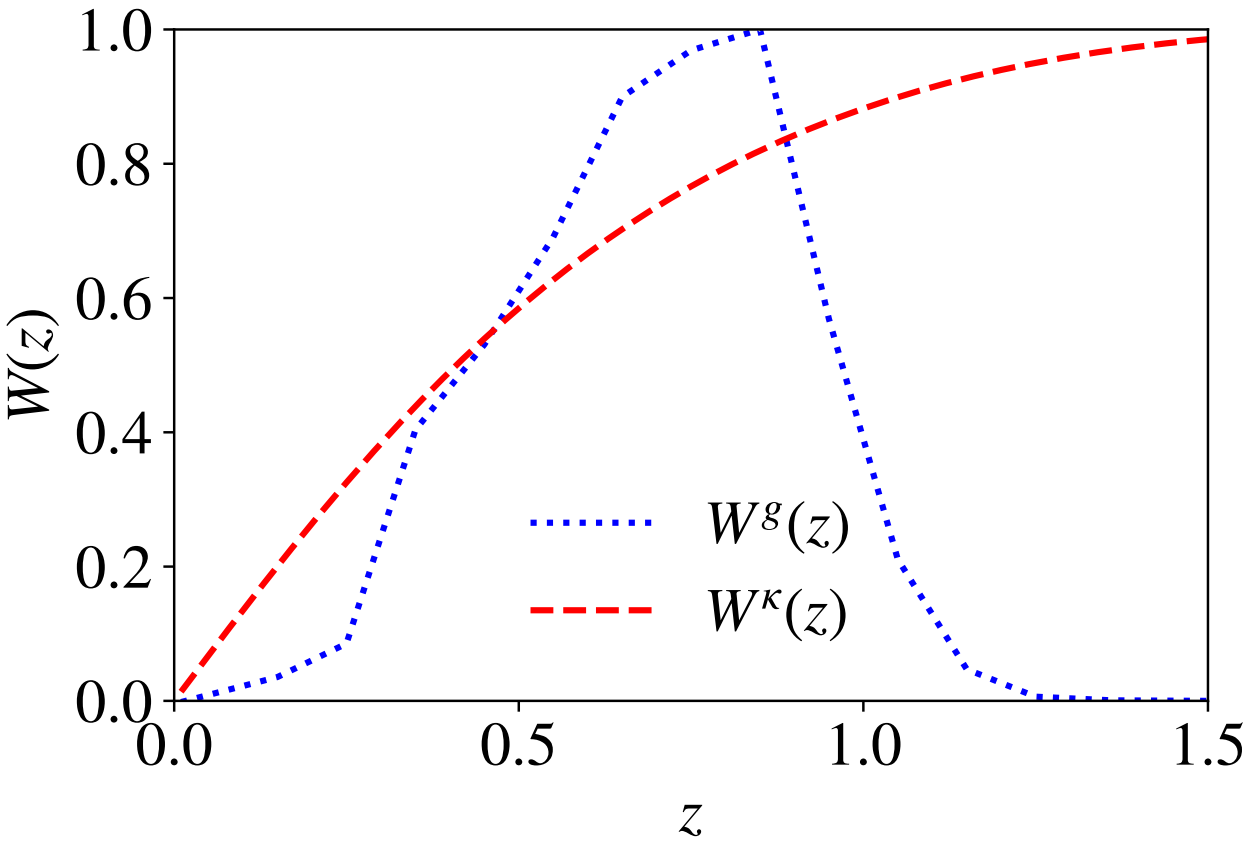

Figure 4.6: Projection kernels for the galaxy sample (dashed blue line) and CMB lensing (dotted red line), both normalized to a unit maximum.

where $\chi_* = \chi(z_*{\approx}1100) \approx 9400\ h^{-1}$Mpc is the distance to the surface of last scattering, and $\phi(z)$ is the normalized redshift distribution of the galaxy sample. These kernels are plotted in Figure 4.6.

Plugging in and simplifying the expressions for the spectra,

$$
\begin{aligned}
C_\ell^{\kappa g} &= \int d\chi \; \frac{3\Omega_{m0}H_0^2}{2c^2}\frac{1+z}{\chi^2}\frac{\chi(\chi_*-\chi)}{\chi_*}\phi(\chi)P_{mg}\Big(k=\frac{\ell+1/2}{\chi};z\Big) \\
&= \int dz \; \frac{3\Omega_{m0}H_0^2}{2cH(z)}\frac{1+z}{\chi^2}\frac{\chi(\chi_*-\chi)}{\chi_*}\phi(z)P_{mg}\Big(k=\frac{\ell+1/2}{\chi};z\Big) \\
C_\ell^{gg} &= \int d\chi \; \phi(\chi)^2\frac{1}{\chi^2}P_{gg}\Big(k=\frac{\ell+1/2}{\chi};z\Big) \\
&= \int dz \; \frac{H(z)}{c}\phi(z)^2\frac{1}{\chi^2}P_{gg}\Big(k=\frac{\ell+1/2}{\chi};z\Big) \\
C_\ell^{\kappa\kappa} &= \int d\chi \; \Big(\frac{3\Omega_{m0}H_0^2}{2c^2}\frac{1+z}{\chi^2}\frac{\chi(\chi_*-\chi)}{\chi_*}\Big)^2 P_{mm}\Big(k=\frac{\ell+1/2}{\chi};z\Big) \\
&= \int dz \; \frac{H(z)}{c}\Big(\frac{3\Omega_{m0}H_0^2}{2cH(z)}\frac{1+z}{\chi^2}\frac{\chi(\chi_*-\chi)}{\chi_*}\Big)^2 P_{mm}\Big(k=\frac{\ell+1/2}{\chi};z\Big)
\end{aligned}
\tag{4.22}
$$

Estimating angular power spectra

Many different approaches for estimating angular power spectra from cosmological maps exist in the literature, including maximum likelihood estimators (Bond et al. 1998, Wandelt & Hansen 2003), the optimal quadratic estimator (Tegmark 1997, Tegmark & de Oliveira-Costa 2001), and Bayesian sampling techniques (e.g. Eriksen et al. 2004, Taylor et al. 2008). While these methods have the advantage of recovering the unbiased power spectrum directly, they are computationally expensive to implement, particularly for the high resolution maps produced by modern experiments, since they scale as $\mathcal{O}(\ell_{\rm max}^6)$. Sub-optimal but numerically efficient pseudo-C_ℓ algorithms (Hivon et al., 2002) are a popular alternative when dealing with multipoles $\ell > 30$ (Efstathiou, 2004a), as they take advantage of speedy spherical harmonics transforms to recover the power spectrum in $\mathcal{O}(\ell_{\rm max}^3)$ time. Below, we briefly outline the pseudo-C_ℓ approach.

Any function $T(\hat{n})$ defined on a sphere may be expanded into spherical harmonics $Y_{\ell m}$ with expansion coefficients $a_{\ell m}$ as

$$T(\hat{n}) = \sum_{\ell=0}^{\infty}\sum_{m=-\ell}^{\ell} a_{\ell m}Y_{\ell m}(\hat{n}) \tag{4.23}$$

$$a_{\ell m} = \int_{4\pi} d\Omega \; T(\hat{n}) \; Y^*_{\ell m}(\hat{n}) \tag{4.24}$$

The angular power spectrum C_ℓ measures the amplitude as a function of wavelength averaged over direction,

$$C_\ell = \frac{1}{2\ell+1}\sum_{m=-\ell}^{\ell}|a_{\ell m}|^2 \tag{4.25}$$

This is the observed angular power spectrum of a given Gaussian realization; the average over an ensemble of Universes, $\langle C_\ell \rangle \equiv C_\ell^{\rm th}$, is specified by the physics (primordial perturbations, galaxy formation, etc.) with uncertainty due to cosmic variance given by

$$\sigma_\ell^2 = \frac{C_\ell^{\rm XX} C_\ell^{\rm YY} + (C_\ell^{\rm XY})^2}{2\ell + 1} \tag{4.26}$$

However, in practice, we are not dealing with measurements over the full sky, but rather a masked and weighted partial sky. We must account for the effect of the masking window function $W(\hat{n})$, which couples different ℓ modes and biases the estimator. Naive calculation of the spherical harmonics transform on a partial sky map produces the pseudo angular power spectrum, whose coefficients are a convolution of the mask and the true coefficients,

$$\tilde{C}_\ell = \frac{1}{2\ell + 1} \sum_{m=-\ell}^{\ell} |\tilde{a}_{\ell m}|^2 \tag{4.27}$$

$$\tilde{a}_{\ell m} = \int_{4\pi} d\Omega \; T(\hat{n}) \; W(\hat{n}) \; Y^*_{\ell m}(\hat{n}) \tag{4.28}$$

Fortunately, their ensemble averages are related simply as

$$\langle \tilde{C}_\ell \rangle = \sum_{\ell'=0}^{\infty} M_{\ell\ell'} \langle C_{\ell'} \rangle \tag{4.29}$$

where the mode-mode coupling matrix M can be determined purely from the geometry of the mask. This ℓ-by-ℓ matrix is generally singular in the case of large sky cuts. In order to perform matrix inversion, a common method is to use a set of discrete bandpower bins L and assume the angular power spectrum is a step-wise function in each bin. Using this approach, the MASTER algorithm (Hivon et al., 2002) is able to efficiently calculate and invert the L-by-L mode-mode coupling matrix to extract the binned angular power spectrum from the binned pseudo angular power spectrum,

$$\langle C_L \rangle = \sum_{L'} M^{-1}_{LL'} \langle \tilde{C}_{L'} \rangle \tag{4.30}$$

We use the implementation `NaMaster` (Alonso et al., 2019) to calculate the mode-mode coupling matrix and decoupled angular power spectra in bandpower bins. Multipole resolution is limited by $\Delta\ell \approx 180°/\phi$, where ϕ is the smallest dimension of the angular patch, and the minimum multipole that can be meaningfully constrained is the wavelength corresponding to this angular scale (Peebles, 1980). Since the angular power of the mask is concentrated at large modes, dropping to below 10% power at $\ell \sim 20$, we choose a conservative binning scheme with linearly spaced bins of size $\Delta\ell = 20$ from $\ell_{\rm min} = 30$ to $\ell_{\rm max} = 1500$. However, following the approach of Krolewski et al. (2019), we run `NaMaster` out to larger $\ell_{\rm max}$ to avoid power leakage near the edge of the measured range.

Evaluating the observational results requires consistent application of the same binning scheme to the theory curves. Since the theory curves are not necessarily piecewise constant, they must first be convolved with the mode-mode coupling matrix $M_{\ell\ell'}$, then binned into the appropriate bandpowers, and then finally decoupled.

Additionally, the observed auto-spectra will be a combination of signal plus noise,

$$C_L^{gg} = S_L^{gg} + N_L^{gg} \tag{4.31}$$
$$C_L^{\kappa\kappa} = S_L^{\kappa\kappa} + N_L^{\kappa\kappa} \tag{4.32}$$

Here, N^{gg} is the shot noise of the galaxy field, $1/\bar{n}$ (where $\bar{n}$ is the mean number of galaxies per square steradian), while an estimate of the lensing noise $N_\ell^{\kappa\kappa}$ due to e.g. instrumental and atmospheric effects is provided by the Planck collaboration and binned into bandpowers using the method discussed above. In subsequent analysis, we have subtracted the noise terms from the observed auto-spectra, as well as dividing out the appropriate pixel window functions.

Estimating covariance matrices

The Gaussian or "disconnected" part of the covariance matrix, i.e. the covariance for perfectly Gaussian fields, dominates the total covariance matrix on linear and weakly nonlinear scales. While trivial to compute for full-sky fields, the exact correlations between different modes induced by a partial sky are computationally expensive to calculate, requiring $\mathcal{O}(\ell_{\rm max}^6)$ operations (Efstathiou 2004b, García-García et al. 2019). A common approximation assumes that the off-diagonal elements remain negligible after mode coupling and simply modifies the diagonal elements by rescaling the number of degrees of freedom,

$$\Sigma_{\ell\ell'}^{\rm XY} = (\sigma_\ell^{\rm XY})^2 \delta_{\ell\ell'} \tag{4.33}$$
$$(\sigma_\ell^{\rm XY})^2 = \frac{[(C_\ell^{\rm XX} + N_\ell^{\rm XX})(C_\ell^{\rm YY} + N_\ell^{\rm YY}) + (C_\ell^{\rm XY} + N_\ell^{\rm XY})^2]_{\rm th}}{f_{\rm sky}(2\ell+1)} \frac{w_4}{w_2^2}$$

where $f_{\rm sky}$ is the fraction of the sky masked,

$$f_{\rm sky} = \int_{4\pi} d\Omega\ W(\hat{n}) \tag{4.34}$$

and w_i is related to the ith moment as

$$w_i = \frac{1}{f_{\rm sky}} \int_{4\pi} d\Omega\ W^i(\hat{n}) \tag{4.35}$$

The factor $f_{\rm sky} w_2^2 / w_4$ accounts for the loss of modes induced by masking. This analytic expression has been shown to reproduce errors that are nearly identical to those obtained from Monte Carlo simulations (Hivon et al., 2002).

We average over the bandpower bins with the inverse weighting

$$\frac{1}{(\sigma_L^{\mathrm{XY}})^2} = \frac{1}{\Delta\ell}\sum_{\ell\in L}\frac{1}{(\sigma_\ell^{\mathrm{XY}})^2} \tag{4.36}$$

where $\Delta\ell$ is the width of the bandpower bin.

Pixelised maps and masks

To create our galaxy density map, we pixelise the sky using the `HEALPix` scheme with resolution $N_{\mathrm{SIDE}} = 512$, corresponding to a pixel area of approximately 0.013 square degrees. This resolution was chosen to avoid the shot noise limit in which most pixels contain zero or one galaxies (for our sample with mean density ≈ 610 per square degree, it produces an average of 5-10 galaxies per pixel), while still probing the scales of interest, $\ell_{\mathrm{max}} \sim 3 \times N_{\mathrm{SIDE}} \approx 1500$. Using galaxy and random catalogs with the masks of Section 4.2 applied to both, we calculate the density contrast $\delta = n/\bar{n} - 1$ within each pixel. Under the `HEALPix` scheme, pixels have identical areas; however, the effective area of some pixels may be less than this if they straddle the irregular shape of the footprint boundary or overlap with masked regions around bright stars, large galaxies, etc. Since our masks are applied to both the galaxy and random catalogs in a consistent manner, we can use the random catalog to estimate the effective area of each pixel, and thus calculate accurate mean galaxy densities even in pixels that are partially masked.

To construct the pixelised galaxy mask, we measure where the distribution of effective areas deviates from a Poisson distribution, since the effective areas are estimated directly from the number of randoms per pixel, which is a Poisson process. We determine a cutoff of $a_{\mathrm{eff}}/a_{\mathrm{tot}} = 0.5$, and confirm that the pixels below this cutoff lie mainly along footprint boundary, as shown in Figure 4.7. Here, the effective area is calculated by using the random catalog *pre*-masking, hence why the distribution is centered at $a_{\mathrm{eff}}/a_{\mathrm{tot}} \approx 1$. The equivalent distribution calculated using masked randoms results in a slightly lower mean $\tilde{a}_{\mathrm{eff}}/a_{\mathrm{tot}} \approx 0.95$ (matching the masked sky fraction of Table 4.1) and an enhanced left tail since a substantial fraction of pixels are now partially masked. However, we do not necessarily need to discard these partially masked pixels as long as we are able to accurately estimate the density within them, since the pixelisation smooths the density on scales smaller than the pixel size. Hence, for our binary pixel mask, we use the cutoff calculated using the unmasked randoms, with the mask set to 1 for $a_{\mathrm{eff}}/a_{\mathrm{tot}} > 0.5$ and 0 otherwise.

The galaxy density map and mask are then upgraded to $N_{\mathrm{SIDE}} = 2048$ to match the resolution of the Planck CMB lensing map and mask, and converted from equatorial to galactic coordinates. To improve the stability of the matrix inversion, the Planck mask is apodized using a 1° FWHM Gaussian. The resulting masked galaxy density and CMB lensing convergence maps are shown in Figure 4.8.

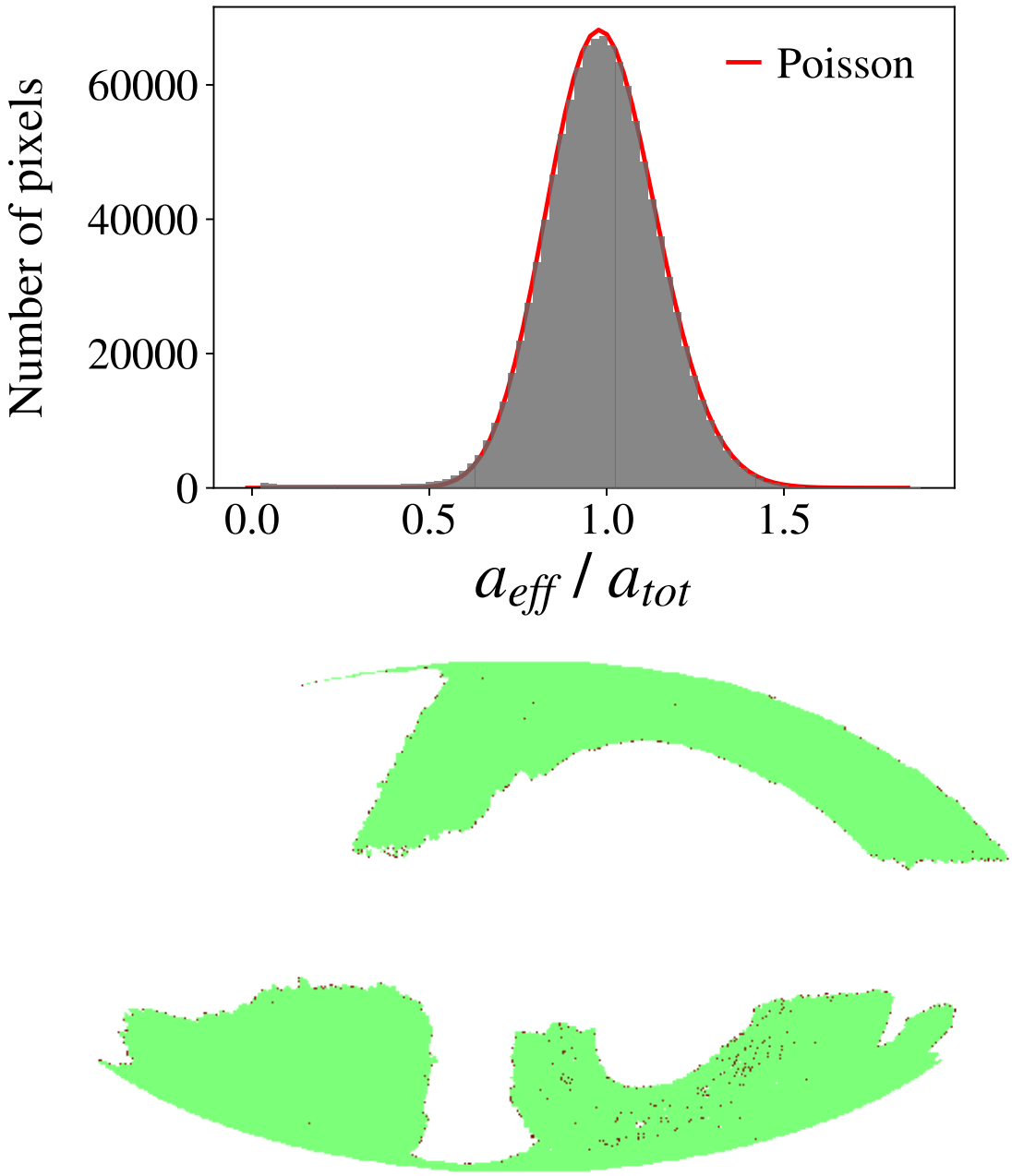

Figure 4.7: Upper: Histogram of the effective areas of pixels created with `HEALPix` resolution $N_{\rm SIDE} = 512$, showing a slight deviation from a Poisson distribution at the low end due to pixels straddling the footprint boundary or holes from the galaxy mask. Lower: Pixels selected as $a_{\rm eff}/a_{\rm tot} < 0.5$ lie predominately on the edges of the footprint.

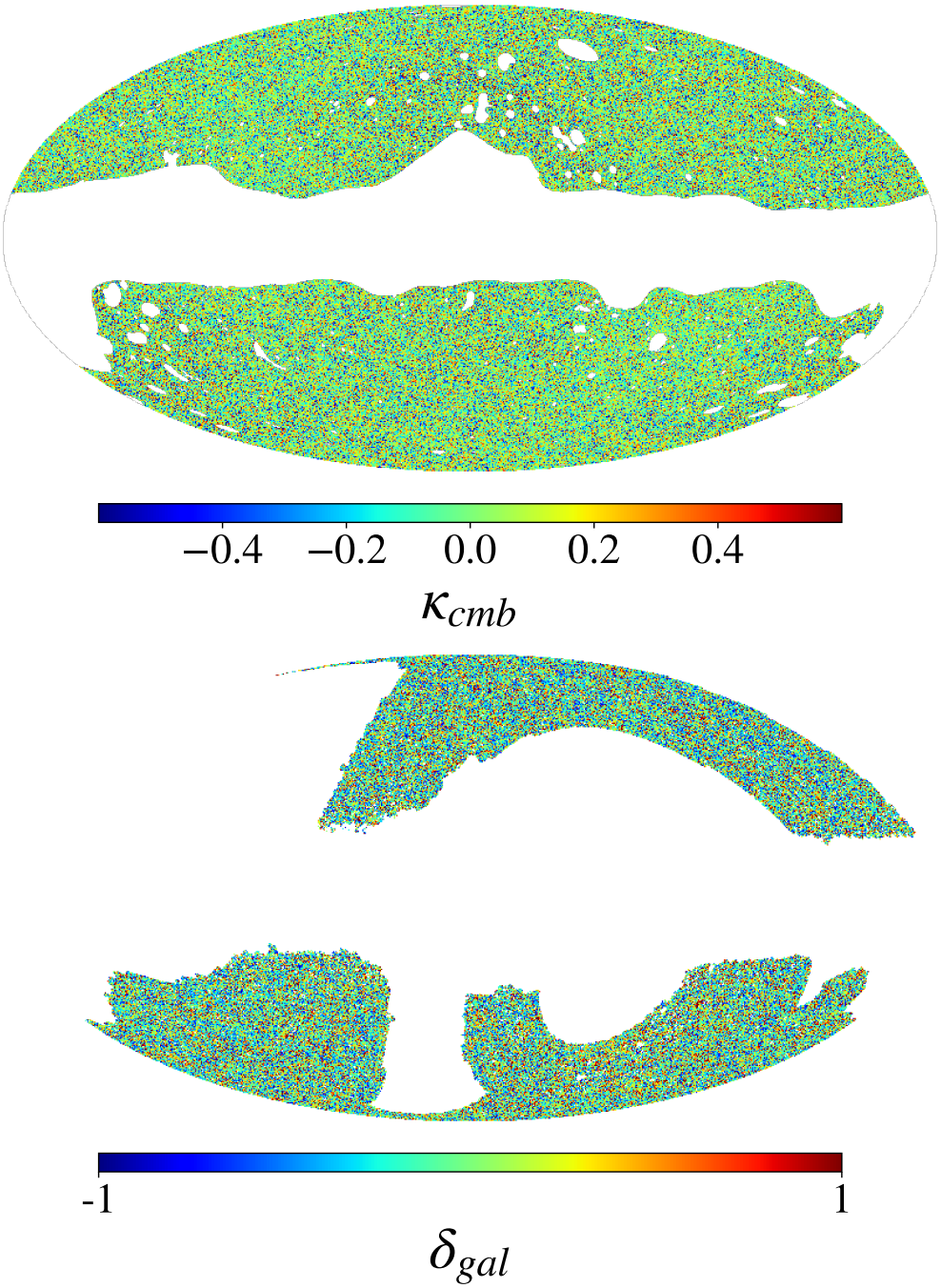

Figure 4.8: Maps of Planck `BASE` CMB lensing convergence (upper) and DESI LRG galaxy overdensity (lower) in galactic coordinates. Uses `HEALPix` scheme with resolution $N_{\mathrm{SIDE}} = 2048$, Mollweide projection, and the astronomy convention (east towards left). Both maps are multiplied by their corresponding masks. The CMB lensing convergence is additionally smoothed on a scale of 10 arcmin for visual clarity.

4.5 Magnification Bias

Magnification bias is a well-known weak lensing effect (for a review of weak lensing, we refer the reader to Bartelmann & Schneider 2001) that modulates the number density of galaxies in a flux-limited survey. When distant galaxies are magnified by gravitational lenses along the line-of-sight, their observed number per unit area is decreased due to the apparent stretching of space between and around them. At the same time, there is a corresponding increase in their observed brightness; as a consequence, the lensed galaxies are drawn from a fainter source population than the unlensed galaxies, leading to an increase in the number count as galaxies that would normally fall below the limiting magnitude of the survey become detectable with magnification. Through these two competing effects, magnification induces correlations between the galaxies and intervening matter in their foreground, and thus can bias the galaxy-galaxy and galaxy-convergence angular power spectra (see e.g. LoVerde et al. 2008, Ziour & Hui 2008, and references contained therein).

In practice, the magnification bias introduces an additional term in the galaxy window function,

$$W^g(z) \to W^g(z) + W^\mu(z) \tag{4.37}$$

which, to first order, is given by

$$W^\mu(z) = (5s-2)\frac{3}{2c}\Omega_{m0}\frac{H_0^2}{H(z)}(1+z)\int_z^{z^*} dz' g(z') \tag{4.38}$$

$$g(z') = \frac{\chi(z)(\chi(z')-\chi(z))}{\chi(z')}\phi(z') \tag{4.39}$$

where s is the slope of the cumulative magnitude function, i.e. the response of the number density of the sample to a multiplicative change in brightness at the limiting magnitude of the survey,

$$s = \frac{d\log_{10} n(m < m_{\rm lim})}{dm}|_{m=m_{\rm lim}} \tag{4.40}$$

This W^μ term in the galaxy window function leads to additional terms in the galaxy-convergence and galaxy-galaxy angular power spectra,

$$C_\ell^{\kappa g} \to C_\ell^{\kappa g} + C_\ell^{\kappa\mu} \tag{4.41}$$

$$C_\ell^{gg} \to C_\ell^{gg} + 2C_\ell^{g\mu} + C_\ell^{\mu\mu} \tag{4.42}$$

We calculate s by perturbing the observed optical and infrared magnitudes of the imaged objects by a small differential in each direction $\Delta m = \pm 0.01$, then reapplying target selection (as defined in Section 4.2) and measuring the corresponding shifts in the number density of the new LRG samples. Using the finite difference method, we determine $s = 0.999 \pm 0.015$, with the error computed as $\Delta s = (\log_{10}(N) - \log_{10}(N - \sqrt{N}))/\Delta m$.

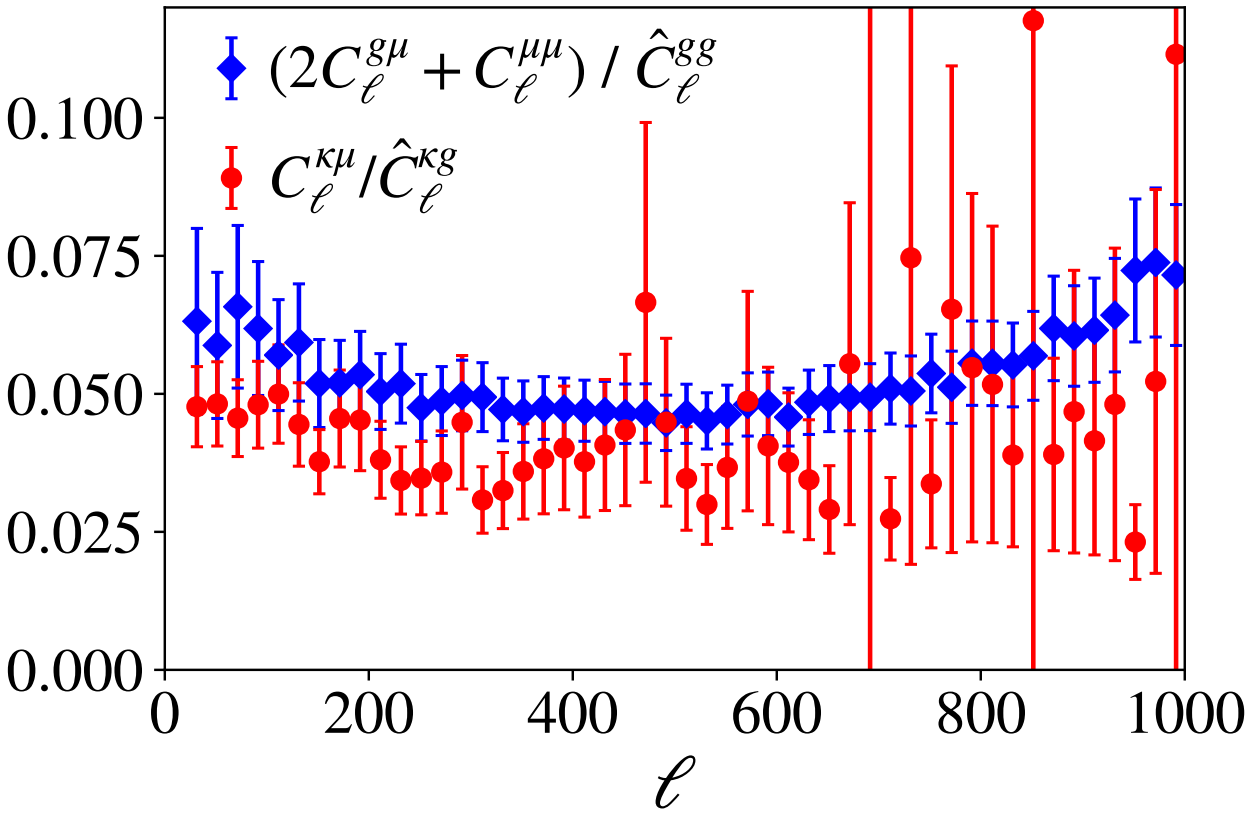

Figure 4.9: The magnification bias terms of Equations 4.41 and 4.42 as a fraction of the total observed (after subtracting shot noise, in the galaxy-galaxy case) spectra, i.e. before correcting for magnification bias. The error bars represent error on the fraction and are dominated by the errors of the denominator.

We plot the magnification bias corrections as a fraction of the observed spectra (after noise subtraction) in Figure 4.9. The corrections to the galaxy-galaxy spectrum are at a level of approximately 5% over most of the range of scales considered, with 1-2% increases at edges of the range $\ell < 100$ and $\ell > 900$, while the correction to the cross-spectrum is flat within error bars[10] at 4-5%. Though the DESI LRG redshift distribution is relatively narrow and peaks at $z < 1$, the high number density and low clustering bias coupled with a steep faint end slope contribute to effects at the level of a few percent, as Figure 4.9 shows.

4.6 Results

A cross-correlation measurement between DESI-like LRGs selected from DECaLS imaging and CMB lensing from Planck 2018 is detected at a significance of S/N = 27.2 over the range of scales $\ell_{\rm min} = 30$ to $\ell_{\rm max} = 1000$. In Figure 4.10, we plot per-multipole and cumulative

[10]These error bars are dominated by the errors in the cross-spectrum, which become significant at $\ell > 700$.

signal-to-noise ratios for both the galaxy-galaxy and galaxy-convergence spectra, where the signal-to-noise ratio of the XY angular power spectrum at multipole ℓ is given by

$$\left(\frac{S}{N}\right)(\ell) = \frac{C_\ell^{\mathrm{XY}}}{\sigma_\ell^{\mathrm{XY}}} \tag{4.43}$$

and the cumulative signal-to-noise ratio up to ℓ_{max} is

$$\left(\frac{S}{N}\right)(<\ell_{\mathrm{max}}) = \sqrt{\sum_{\ell'=L_{\mathrm{min}}}^{\ell_{\mathrm{max}}} \frac{(C_{\ell'}^{\mathrm{XY}})^2}{(\sigma_{\ell'}^{\mathrm{XY}})^2}} \tag{4.44}$$

The galaxy-galaxy S/N peaks at $\ell \sim 500$ whereas the galaxy-convergence generally decreases over the range of scales considered. We note that the theoretical galaxy-convergence S/N would be expected to peak at $\ell \sim 100$ and fall off at smaller ℓ; as this is within the regime at which both the pseudo-C_ℓ framework and the Limber approximation begin to break down, this feature is washed out in the observed S/N.

We also compare the cross-spectrum using the baseline MV CMB lensing map versus using the TT-only tSZ-deprojected map. The two curves are shown in the top panel of Figure 4.11, and clearly lie well within 1σ of one another. The fractional difference is shown in the lower panel. Since the error bars on the cross-spectra are generally large, they dominate the errors on the fraction, but as Figure 4.11 illustrates, the errors associated with tSZ are on the order of a few percent and very subdominant to the overall lensing noise.

In the following sub-sections, we present the angular power spectra and interpret them using two different models for the galaxy-galaxy and matter-galaxy 3D power spectra: the HaloFit dark matter power spectrum multiplied by a linear large-scale bias, and a convolutional Lagrangian effective field theory with Lagrangian bias. Additionally, we perform the fits using both photometric- and clustering-derived redshift distributions for the galaxy sample, which not only suggests an estimate of the error associated with uncertainty in the redshift distribution, but also allows us to evaluate the bias at an effective redshift $z \approx 0.68$ in both models and to test the assumption of passive bias evolution.

HaloFit Modeling

Within a framework for modeling the galaxy-galaxy and matter-galaxy power spectra $P_{\mathrm{gg}}(k)$, $P_{\mathrm{mg}}(k)$, the observed angular power spectra C_ℓ^{gg}, $C_\ell^{\kappa g}$ can constrain cosmological and galaxy bias parameters. A particularly simple and interpretable model is to use the HaloFit (Smith et al., 2003) fitting function for the nonlinear dark matter power spectrum, $P_{\mathrm{mm}}^{\mathrm{HF}}(k)$, and multiply by scale-independent linear biases to obtain the galaxy-galaxy and galaxy-matter power spectra,

$$P_{gg}(k,z) = b_{gg}(z)^2 P_{\mathrm{mm}}^{\mathrm{HF}}(k,z) \tag{4.45}$$

$$P_{\kappa g}(k,z) = b_{\kappa g}(z) P_{\mathrm{mm}}^{\mathrm{HF}}(k,z) \tag{4.46}$$

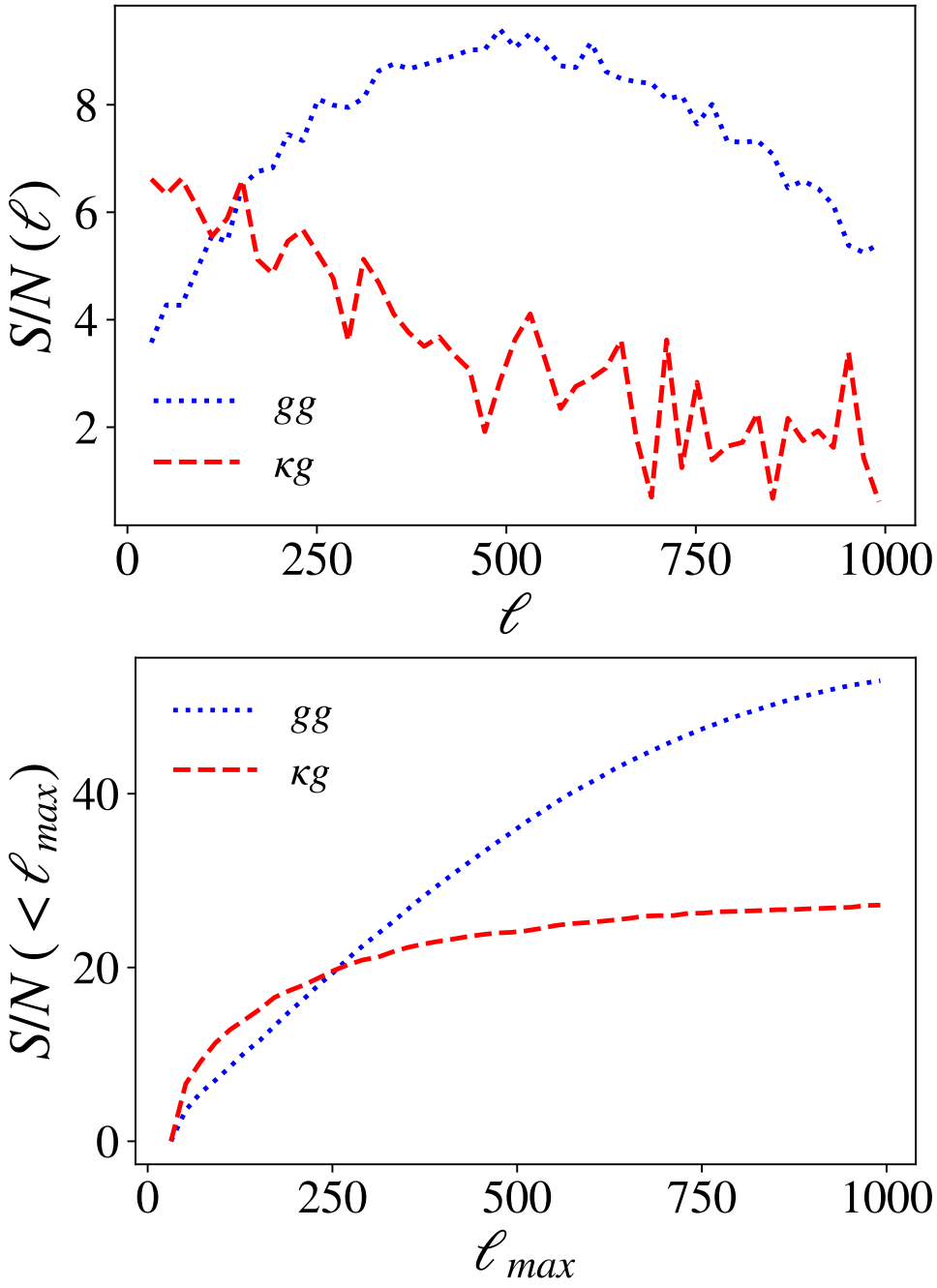

Figure 4.10: Per multipole (upper) and cumulative (lower) signal-to-noise ratio for the galaxy-galaxy (blue dotted line) and galaxy-convergence (red dashed line) angular power spectra measurements.

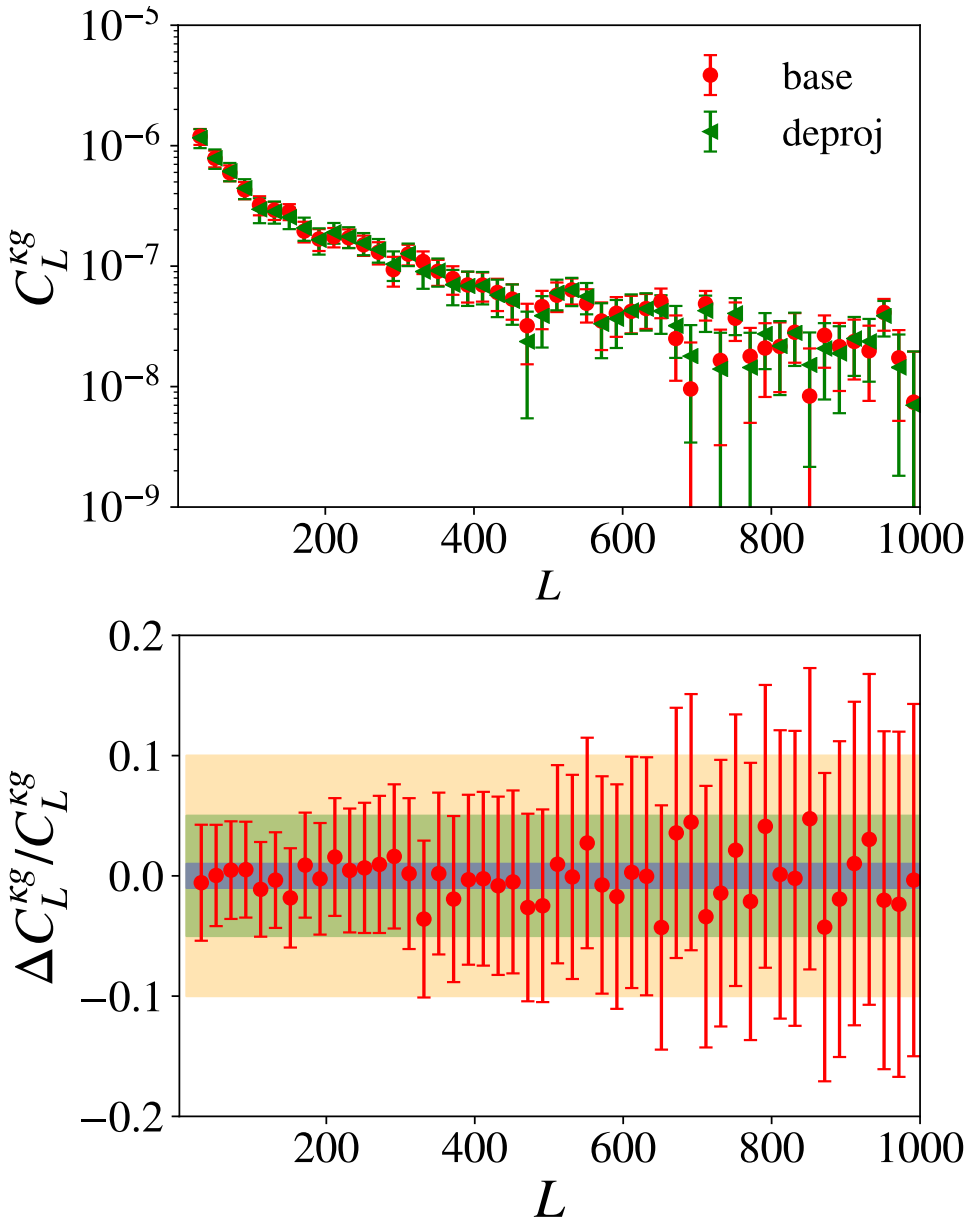

Figure 4.11: Upper: Comparison of observed cross-spectrum $C_L^{\kappa g}$ calculated from `BASE` (red circles) versus `DEPROJ` (green triangles) lensing maps. Lower: The difference between the two measurements as a fraction of the theoretical prediction, with three bands illustrating 1%, 5% and 10%.

HaloFit Model, Photo $\phi(z)$

$\ell_{\rm max}$	$b_{\rm gg}$	$\chi^2_{\rm gg}$/d.o.f.	$b_{\kappa \rm g}$	$\chi^2_{\kappa \rm g}$/d.o.f.
200	1.57 ± 0.05	0.7 / 8	1.27 ± 0.07	4.2 / 8
400	1.63 ± 0.03	3.4 / 18	1.32 ± 0.06	8.1 / 18
600	1.66 ± 0.02	8.4 / 28	1.32 ± 0.05	12.1 / 28
800	1.67 ± 0.02	9.9 / 38	1.32 ± 0.05	20.9 / 38
1000	1.64 ± 0.02	30.4 / 48	1.32 ± 0.05	26.8 / 48

Table 4.3: Fitting linear bias from the observed C_ℓ^{gg}, $C_\ell^{\kappa g}$ up to different $\ell_{\rm max}$ using the HaloFit model for the nonlinear dark matter power spectrum, photometric $\phi(z)$, and the assumption $b(z) \propto D(z)^{-1}$.

Differences between b_{gg} and $b_{\kappa g}$ are expected, due in large part to the stochastic contribution arising from the the fact that the galaxy field is a discrete sampling of the underlying dark matter distribution. As such, this stochastic component, which may include scale-dependent and non-Poissonian behavior, affects the galaxy-galaxy auto-spectrum and matter-galaxy cross-spectrum differently.

Using the Boltzmann code `CLASS` (Blas et al., 2011) to calculate the HaloFit dark matter power spectrum for the fiducial Planck 2018 cosmology, we take the photometric $\phi(z)$ and assume a bias evolution $b_{gg}(z), b_{\kappa g}(z) \propto D(z)^{-1}$. We then perform weighted least squares fits of the present day biases. The results are given in Table 4.3, with the fits repeated for $\ell_{\rm max} = 200, 400, 600, 800, 1000$. We find that the linear biases are unaffected by the choice of $\ell_{\rm max}$ and that the cross bias $b_{\kappa g}$ is consistently lower than the galaxy bias b_{gg}, with the latter agreeing well with DESI survey expectations and the findings of Kitanidis et al. 2019.

We then repeat the same measurement using the clustering-derived $\phi(z)$ discussed in Section 4.3, again finding that the choice of $\ell_{\rm max}$ has negligible impact. The results, given in Table 4.4, show that uncertainty in the redshift distribution causes a difference in the derived galaxy bias parameters of $\sigma_{b_{gg}} = 0.08$. By contrast, the cross bias is extremely stable with respect to changes in the redshift distribution, not changing at all when the redshift distribution is changed from the photometric estimate to the clustering estimate; this may be explained by the fact that the cross-spectrum only depends on one factor of $\phi(z)$ while the auto-spectrum requires $\phi(z)^2$.

Another advantage of using the clustering-based $\phi(z)$ is the ability to extract a galaxy redshift kernel with bias evolution baked in, rather than assuming a parametric form e.g. $b(z) \propto D(z)^{-1}$. As discussed in Section 4.3, this type of modeling allows us to constrain $b_{\rm eff} \approx b(z_{\rm eff})$ rather than the present day bias. We find the results, given in Table 4.5, to be in perfect agreement with the results of Table 4.4 under the assumption $b(z) \propto D(z)^{-1}$ used in the latter, giving for instance $b_{\rm gg} = 1.56 \pm 0.01$ and $b_{\kappa \rm g} = 1.31 \pm 0.05$ for the $\ell_{\rm max} = 1000$ case.

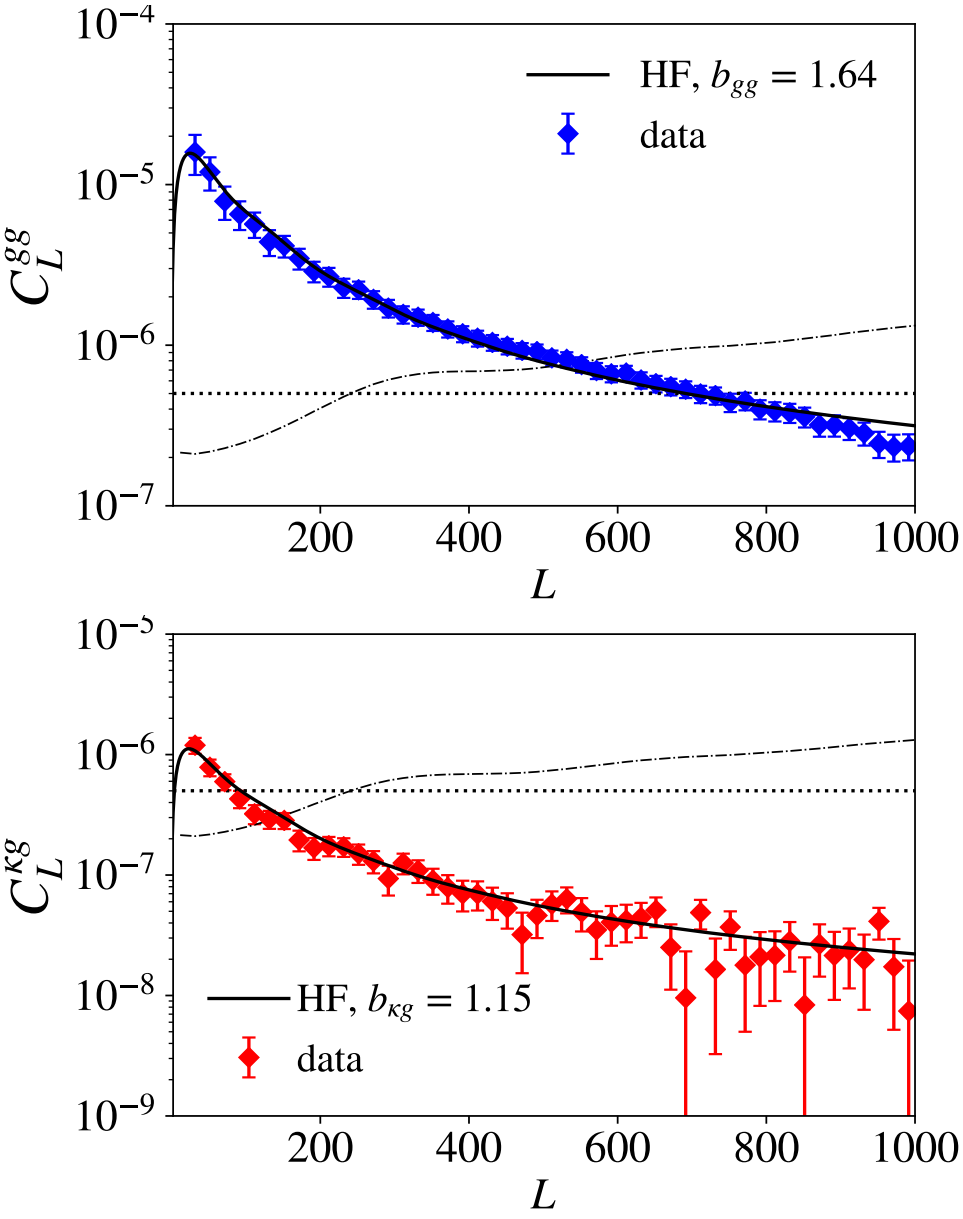

Figure 4.12: The observed galaxy-galaxy (upper plot, blue diamonds) and galaxy-convergence (lower plot, red diamonds) angular power spectra, after subtracting noise and correcting for magnification bias. Solid lines correspond to the the theoretical predictions using a HaloFit matter power spectrum and the best fit linear biases from Table 4.3. The dotted horizontal line is the galaxy shot noise floor, and the dashed black curve is the lensing noise.

HaloFit Model, Clustering $\phi(z)$

$\ell_{\rm max}$	$b_{\rm gg}$	$\chi^2_{\rm gg}$/d.o.f.	$b_{\kappa \rm g}$	$\chi^2_{\kappa \rm g}$/d.o.f.
200	1.50 ± 0.05	0.8 / 8	1.27 ± 0.07	4.0 / 8
400	1.55 ± 0.03	3.4 / 18	1.32 ± 0.06	8.0 / 18
600	1.59 ± 0.02	8.7 / 28	1.32 ± 0.05	11.9 / 28
800	1.59 ± 0.02	10.2 / 38	1.32 ± 0.05	20.8 / 38
1000	1.56 ± 0.01	29.9 / 48	1.32 ± 0.05	26.7 / 48

Table 4.4: Fitting linear bias from the observed C_ℓ^{gg}, $C_\ell^{\kappa g}$ up to different $\ell_{\rm max}$ using the HaloFit model for the nonlinear dark matter power spectrum, clustering $\phi(z)$, and the assumption $b(z) \propto D(z)^{-1}$.

HaloFit Model, Clustering $b(z)\phi(z)$

$\ell_{\rm max}$	$b^{\rm eff}_{\rm gg}$	$\chi^2_{\rm gg}$/d.o.f.	$b^{\rm eff}_{\kappa \rm g}$	$\chi^2_{\kappa \rm g}$/d.o.f.
200	2.14 ± 0.07	0.8 / 8	1.80 ± 0.10	4.0 / 8
400	2.21 ± 0.04	3.4 / 18	1.89 ± 0.08	8.0 / 18
600	2.26 ± 0.03	8.7 / 28	1.88 ± 0.08	12.0 / 28
800	2.27 ± 0.02	10.2 / 38	1.88 ± 0.07	20.8 / 38
1000	2.23 ± 0.02	29.9 / 48	1.88 ± 0.07	26.7 / 48

Table 4.5: Fitting effective bias $b_{\rm eff} \approx b(z_{\rm eff} = 0.68)$ from the observed C_ℓ^{gg}, $C_\ell^{\kappa g}$ up to different $\ell_{\rm max}$ using the HaloFit model for the nonlinear dark matter power spectrum, clustering $b(z)\phi(z)$ (normalized), and no assumptions regarding the shape of the bias evolution.

Perturbation Theory Modelling

We next apply an analytic model. Higher order perturbation theory is a natural approach considering that the cross-correlation is most sensitive to structure at large scales (see Figure 4.10). We use a Lagrangian bias model and the convolution Lagrangian effective field theory (hereafter CLEFT) outlined in Vlah et al. 2016 and the references contained therein. Under this formalism, the matter-galaxy and galaxy-galaxy power spectra are (see e.g. Equa-

tion 2.7 from Modi et al. 2017 and Equation B.2 from Vlah et al. 2016):

$$P_{\rm mg} = (1 - \frac{\alpha_\times k^2}{2})P_{\rm Z} + P_{\rm 1L} + \frac{b_1}{2}P_{\rm b_1} + \frac{b_2}{2}P_{\rm b_2} \tag{4.47}$$

$$P_{\rm gg} = (1 - \frac{\alpha_a k^2}{2})P_{\rm Z} + P_{\rm 1L} + b_1 P_{\rm b_1} + b_2 P_{\rm b_2} + b_1 b_2 P_{\rm b_1 b_2} + b_1^2 P_{\rm b_1^2} + b_2^2 P_{\rm b_2^2} \tag{4.48}$$

where we have dropped the terms corresponding to shear bias as we find they mainly affect scales $\ell > 1000$. Here, $P_{\rm Z}$ and $P_{\rm 1L}$ are the Zeldovich and 1-loop dark matter contributions (see e.g. Vlah et al. 2015), b_1 and b_2 are the Lagrangian bias parameters for the galaxy sample, and the effective field theory terms $\alpha_\times$ and α_a (which are not necessarily the same) are free parameters encapsulating the small-scale physics not modeled by Lagrangian perturbation theory.

Under the CLEFT formalism, the power spectrum contributions $P_{\rm Z}$, $P_{\rm 1L}$, $P_{\rm b_1}$, $P_{\rm b_2}$, etc. can be computed analytically and combined with the free parameters $\alpha_\times, \alpha_a, b_1, b_2$. With these additional degrees of freedom, CLEFT provides a more flexible model than the phenomenological approach of Section 4.6, and allows us to fit the cross-spectrum and galaxy auto-spectrum simultaneously.

We use a version of the public code `velocileptors`[11] (Chen et al. 2020) to calculate the power spectrum terms and the MCMC likelihood estimator `emcee`[12] (Foreman-Mackey et al. 2013) to optimize our model parameters. To reduce model expense, we evaluate the power spectrum terms at a single effective redshift,

$$z_{\rm eff}^{XY} = \frac{\int d\chi \; z \; W^X(\chi) W^Y(\chi)/\chi^2}{\int d\chi \; W^X(\chi) W^Y(\chi)/\chi^2} \tag{4.49}$$

which is $z_{\rm eff} = 0.67$ for κg and $z_{\rm eff} = 0.68$ for gg[13]. Given the narrow redshift distribution and presumed passive bias evolution of our galaxy sample, this substitution should not affect the C_ℓ's significantly (Modi et al., 2017), and we confirm that the overall impact on the scales of interest is sub-percent level. Additionally, this allows us to more easily interpret the Lagrangian bias parameters as being also evaluated at the effective redshift. We use the photometric redshift distribution to eliminate the need to assume a shape for the bias evolution.

We perform a joint fit on both the galaxy-galaxy auto-spectrum and galaxy-convergence cross-spectrum using a simple Gaussian likelihood function:

$$\mathcal{L}(d|\vartheta) \propto \exp\Big\{ -\frac{1}{2}(\hat{C}(\vartheta) - C)\; \Sigma^{-1}\; (\hat{C}(\vartheta) - C)^{\rm T} \Big\} \tag{4.50}$$

[11] https://github.com/sfschen/velocileptors

[12] https://github.com/dfm/emcee

[13] To jointly fit the auto- and cross-spectrum, we assume $z_{\rm eff} = 0.68$ for both.

The vectors C and $\hat{C}(\vartheta)$ are, respectively, the observed and predicted angular power spectra, with the auto- and cross-spectrum measurements joined together as

$$C_L = (C_L^{\kappa g}, C_L^{gg}) \tag{4.51}$$

for each bandwidth bin L. The covariance matrix is also created by stitching together four constituent covariance matrices,

$$\Sigma_{LL'} = \begin{pmatrix} \Sigma_{LL'}^{\kappa g} & (\Sigma_{LL'}^{\kappa g-gg})^{\mathrm{T}} \\ \Sigma_{LL'}^{\kappa g-gg} & \Sigma_{LL'}^{gg} \end{pmatrix} \tag{4.52}$$

The covariance matrices $\Sigma_{LL'}^{\kappa g}$ and $\Sigma_{LL'}^{gg}$ are given by Equations 4.33. Similarly, the Gaussian part of the covariance between the auto-spectrum and cross-spectrum measurements is given by

$$\Sigma_{LL'}^{\kappa g-gg} = (\sigma_L^{\kappa g-gg})^2 \delta_{LL'} \tag{4.53}$$

where

$$\frac{1}{(\sigma_L^{\kappa g-gg})^2} = \frac{1}{\Delta\ell} \sum_{\ell \in L} \frac{1}{(\sigma_\ell^{\kappa g-gg})^2} \tag{4.54}$$

$$(\sigma_\ell^{\kappa g-gg})^2 = \frac{[2C_\ell^{\kappa g}(C_\ell^{gg} + N_\ell^{gg})]_{\mathrm{th}}}{f_{\mathrm{sky}}(2\ell+1)} \frac{w_4}{w_2^2} \tag{4.55}$$

We use flat priors for the four model parameters, and additional impose a loose Gaussian prior on b_2 centered on the peak-background split prediction for a given b_1. The results of the MCMC analysis are listed in Table 4.6, calculated using $\ell_{\mathrm{max}} = 1000$. As in the case of the HaloFit model, we repeat our analysis for $\ell_{\mathrm{max}} = 200, 400, 600, 800$ and find that the best fit parameters remain stable within error bars. The corner plots visualizing the 1D and 2D posterior distributions are shown in Figure 4.13, and the resulting theory predictions are plotted against the binned data in Figure 4.14, both for the $\ell_{\mathrm{max}} = 1000$ case. The values and errors are based on 16th, 50th, and 84th percentiles of the posterior distributions. The model is able to constrain b_1 very well, and provides a more flexible fit to the shape of the data.

We can compare the Lagrangian b_1 to the Eulerian bias found in the previous section,

$$b(z_{\mathrm{eff}}) = 1 + b_1(z_{\mathrm{eff}}) \tag{4.56}$$

$$= b(0)/D(z_{\mathrm{eff}}) \tag{4.57}$$

For $z_{\mathrm{eff}} = 0.68$, the best fit $b_1 = 1.33$ corresponds to $b(0) = 1.64$, in perfect agreement with the result from our HaloFit model using the photometric redshift distribution. Furthermore, after accounting for the uncertainty associated with photometric versus clustering redshift distributions $\sigma_{b_{gg}} = 0.08$, the effective bias from the perturbation theory model is consistent with the effective bias measured using the clustering $b(z)\phi(z)$ (Table 4.5). Thus, these two models show excellent consistency with each other, and both are consistent with the assumed bias evolution model.

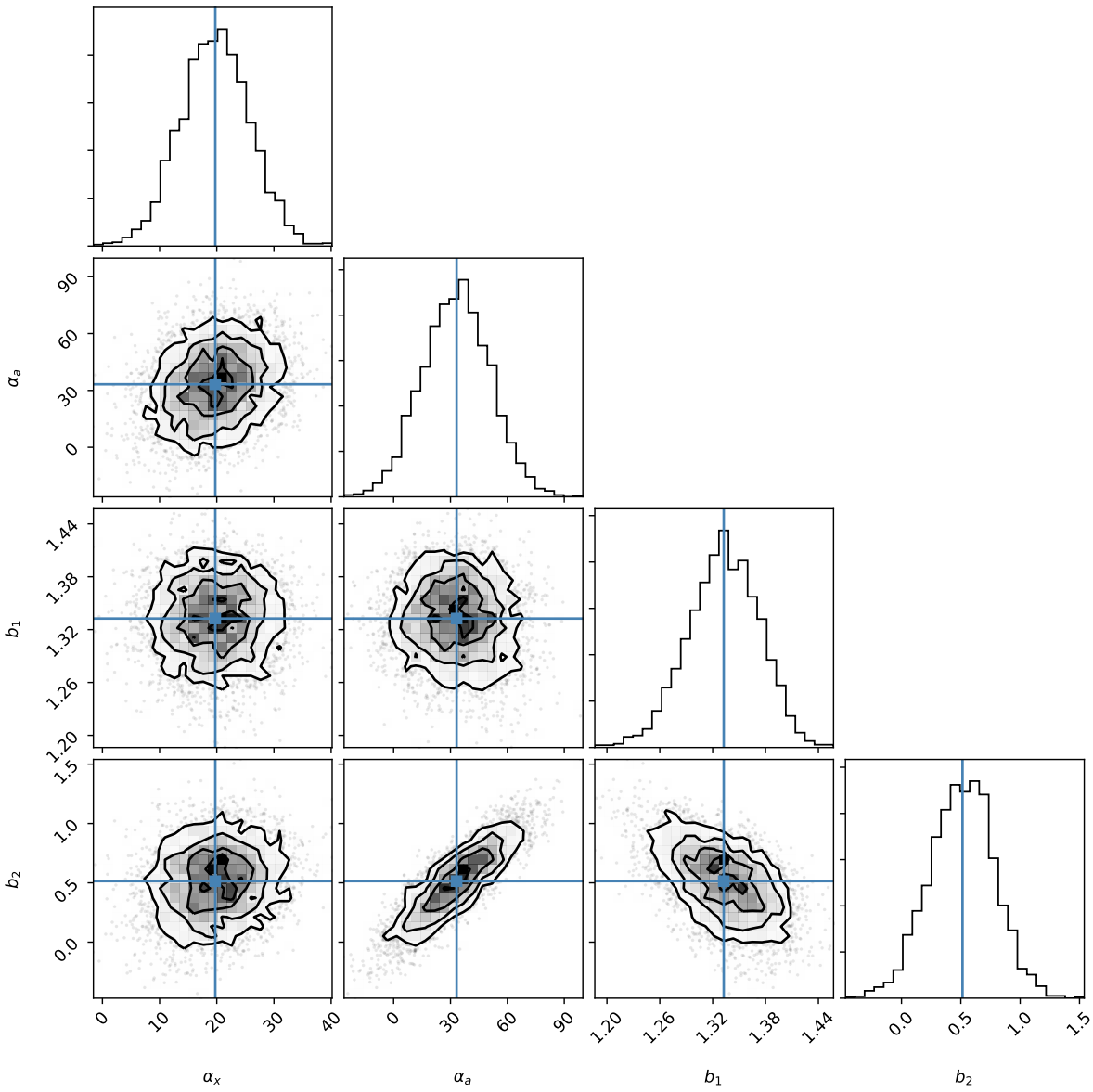

Figure 4.13: Marginalized 1D and 2D posterior probability distributions of the parameters. Vertical lines are median values.

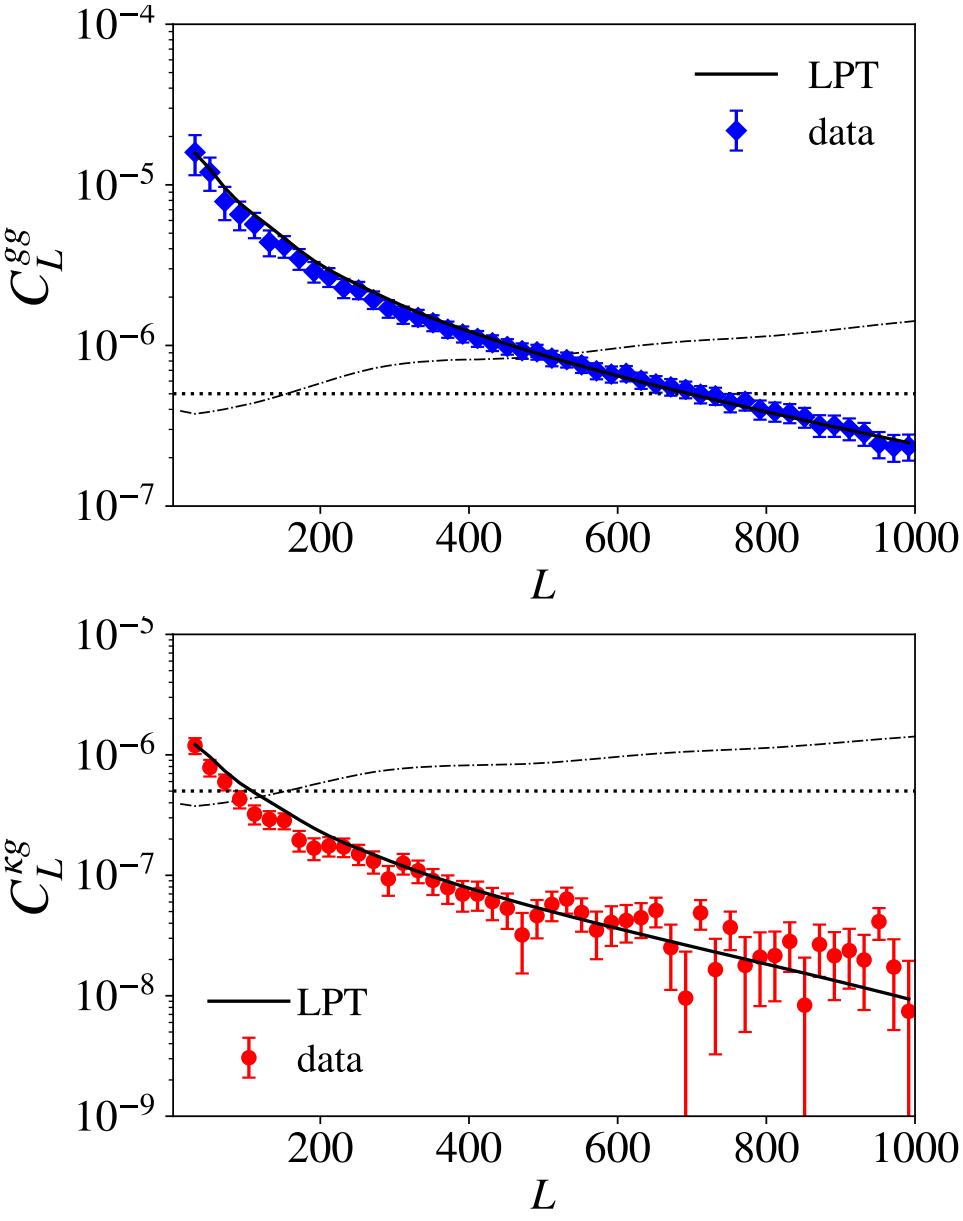

Figure 4.14: The observed galaxy-galaxy (upper plot, blue diamonds) and galaxy-convergence (lower plot, red diamonds) angular power spectra, after subtracting noise and correcting for magnification bias. Solid lines correspond to the predictions from the CLEFT perturbation theory framework using MCMC fitted parameters (Table 4.6). The dotted horizontal line is the galaxy shot noise floor, and the dashed black curve is the lensing noise.

CLEFT Model, Photo $\phi(z)$, $\ell_{\rm max} = 1000$		
Parameter	Prior	Posterior
b_1	$\in [0.5, 1.5]$	$1.33^{+0.04}_{-0.04}$
b_2	$\in [-1, 2]$	$0.514^{+0.255}_{-0.283}$
	$\propto \mathcal{N}\left(\tilde{b}_2, 0.3\right)$	
$\alpha_\times$	$\in [-100, 100]$	$19.74^{+5.94}_{-6.13}$
α_a	$\in [-100, 100]$	$33.23^{+17.54}_{-18.25}$

Table 4.6: The second column lists the priors used for the LPT model parameters, while the third column is the medians and 1σ confidence intervals based on the 16th and 84th percentiles of the posterior distributions. All priors are flat except for the prior on b_2, which is a Gaussian loosely centered at the peak-background split prediction for a given b_1.

4.7 Conclusions for Chapter 4 and Future Directions

In this chapter, we present a cross-correlation between DESI-like LRGs selected from DECaLS DR8 and all-sky CMB lensing maps from Planck, and report a detection significance of $S/N = 27.2$ over a wide range of scales from $\ell_{\rm min} = 30$ to $\ell_{\rm max} = 1000$.

To correct for the effects of magnification bias on the galaxy-galaxy auto-spectrum and galaxy-convergence cross-spectrum, we calculate the slope of the LRG cumulative magnitude function at the limiting magnitude of the survey, determining a value of order unity, $s = 0.999 \pm 0.015$. We find that the resulting corrections to the spectra are on the order of 4-6%. We also test the impact of tSZ bias in the lensing map, showing the associated errors on the galaxy-lensing cross-correlation to be highly sub-dominant to the overall lensing noise.

Within two different frameworks for modeling galaxy clustering and using two different methods for estimating the redshift distribution of the LRG sample, we fit the galaxy bias in multiple complementary ways and cross-check the results, both for internal consistency and to ascertain the impact of uncertainty in the redshift distribution on the inferred bias parameters.

1. Under a simple linear bias times HaloFit model, using a photometric $\phi(z)$ and an assumed bias evolution $b(z) \propto D(z)^{-1}$, we determine best fit values for the present day bias $b_{\rm gg} = 1.64 \pm 0.02$ and $b_{\kappa \rm g} = 1.32 \pm 0.05$. This value of the galaxy bias is similar to the prediction in the DESI Final Design Report (DESI Collaboration et al., 2016), $b_{\rm LRG}(z) = 1.7/D(z)$.

2. Under a simple linear bias times HaloFit model, using a clustering $\phi(z)$ and an assumed bias evolution $b(z) \propto D(z)^{-1}$, we determine best fit values for the present day bias $b_{\rm gg} = 1.56 \pm 0.01$ and $b_{\kappa \rm g} = 1.32 \pm 0.05$. We note that the value of $b_{\rm gg}$ changes by $\sigma_{b_{\rm gg}} = 0.08$ in switching from the photometric estimate of $\phi(z)$ to the clustering

estimate of $\phi(z)$, whereas the cross-correlation is far more robust to this uncertainty in the redshift distribution, with the inferred parameter $b_{\kappa g}$ unchanged.

3. Under a simple linear bias times HaloFit model, using a clustering $b(z)\phi(z)$ with bias evolution implicitly folded into the overall redshift kernel, we determine best fit values for the effective bias $b_{\rm eff} \approx b(z_{\rm eff} = 0.68)$, finding $b_{\rm gg}^{\rm eff} = 2.23 \pm 0.02$ and $b_{\kappa g}^{\rm eff} = 1.88 \pm 0.07$. We find perfect consistency with the results of (ii) under the latter's assumed bias evolution.

4. Under a Lagrangian effective field theory with a Lagrangian bias model, and using a photometric $\phi(z)$, we determine model parameters evaluated at the effective redshift $z_{\rm eff} = 0.68$. The Lagrangian bias parameter $b_1 = 1.33 \pm 0.04$, when converted into Eulerian bias $b = 1 + b_1$, agrees with the results of (iii) within the error found to be associated with uncertainty in the redshift distribution. Furthermore, after applying the bias evolution assumption $b(z) \propto D(z)^{-1}$, this result is also in perfect agreement with the results of (i).

In summary, we find strong constraints on the present day and effective linear bias, with the largest errors on these inferred parameters originating from errors in the galaxy redshift distribution but having negligible effect on the cross bias term $b_{\kappa g}$. We also present a united framework for modeling bias in a bias evolution agnostic way, and use this to validate the assumption of passive bias evolution for LRGs. In future works, we intend to use the same framework to perform joint constraints on cosmological and galaxy bias parameters.

Chapter 5

Summary & Conclusions

This thesis describes original contributions to the field of physical cosmology, specifically the task of mapping the Universe for next-generation dark energy experiments such as the Dark Energy Spectroscopic Instrument (DESI). Chapter 2 provides a review of the theoretical background needed to motivate and contextualize this work, with particular focus on dark energy and two of its most powerful probes, baryon acoustic oscillations and redshift-space distortions (the key deliverables of DESI). In order to fully leverage the statistical power of DESI and other next-generation galaxy surveys, it is crucial to account for and control any non-cosmological signals in the data that could bias scientific studies, and to have a sophisticated understanding of the connection between galaxy clustering and the underlying distribution of dark matter. Chapter 3 presents the first major analysis of the systematics and clustering of the DESI main targets selected from deep imaging, laying the groundwork for all subsequent cosmology with DESI. We present masks and weights that will be used in the construction of cosmological catalogs, and also characterize the large-scale clustering properties of the DESI samples, a vital first step for enabling cosmological analyses and simulations. Furthermore, this chapter presents widely applicable new techniques and frameworks for diagnosing systematic errors as well as performing clustering studies with photometric data. Chapter 4 describes a measurement of the cross-correlation between a sample of DESI-like luminous red galaxies and the matter lensing convergence of the cosmic microwave background, one of the strongest such detections to date. We present two complementary ways to estimate the effective galaxy bias without assuming a form of the bias evolution, and obtain tight constraints on both present day and effective bias. We further quantify the error caused by uncertainty in the redshift distribution of the galaxies. Overall, our findings suggest that DESI is on the path to highly impactful new scientific discoveries. The next generation of dark energy surveys will shed light on the mysteries of our Universe, making this a truly exciting decade to look forward to.

Bibliography

Alam S., et al., 2017, MNRAS, 470, 2617

Albrecht A., et al., 2006, ArXiv Astrophysics e-prints,

Allen S. W., Schmidt R. W., Fabian A. C., 2002, MNRAS, 334, L11

Alonso D., Sanchez J., Slosar A., LSST Dark Energy Science Collaboration 2019, MNRAS, 484, 4127

Amendola L., et al., 2013, Living Reviews in Relativity, 16, 6

Amendola L., Bettoni D., Marta Pinho A., Casas S., 2019, arXiv e-prints, p. arXiv:1902.06978

Anderson L., et al., 2012, MNRAS, 427, 3435

Anderson L., et al., 2014, MNRAS, 441, 24

Ata M., et al., 2018, MNRAS, 473, 4773

Bartelmann M., Schneider P., 2001, Phys. Rep., 340, 291

Bassett B., Hlozek R., 2010, Baryon acoustic oscillations. p. 246

Bautista J. E., et al., 2017, A&A, 603, A12

Bautista J. E., et al., 2018, ApJ, 863, 110

Beutler F., et al., 2011, MNRAS, 416, 3017

Beutler F., et al., 2012, MNRAS, 423, 3430

Blake C., Glazebrook K., 2003, ApJ, 594, 665

Blake C., Wall J., 2002, MNRAS, 337, 993

Blake C., et al., 2011, MNRAS, 415, 2876

Blas D., Lesgourgues J., Tram T., 2011, J. Cosmology Astropart. Phys., 2011, 034

Block D. L., 2012, Georges Lemaître and Stigler's Law of Eponymy. p. 89, doi:10.1007/978-3-642-32254-9_8

Bond J. R., Jaffe A. H., Knox L., 1998, Phys. Rev. D, 57, 2117

Buchalter A., Helfand D. J., Becker R. H., White R. L., 1998, ApJ, 494, 503

Burden A., Padmanabhan N., Cahn R. N., White M. J., Samushia L., 2017, J. Cosmology Astropart. Phys., 3, 001

Busca N. G., et al., 2013, A&A, 552, A96

Cahn R. N., Pinol L., Hand N., McDonald P., Seljak U., 2017, in APS April Meeting Abstracts. p. S5.004

Casas S., Kunz M., Martinelli M., Pettorino V., 2017, preprint, (arXiv:1703.01271)

Chen S.-F., Vlah Z., White M., 2020, arXiv e-prints, p. arXiv:2005.00523

Chevallier M., Polarski D., 2001, International Journal of Modern Physics D, 10, 213

Chiang Y.-K., Ménard B., Schiminovich D., 2018, arXiv e-prints, p. arXiv:1810.00885

Cole S., et al., 2005, MNRAS, 362, 505

Colombi S., Szapudi I., 2001, in Banday A. J., Zaroubi S., Bartelmann M., eds, Mining the Sky. p. 262, doi:10.1007/10849171_29

Comparat J., et al., 2013, MNRAS, 433, 1146

Cresswell J. G., Percival W. J., 2009, MNRAS, 392, 682

Crocce M., Gaztañaga E., Cabré A., Carnero A., Sánchez E., 2011, MNRAS, 417, 2577

Crocce M., et al., 2016, MNRAS, 455, 4301

Croom S. M., et al., 2005, MNRAS, 356, 415

Cutri R. M., et al., 2015, Technical report, Explanatory Supplement to the NEOWISE Data Release Products

DES Collaboration et al., 2005 (arXiv:astro-ph/0510346)

DESI Collaboration et al., 2016 (arXiv:1611.00036)

Davis M., Peebles P. J. E., 1983, ApJ, 267, 465

Davis C., et al., 2018, MNRAS, 477, 2196

Dawson K. S., et al., 2013a, AJ, 145, 10

Dawson K. S., et al., 2013b, AJ, 145, 10

Dawson K. S., et al., 2016, AJ, 151, 44

Delubac T., et al., 2015, A&A, 574, A59

Delubac T., et al., 2017, MNRAS, 465, 1831

Desjacques V., Jeong D., Schmidt F., 2018, Phys. Rep., 733, 1

Dey A., et al., 2018, preprint, (arXiv:1804.08657)

Efron B., 1979, Bootstrap Methods: Another Look at the Jackknife

Efstathiou G., 2004a, MNRAS, 348, 885

Efstathiou G., 2004b, MNRAS, 349, 603

Eisenstein D., 2003, arXiv e-prints, pp astro–ph/0301623

Eisenstein D. J., 2005, New Astron. Rev., 49, 360

Eisenstein D. J., Hu W., Tegmark M., 1998, ApJ, 504, L57

Eisenstein D. J., Seo H.-J., Sirko E., Spergel D. N., 2007, ApJ, 664, 675

Eisenstein D. J., et al., 2011, AJ, 142, 72

Elvin-Poole J., et al., 2018, Phys. Rev. D, 98, 042006

Eriksen H. K., et al., 2004, ApJS, 155, 227

Favole G., et al., 2016, MNRAS, 461, 3421

Fisher K. B., Davis M., Strauss M. A., Yahil A., Huchra J., 1994, MNRAS, 266, 50

Fitzpatrick E. L., 1999, PASP, 111, 63

Flaugher B., et al., 2015, AJ, 150, 150

Font-Ribera A., McDonald P., Mostek N., Reid B. A., Seo H.-J., Slosar A., 2014a, J. Cosmology Astropart. Phys., 5, 023

Font-Ribera A., McDonald P., Mostek N., Reid B. A., Seo H.-J., Slosar A., 2014b, J. Cosmology Astropart. Phys., 2014, 023

Foreman-Mackey D., Hogg D. W., Lang D., Goodman J., 2013, PASP, 125, 306

Friedmann A., 1922, Zeitschrift fur Physik, 10, 377

Fry J. N., 1985, ApJ, 289, 10

Fry J. N., Gaztanaga E., 1993, ApJ, 413, 447

Fry J. N., Colombi S., Fosalba P., Balaraman A., Szapudi I., Teyssier R., 2011, MNRAS, 415, 153

García-García C., Alonso D., Bellini E., 2019, J. Cosmology Astropart. Phys., 2019, 043

Gariazzo S., Lopez-Honorez L., Mena O., 2015, Phys. Rev. D, 92, 063510

Gatti M., et al., 2018, MNRAS, 477, 1664

Górski K. M., Hivon E., Banday A. J., Wandelt B. D., Hansen F. K., Reinecke M., Bartelmann M., 2005, ApJ, 622, 759

Guzik J., Bernstein G., Smith R. E., 2007, MNRAS, 375, 1329

Guzzo L., et al., 2008, Nature, 451, 541

Hamann J., Hannestad S., Melchiorri A., Wong Y. Y. Y., 2008, Journal of Cosmology and Astro-Particle Physics, 2008, 017

Hildebrandt H., et al., 2017, MNRAS, 465, 1454

Hivon E., Górski K. M., Netterfield C. B., Crill B. P., Prunet S., Hansen F., 2002, ApJ, 567, 2

Ho S., Hirata C., Padmanabhan N., Seljak U., Bahcall N., 2008, Phys. Rev. D, 78, 043519

Høg E., et al., 2000, 355, L27

Hogg D. W., et al., 1998, AJ, 115, 1418

Hu W., Okamoto T., 2002, ApJ, 574, 566

Hubble E., 1929, Proceedings of the National Academy of Science, 15, 168

Hubble E., 1934, ApJ, 79, 8

Huterer D., et al., 2015, Astroparticle Physics, 63, 23

Jackson J. C., 1972, MNRAS, 156, 1P

Jain B., Khoury J., 2010, Annals of Physics, 325, 1479

Jarrett T. H., Chester T., Cutri R., Schneider S., Skrutskie M., Huchra J. P., 2000, AJ, 119, 2498

Jimenez R., Loeb A., 2002, ApJ, 573, 37

Jouvel S., et al., 2015, arXiv e-prints, p. arXiv:1509.07121

Joyce A., Jain B., Khoury J., Trodden M., 2015, Phys. Rep., 568, 1

Kaiser N., 1987, MNRAS, 227, 1

Kashiwagi T., Yahata K., Suto Y., 2013, PASJ, 65, 43

Kashiwagi T., Suto Y., Taruya A., Kayo I., Nishimichi T., Yahata K., 2015, ApJ, 799, 132

Kazin E. A., et al., 2013, MNRAS, 435, 64

Kellermann K. I., 1993, Nature, 361, 134

Kirkby D., et al., 2013, J. Cosmology Astropart. Phys., 2013, 024

Kitanidis E., et al., 2019, arXiv e-prints, p. arXiv:1911.05714

Krolewski A., Ferraro S., Schlafly E. F., White M., 2019, arXiv e-prints, p. arXiv:1909.07412

LSST Science Collaboration et al., 2009, arXiv e-prints, p. arXiv:0912.0201

Landy S. D., Szalay A. S., 1993, ApJ, 412, 64

Landy S. D., Szalay A. S., Koo D. C., 1996, ApJ, 460, 94

Lang D., Hogg D. W., Mykytyn D., 2016, The Tractor: Probabilistic astronomical source detection and measurement, Astrophysics Source Code Library (ascl:1604.008)

Laurent P., et al., 2017, J. Cosmology Astropart. Phys., 2017, 017

Leistedt B., et al., 2016, ApJS, 226, 24

Lemaître G., 1927, Annales de la Société Scientifique de Bruxelles, 47, 49

Lewis A., Challinor A., 2006, Phys. Rep., 429, 1

Limber D. N., 1953, ApJ, 117, 134

Linder E. V., 2003, Phys. Rev. Lett., 90, 091301

LoVerde M., Hui L., Gaztañaga E., 2008, Phys. Rev. D, 77, 023512

Loverde M., Afshordi N., 2008, Phys. Rev. D, 78, 123506

Madhavacheril M. S., Hill J. C., 2018, arXiv e-prints, p. arXiv:1802.08230

Marulli F., et al., 2013, A&A, 557, A17

Matthews D. J., Newman J. A., 2010, ApJ, 721, 456

Matthews D. J., Newman J. A., 2012, ApJ, 745, 180

McQuinn M., White M., 2013, MNRAS, 433, 2857

Ménard B., Scranton R., Schmidt S., Morrison C., Jeong D., Budavari T., Rahman M., 2013, arXiv e-prints, p. arXiv:1303.4722

Mo H. J., Jing Y. P., Boerner G., 1992, ApJ, 392, 452

Modi C., White M., Vlah Z., 2017, Journal of Cosmology and Astro-Particle Physics, 2017, 009

Moresco M., et al., 2016, J. Cosmology Astropart. Phys., 2016, 014

Mostek N., Coil A. L., Cooper M., Davis M., Newman J. A., Weiner B. J., 2013, ApJ, 767, 89

Myers A. D., et al., 2006, ApJ, 638, 622

Myers A. D., White M., Ball N. M., 2009, MNRAS, 399, 2279

Newman J. A., 2008, ApJ, 684, 88

Norberg P., Baugh C. M., Gaztañaga E., Croton D. J., 2009, MNRAS, 396, 19

Okumura T., et al., 2016, PASJ, 68, 38

Omori Y., et al., 2019, Phys. Rev. D, 100, 043501

Osborne S. J., Hanson D., Doré O., 2014, J. Cosmology Astropart. Phys., 2014, 024

Padmanabhan N., White M., Norberg P., Porciani C., 2009, MNRAS, 397, 1862

Padmanabhan N., Xu X., Eisenstein D. J., Scalzo R., Cuesta A. J., Mehta K. T., Kazin E., 2012, MNRAS, 427, 2132

Peacock J. A., 1999, Cosmological Physics

Peacock J. A., et al., 2001, Nature, 410, 169

Peebles P. J. E., 1980, The large-scale structure of the universe

Percival W. J., et al., 2004, MNRAS, 353, 1201

Perlmutter S., et al., 1998, Nature, 391, 51

Phillipps S., Shanks T., 1987, MNRAS, 227, 115

Pinol L., Cahn R. N., Hand N., Seljak U., White M., 2017, J. Cosmology Astropart. Phys., 4, 008

Planck Collaboration et al., 2018a, arXiv e-prints, p. arXiv:1807.06209

Planck Collaboration et al., 2018b, arXiv e-prints, p. arXiv:1807.06210

Prakash A., et al., 2016, ApJS, 224, 34

Rahman M., Ménard B., Scranton R., Schmidt S. J., Morrison C. B., 2015, MNRAS, 447, 3500

Riess A. G., et al., 1998, AJ, 116, 1009

Rodríguez-Torres S. A., et al., 2016, MNRAS, 460, 1173

Ross A. J., Brunner R. J., Myers A. D., 2006, ApJ, 649, 48

Ross A. J., et al., 2011, MNRAS, 417, 1350

Ross A. J., et al., 2012, MNRAS, 424, 564

Rubin V. C., 1954, 40, 54

Ruggeri R., et al., 2019, MNRAS, 483, 3878

Samushia L., Percival W. J., Raccanelli A., 2012, MNRAS, 420, 2102

Samushia L., et al., 2014, MNRAS, 439, 3504

Sawangwit U., Shanks T., Abdalla F. B., Cannon R. D., Croom S. M., Edge A. C., Ross N. P., Wake D. A., 2011, MNRAS, 416, 3033

Schaan E., Ferraro S., 2019, Phys. Rev. Lett., 122, 181301

Schlafly E. F., Finkbeiner D. P., 2011, ApJ, 737, 103

Schlegel D. J., Finkbeiner D. P., Davis M., 1998, ApJ, 500, 525

Schmidt S. J., Ménard B., Scranton R., Morrison C., McBride C. K., 2013, MNRAS, 431, 3307

Schulz A. E., 2010, ApJ, 724, 1305

Schulz A. E., White M., 2006, Astroparticle Physics, 25, 172

Scodeggio M., et al., 2018, A&A, 609, A84

Scottez V., et al., 2016, MNRAS, 462, 1683

Scottez V., Benoit-Lévy A., Coupon J., Ilbert O., Mellier Y., 2018, MNRAS, 474, 3921

Scranton R., et al., 2002, ApJ, 579, 48

Seldner M., Peebles P. J. E., 1979, ApJ, 227, 30

Seljak U., 2001, MNRAS, 325, 1359

Simon P., 2007, A&A, 473, 711

Slosar A., et al., 2013, J. Cosmology Astropart. Phys., 2013, 026

Smith R. E., et al., 2003, MNRAS, 341, 1311

Smith R. E., Scoccimarro R., Sheth R. K., 2007, Phys. Rev. D, 75, 063512

Suchyta E., et al., 2016, MNRAS, 457, 786

Szapudi I., 1998, ApJ, 497, 16

Szapudi I., Colombi S., 1996, ApJ, 470, 131

Szapudi I., Szalay A. S., 1993a, ApJ, 408, 43

Szapudi I., Szalay A. S., 1993b, ApJ, 408, 43

Szapudi I., Meiksin A., Nichol R. C., 1996, ApJ, 473, 15

Taylor J. F., Ashdown M. A. J., Hobson M. P., 2008, MNRAS, 389, 1284

Tegmark M., 1997, Phys. Rev. D, 55, 5895

Tegmark M., de Oliveira-Costa A., 2001, Phys. Rev. D, 64, 063001

Tellarini M., Ross A. J., Tasinato G., Wands D., 2016, J. Cosmology Astropart. Phys., 6, 014

Tojeiro R., et al., 2014, MNRAS, 440, 2222

Vlah Z., White M., Aviles A., 2015, A Lagrangian effective field theory (`arXiv:1506.05264`), doi:10.1088/1475-7516/2015/09/014

Vlah Z., Castorina E., White M., 2016, J. Cosmology Astropart. Phys., 2016, 007

Wandelt B. D., Hansen F. K., 2003, Phys. Rev. D, 67, 023001

Wechsler R. H., Tinker J. L., 2018, ARA&A, 56, 435

Weinberg D. H., Mortonson M. J., Eisenstein D. J., Hirata C., Riess A. G., Rozo E., 2013, Phys. Rep., 530, 87

White S. D. M., 1979, MNRAS, 186, 145

Wilson M. J., White M., 2019, arXiv e-prints, p. arXiv:1904.13378

Wolk M., McCracken H. J., Colombi S., Fry J. N., Kilbinger M., Hudelot P., Mellier Y., Ilbert O., 2013, MNRAS, 435, 2

Wright E. L., et al., 2010, AJ, 140, 1868

Yahata K., Yonehara A., Suto Y., Turner E. L., Broadhurst T., Finkbeiner D. P., 2007, PASJ, 59, 205

Zaldarriaga M., Seljak U., 1999, Phys. Rev. D, 59, 123507

Zehavi I., et al., 2005, ApJ, 621, 22

Zhou R., et al., 2020, arXiv e-prints, p. arXiv:2001.06018

Zhu F., et al., 2018, MNRAS, 480, 1096

Ziour R., Hui L., 2008, Phys. Rev. D, 78, 123517

de la Torre S., et al., 2013, A&A, 557, A54

du Mas des Bourboux H., et al., 2017, A&A, 608, A130

van Engelen A., Bhattacharya S., Sehgal N., Holder G. P., Zahn O., Nagai D., 2014, ApJ, 786, 13

Appendix A

Clustering Redshift Formalism

A.1 Detailed Derivation

The angular cross-correlation function is related to the spatial cross-correlation function by the equation

$$w_{\rm ps}(\theta, z_{\rm i}) = \int_0^\infty d\chi_1 \int_0^\infty d\chi_2 \; \phi_{\rm p}(\chi_1)\phi_{\rm s}(\chi_2) \times \; \xi_{\rm ps}\left(\sqrt{\chi_1^2 + \chi_2^2 - 2\chi_1\chi_2\cos\theta}, z_{\rm i}\right) \tag{A.1}$$

where the $\phi(\chi)$'s are the normalized radial distributions, and are related to the normalized redshift distributions $\phi(z)$ by $\phi(\chi) = \phi(z)H(z)/c$. Applying algebraic massaging to the argument of $\xi_{\rm ps}$, we have

$$\sqrt{\chi_1^2 + \chi_2^2 - 2\chi_1\chi_2\cos\theta} = \sqrt{2(\frac{\chi_1+\chi_2}{2})^2(1-\cos\theta) + \frac{(\chi_2-\chi_1)^2}{2}(1+\cos\theta)} \tag{A.2}$$

Since we are restricting to $\theta \leq 1^\circ$, we can use the small-angle approximation[1], $\cos\theta \approx 1 - \theta^2/2$, to simplify this expression.

$$w_{\rm ps}(\theta, z_{\rm i}) = \int_0^\infty d\chi_1 \int_0^\infty d\chi_2 \; \phi_{\rm p}(\chi_1)\phi_{\rm s}(\chi_2) \times \; \xi_{\rm ps}\left(\sqrt{(\frac{\chi_1+\chi_2}{2})^2\theta^2 + (\chi_2-\chi_1)^2}, z_{\rm i}\right) \tag{A.3}$$

Furthermore, if the redshift bins are sufficiently narrow, we can treat the spectroscopic redshift distribution as a Dirac delta function $\phi_{\rm s}(z) \propto \delta^D(z - z_{\rm i})$ for each bin and perform

[1] At 1°, this approximation is accurate to within $\approx 4 \times 10^{-9}$.

the $d\chi_2$ integral directly. We also note that the $d\chi_1$ integral is, in practice, only evaluated over the range of redshifts for which $\phi_{\rm p}(z)$ is non-zero, $z_{\rm min}$ to $z_{\rm max}$.

$$w_{\rm ps}(\theta, z_{\rm i}) \propto \int_{\chi_{\rm min}}^{\chi_{\rm max}} d\chi\ \phi_{\rm p}(\chi) \times\ \xi_{\rm ps}\left(\sqrt{(\frac{\chi+\chi_{\rm i}}{2})^2\theta^2 + (\chi-\chi_{\rm i})^2}, z_{\rm i}\right) \tag{A.4}$$

We now rewrite $\xi_{\rm ps}$ in terms of the underlying dark matter correlation function times the linear biases of the photometric and spectroscopic samples,

$$w_{\rm ps}(\theta, z_{\rm i}) \propto \int_{\chi_{\rm min}}^{\chi_{\rm max}} d\chi\ \phi_{\rm p}(\chi) b_{\rm p}(\chi) b_{\rm s}(\chi_{\rm i}) \times\ \xi_{\rm mm}\left(\sqrt{(\frac{\chi+\chi_{\rm i}}{2})^2\theta^2 + (\chi-\chi_{\rm i})^2}, z_{\rm i}\right) \tag{A.5}$$

Next, we apply the Limber approximation (generally valid for scales $\theta \leq 1^\circ$), which assumes that $\phi_{\rm p}$ and $b_{\rm p}$ do not vary appreciably over the characteristic scale defined by $\xi_{\rm mm}$, and thus can be taken out of the integral. Since the integrand is sharply peaked around $\chi = \chi_{\rm i}$, this gives

$$w_{\rm ps}(\theta, z_{\rm i}) \propto \phi_{\rm p}(\chi_{\rm i}) b_{\rm p}(\chi_{\rm i}) b_{\rm s}(\chi_{\rm i}) \times \int_{\chi_{\rm min}}^{\chi_{\rm max}} d\chi\ \xi_{\rm mm}\left(\sqrt{\chi_{\rm i}^2\theta^2 + (\chi-\chi_{\rm i})^2}, z_{\rm i}\right) \tag{A.6}$$

$$= \phi_{\rm p}(z_{\rm i}) \frac{H(z_{\rm i})}{c} b_{\rm p}(z_{\rm i}) b_{\rm s}(z_{\rm i}) I(\theta, z_{\rm i}) \tag{A.7}$$

where

$$I(\theta, z_{\rm i}) \equiv \int_{\chi_{\rm min}}^{\chi_{\rm max}} d\chi\ \xi_{\rm mm}\left(\sqrt{\chi_{\rm i}^2\theta^2 + (\chi-\chi_{\rm i})^2}, z_{\rm i}\right) \tag{A.8}$$

can be computed directly from theory.

A.2 Understanding $I(z)$

To understand the shape of $I(z)$, it is useful to switch the integration variable from $d\chi$ to $dz = H(z)/c d\chi$, such that we have

$$I(\theta, z_{\rm i}) = \int_{z_{\rm min}}^{z_{\rm max}} dz\ \frac{c}{H(z)} \xi_{\rm mm}\left(\sqrt{\chi_{\rm i}^2\theta^2 + (\chi-\chi_{\rm i})^2}, z_{\rm i}\right) \tag{A.9}$$

For linear scales, $\xi_{\rm mm}(r,z) = D(z)^2\xi_{\rm mm}(r,z=0) \implies$

$$I(\theta, z_{\rm i}) = \int_{z_{\rm min}}^{z_{\rm max}} dz\ \frac{cD(z)^2}{H(z)}\xi_{\rm mm}\left(\sqrt{\chi_{\rm i}^2\theta^2 + (\chi-\chi_{\rm i})^2}, 0\right) \tag{A.10}$$

Since the integrand is sharply peaked around $\chi(z) = \chi_{\rm i}$,

$$I(\theta, z_{\rm i}) \approx \frac{cD(z_{\rm i})^2}{H(z_{\rm i})}\int_{z_{\rm min}}^{z_{\rm max}} dz\ \xi_{\rm mm}\left(\sqrt{\chi_{\rm i}^2\theta^2 + (\chi-\chi_{\rm i})^2}, 0\right) \tag{A.11}$$

This form tells us that $I(\theta, z_{\rm i}) \propto D(z_{\rm i})^2/H(z_{\rm i})$ multiplied by an integral that is only weakly dependent on $z_{\rm i}$ through the co-moving distance $\chi_{\rm i} = \chi(z_{\rm i})$. Furthermore, we note that if both biases are passively evolving $b(z) \propto D(z)^{-1}$, then Equation A.7 reduces to a direct proportionality $w_{\rm ps}(\theta, z_{\rm i}) \propto \phi(z_{\rm i})$ for linear scales.

A.3 Normalization and Scale-Dependent Bias

One of the principal challenges of determining $\phi(z)$ through cross-correlation analysis is the fact that each cross-correlation measurement is only reliable over the subset of the redshift range in which the two samples overlap. Hence, while it's often touted that only the redshift dependence of the various functions such as bias are required to constrain $\phi(z)$, as the many proportionality constants can be normalized away, the different measurements must first be connected piece-wise. Even when all nuisance parameters can be tracked and accounted for, the analysis is ultimately limited by the fact that the biases may be somewhat scale-dependent on the scales in which signal-to-noise is high for angular cross-correlations. Hence, the choice of which scales to integrate over, as discussed in Section 4.3, can lead to additional factors. In practice, we often need to integrate over different physical scales for different cross-correlations to optimize S/N (for example, VIPERS has high surface density but very small area, so the information lies mostly in smaller scales compared to CMASS and eBOSS), leading to some residual offsets between the measurements.

As an example to probe how scale dependence can change the clustering-derived $\phi(z)$, we consider the "P-model" (Smith et al. 2007, Hamann et al. 2008, Cresswell & Percival 2009), where the nonlinear correction to the bias is represented as an additional constant in the power spectrum that accounts for non-Poissonian shot noise associated with the 1-halo term (Seljak 2001, Schulz & White 2006, Guzik et al. 2007),

$$P_{\rm g}(k) \to b_{\rm g}^2 P_{\rm mm}(k) + \mathcal{P} \implies \tag{A.12}$$

$$\xi_{\rm ps}(r) \to b_{\rm p}b_{\rm s}\xi_{\rm mm}(r) + \xi_{\mathcal{P}}(r) \tag{A.13}$$

where $\xi_{\mathcal{P}}(r)$ is simply the Hankel transformed $\mathcal{P}$,

$$\xi_{\mathcal{P}}(r) = \int \frac{dk}{k} \frac{k^3}{2\pi^2} \mathcal{P}\ j_0(kr) \tag{A.14}$$

$$= \frac{\mathcal{P}}{2\pi^2} \int dk\ k^2 j_0(kr) \tag{A.15}$$

Hence,

$$w_{\rm ps}(\theta, z_{\rm i}) \propto \phi_{\rm p}(z_{\rm i}) \frac{H(z_{\rm i})}{c} (b_{\rm p}(z_{\rm i}) b_{\rm s}(z_{\rm i}) I(\theta, z_{\rm i}) + J(\theta, z_{\rm i})) \tag{A.16}$$

where

$$J(\theta, z_{\rm i}) \equiv \int_{\chi_{\rm min}}^{\chi_{\rm max}} d\chi\ \xi_{\mathcal{P}} \left(\sqrt{\chi_{\rm i}^2 \theta^2 + (\chi - \chi_{\rm i})^2}, z_{\rm i} \right) \tag{A.17}$$

Without knowing the value of $\mathcal{P}$, the exact normalization (and, indeed, the shape) of $\phi_{\rm p}(z)$ cannot be computed, since

$$\phi_{\rm p}(z_{\rm i}) \propto \frac{w_{\rm ps}(\theta, z_{\rm i}) \frac{c}{H(z_{\rm i})}}{b_{\rm p}(z_{\rm i}) b_{\rm s}(z_{\rm i}) I(\theta, z_{\rm i}) + J(\theta, z_{\rm i})} \tag{A.18}$$

Assuming that the scale-dependent term is sub-dominant, $J/I \ll 1$, we can expand in this ratio,

$$\begin{aligned} \phi_{\rm p}(z_{\rm i}) &\propto \frac{w_{\rm ps}(\theta, z_{\rm i}) \frac{c}{H(z_{\rm i})}}{b_{\rm p}(z_{\rm i}) b_{\rm s}(z_{\rm i}) I(\theta, z_{\rm i})} \frac{1}{1 + \frac{J(\theta, z_{\rm i})}{b_{\rm p}(z_i) b_{\rm s}(z_i) I(\theta, z_{\rm i})}} \\ &\approx \frac{w_{\rm ps}(\theta, z_{\rm i}) \frac{c}{H(z_{\rm i})}}{b_{\rm p}(z_{\rm i}) b_{\rm s}(z_{\rm i}) I(\theta, z_{\rm i})} (1 - \frac{J(\theta, z_{\rm i})}{b_{\rm p}(z_i) b_{\rm s}(z_i) I(\theta, z_{\rm i})} + \mathcal{O}^2) \end{aligned} \tag{A.19}$$

and thus obtain an estimate of the leading order effect of including scale-dependent bias for a given $\mathcal{P}$ and range of redshifts and angles.